Liquid-microjet photoelectron spectroscopy and dynamics of the photoactive yellow protein chromophore in aqueous solution

Edoardo Simonetti

A dissertation submitted in partial fulfillment

of the requirements for the degree of

Doctor of Philosophy

of

University College London.

Department of Chemistry

University College London

November 22, 2025

I, Edoardo Simonetti, confirm that the work presented in this thesis is my own. Where information has been derived from other sources, I confirm that this has been indicated in the work.

Abstract

Understanding the way complex environments influence the electronic structure and excited state dynamics of biological chromophores is crucial for uncovering the fundamental mechanisms driving photochemical processes in biological systems. Liquid-microjet photoelectron spectroscopy (LJ-PES) is an indispensable tool for the study of solutes in aqueous environments, as it enables direct measurement of electron binding energies in solution. However, a major challenge of ultraviolet (UV) LJ-PES, which allows the study of solutes at sub-mM concentrations, lies in our limited understanding of inelastic scattering of low energy electrons (<10 eV) in water, hindering the determination of accurate binding energies. The work presented in Chapter 3 describes a systematic investigation of the parameters employed in the modelling of inelastic scattering in aqueous solution. It examines the effect the scattering cross-sections, electron transmission at the liquid-vacuum interface and the concentration depth profiles of solutes on the retrieval of the genuine photoelectron distributions, using water, phenol and phenolate as benchmarks. Exploiting these results, Chapter 4 describes an investigation of the electronic structure of the photoactive yellow protein (PYP) chromophore using X-ray, extreme UV and UV LJ-PES. The first two vertical detachment energies and the adiabatic detachment energy of the chromophore were determined. Additionally, a high-lying resonance responsible for electron ejection into solution and a resonance embedded in the continuum were identified. Chapter 5 describes an investigation of the photochemical dynamics of the PYP chromophore following excitation to its first excited state using with UV LJ-PES. The mea-

surements and analysis revealed that the chromophore moves away from the Franck-Condon region either through solvent relaxation or via rotation around the single bond adjacent to the double bond involved in isomerisation within the protein. Overall the work described in this thesis enhances our ability to interpret UV photoelectron spectra of aqueous solutions and provides new insights into the electronic structure and photochemical dynamics of the PYP chromophore.

Impact Statement

Photoactive proteins play important roles in biological systems enabling processes such as phototaxis, vision and bioluminescence. Understanding the photochemistry of the chromophores embedded within photoactive proteins is essential for advancing technologies such as bioimaging, biophotovoltaics, optogenetics and molecular switches.

This thesis contributes significantly to this understanding by investigating the electronic structure and excited-state dynamics of the photoactive yellow protein chromophore in aqueous solution using liquid-microjet-photoelectron spectroscopy. The photoactive yellow protein has been employed as a model system of biological photoreceptors, and insights into its photocycle can inform the design of novel bioimaging probes or biomolecular devices.

A major outcome of this thesis is the refinement of methodologies employed in the interpretation of ultraviolet photoelectron spectra of aqueous solutions. By systematically investigating the effects of parameters employed in simulations of electron scattering in water, this work enhances the accuracy of liquid-jet photoelectron spectroscopy measurements at physiologically relevant concentrations. These improvements are broadly applicable to the study of other biological and chemical systems in solution, enabling reliable characterisation of electronic structure and photoinduced chemical reactions in solution.

In addition, this thesis provides new spectroscopic data on the electronic structure of the PYP chromophore, including the identification of states that lead to electron ejection and the relaxation pathways of the chromophore upon

photoexcitation. These results deepen our understanding of how chromophores behave in a complex environment and have the potential to inform the design of photoactive proteins with targeted functional properties.

UCL Research Paper Declaration Form: Referencing the Doctoral Candidate's Own Published Work(s)

1. **For a research manuscript that has already been published** (if not yet published, skip to section 2):

   (a) **Title of the manuscript:** Retrieval of Genuine Ultraviolet Liquid-Microjet Photoelectron Spectra

   (b) **Provide the DOI or direct link to the published work:** DOI: 10.1021/acs.jpca.5c02024

   (c) **Publication name (e.g., journal or textbook):** The Journal of Physical Chemistry A

   (d) **Publisher name (e.g., Elsevier, Oxford University Press):** American Chemical Society

   (e) **Date of publication:** 5 June 2025

   (f) **List all authors as they appear in the publication:** Edoardo Simonetti, Helen H. Fielding

   (g) **Was the work peer-reviewed?** Yes

   (h) **Do you retain copyright for the work?** Yes

   (i) **Was an earlier version uploaded to a preprint server (e.g.,**

medRxiv, arXiv)? If **Yes**, provide the DOI or direct link. If not applicable, leave blank. Yes, DOI: 10.26434/chemrxiv-2025-1hvbm

If **No**, please seek publisher permission and check the box below:

☐ *I acknowledge permission from the publisher named in item 1d to include in this thesis portions of the publication cited in item 1c.*

2. **For a manuscript prepared for publication but not yet published** (if already published, skip to section 3):

   (a) **Current title of the manuscript:**

   (b) **Has it been uploaded to a preprint server (e.g., medRxiv, arXiv)?**

   If **Yes**, provide the DOI or direct link. If not applicable, leave blank.

   (c) **Intended publication outlet (e.g., journal name):**

   (d) **List all authors in the intended authorship order:**

   (e) **Current stage of publication (e.g., in submission, under review):**

3. **For multi-authored work, please provide a contribution statement detailing each author's role** (if single-authored, skip to section 4): E.S adapted and refined the code, performed the analysis, wrote the first draft of the manuscript and plotted the figures. H.H.F supervised the project. H.H.F. and E.S. edited the final draft.

4. **In which chapter(s) of your thesis can this material be found?** Chapter 3

e-Signatures confirming accuracy of the above information

(This form should be co-signed by the supervisor/senior author unless the work is single-authored):

Candidate signature:

Date: 17/10/2025

Supervisor/Senior Author signature (where appropriate):

Date: 17/10/2025

Acknowledgements

First and foremost, I would like to thank my supervisor, Professor Helen Fielding, for her invaluable support, guidance, and patience throughout my time at UCL. Your encouragement, feedback, and thoughtful advice have helped shape both my research and personal development over the past three years. I am especially grateful for your timely and constructive comments on drafts of this thesis, and for the many scientific opportunities you have provided along the way.

I am thankful to Iain Wilkinson for giving me the opportunity to work in his outstanding lab and broaden my knowledge of liquid-jet photoelectron spectroscopy. I am also grateful to Bernd Winter for the opportunity to work in his lab and visit DESY.

I would like to thank Johanna Rademacher for her continuous support. Thank you for providing valuable feedback on chapters of this thesis, helpful discussions, fun coding sessions, and tireless help in the lab. Thank you for being a wonderful friend outside the lab. Thank you, Kate Robertson, for being such an exceptional lab companion, facing the numerous challenges the liquid jet has thrown at us with me. Thank you for your support, everlasting determination, amazing friendship, and great music taste. It has been so fun working with you. I would like to thank Sufiyan Kahn for being a wonderful companion throughout this PhD journey from day one. Thank you for the insightful discussions, extensive support and many enjoyable moments. It has been a pleasure to work alongside you over the past three years. My thanks also go to David Bacon for sharing his expertise in the lab and for his generous

help with experiments. I would like to thank Adela Ceman for being such a fantastic addition to our group and her incredible support during the writing of this thesis. I wish you the very best with your PhD. I am also grateful to Igor Kiyan, Bruno Credidio, Harmanjot Kaur for their invaluable support with experiments in Berlin. I would also like to thank William Fortune, for his help in the lab at the start of my PhD, and Michael Scholz, for developing the spectral retrieval code used in this work.

Thank you to all my friends for their incredible support, kindness and laughter, which have made the past three years so much easier and enjoyable. Finally, I would like to thank my parents, whose love, encouragement and belief in me have made everything possible. Thank you for always supporting me throughout my studies. A heartfelt thank you to my sister Gaia for her selflessness, support and always being there for me.

Contents

Chapter 1

Introduction

1.1 Photoelectron spectroscopy

The photoelectric effect was first observed by Hertz in 1887,[1] and a series of subsequent experiments showed that (i) electrons were only emitted from a metal surface if the frequency of the incident light was greater than a sample specific threshold, (ii) the kinetic energy of the emitted electrons was dependent on the frequency not the intensity of the incident light, and (iii) the light intensity determined how many electrons were emitted.[2] A description of these phenomena was developed by Einstein in 1905,[3] when he proposed that the energy of light is quantised following the relationship $E = h\nu$, where E is the energy of one light quantum (photon), h is the Planck constant and ν is the frequency of light. He also proposed that eKE of the emitted electrons could be described as

$$\text{eKE} = h\nu - W \tag{1.1}$$

where W is the work required to remove an electron from the surface into vacuum. This explained the previously unresolved experimental results: (i) eKE depends on the frequency of light, (ii) electrons are only emitted if the energy of one photon is higher than W, and (iii) the number of emitted electrons is proportional to the number of photons absorbed by the sample.

This fundamental understanding of light-matter interaction formed the

foundation for photoelectron spectroscopy (PES), a powerful technique for probing the electronic structure of atoms, molecules and materials. In PES, photons of a known energy are employed to eject electrons from a sample, and the kinetic energy of these electrons is measured. For an isolated neutral molecule M, this process can be summarised as

$$\mathrm{M} \xrightarrow{h\nu} \mathrm{M}^+ + \mathrm{e}^- \tag{1.2}$$

and for a closed shell anion M^-,

$$\mathrm{M}^- \xrightarrow{h\nu} \mathrm{M}^\cdot + \mathrm{e}^- \tag{1.3}$$

where $h\nu$ is the energy of one photon, M^+ is the corresponding cation of M, $\mathrm{M}^\cdot$ is the corresponding neutral radical of M^-, and e^- is the ejected electron. In the independent electron approximation (Koopmans' theorem),[4,5] ionisation occurs without reorganisation of the remaining electrons, and the energy to remove an electron is equal to the negative of the energy of the molecular orbital from which it is removed. Hence, the eKE can be related to the binding energy of the electron (eBE) through the relationship

$$\mathrm{eKE} = h\nu - \mathrm{eBE}. \tag{1.4}$$

Measurement of the eBEs of different electrons in a material offers a picture of its electronic structure.

As photoionisation is effectively instantaneous with respect to nuclear motion, transitions occur within the Born-Oppenheimer approximation and the transition probability is governed by the Franck-Condon (FC) overlap between the vibronic wavefunctions of M and M^+ (Figure 1.1). The most likely transition yields the vertical ionisation energy (VIE) or vertical detachment energy (VDE) for anionic species. Another important quantity is the adiabatic ionisation energy (AIE) or adiabatic detachment energy (ADE), defined as the

energy difference between the vibrational ground states of M and the vibrational ground state of M^+ (Figure 1.1). In a photoelectron spectrum, the VIE and AIE correspond to the peak maximum and the onset of the peak, respectively.

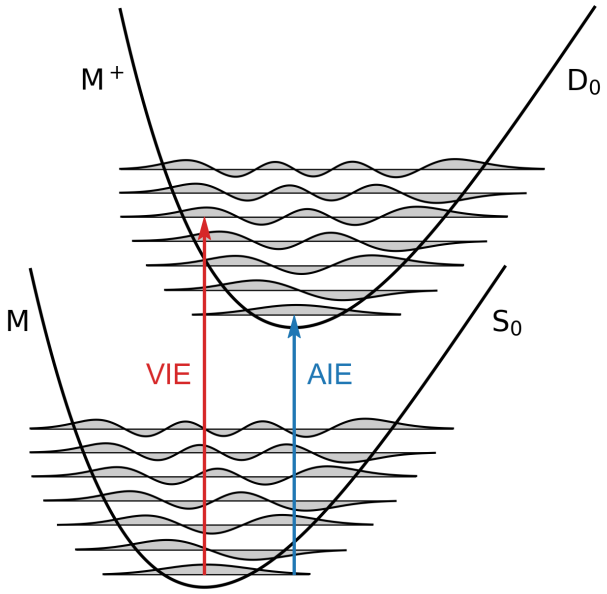

Figure 1.1: Diagram illustrating the vertical ionisation energy (VIE) and adiabatic ionisation energy (AIE). Within the Born-Oppenheimer approximation, photoionisation occurs much faster than nuclear motion, and transitions are governed by the Franck-Condon overlap of the wavefunctions of M and M^+. The most likely transition yields the VIE (red) and the transition from the ground vibrational state of M to the ground vibrational state of M^+ yields the AIE (blue). For closed shell anions, where the photodetachment process is $M^- \xrightarrow{h\nu} M^{\cdot} + e^-$, the equivalent quantities are VDEs and ADEs.

Thanks to advances in monochromatic X-ray and extreme ultraviolet (EUV) sources as well as electron energy analysers, the 1950s and 1960s saw the development of modern photoelectron spectroscopy.[6,7] This work was largely driven by Siegbahn,[8] who developed Electron Spectroscopy for Chemical Analysis (ESCA) for the study of solid surfaces, now simply known as X-ray photoelectron spectroscopy. Concurrently, Turner developed EUV PES and extended it to gas-phase samples.[9] These developments paved the way for

a plethora of experiments using PES, which today is one of the most widely used techniques for characterising the electronic structure of a large variety of systems, including solids, liquids, and gases, using a wide range of photon energies, from ultraviolet (UV) light to hard X-rays.[6,7,10–14] Moreover, PES has been employed extensively in time-resolved experiments, providing significant advantage to optical techniques since ionisation and detachment are always allowed provided there is enough photon energy to ionise or detach an electron.[11,13,15,16]

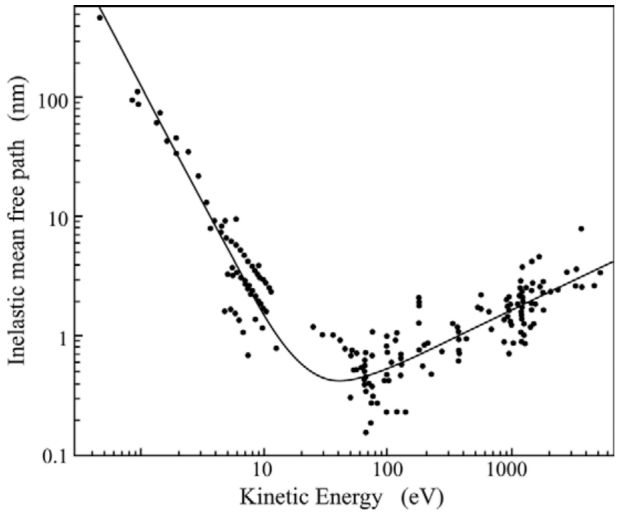

Figure 1.2: Universal curve for the electron inelastic mean free path in elemental solids plotted as a function of eKE. Data from Ref. 17. Reproduced from Damascelli, A., *Physica Scripta T* **2004**, *T109*, 61–74. Copyright IOP Publishing. Reproduced with permission. All rights reserved.

Emitted photoelectrons interact with the atoms and molecules of materials and undergo various scattering events before escaping through the surface of the sample. These interaction can be elastic, where only the direction of travel of the electrons is affected, or inelastic, where part of the electron's kinetic energy is transferred to the material through excitations, such as phonons, electronic excitations or impact ionisation. The inelastic mean free path (IMFP) of electrons is defined as the average distance between two inelastic scattering events, and it directly governs the escape depth of electrons. Figure 1.2 shows the relationship between the IMFP and the eKE of photoelectrons in elemen-

tal solids.[17] This 'universal curve' shows a minimum at around 50-100 eV and increases at both low and high eKEs. Because of these scattering processes and the limited IMFP of photoelectrons, PES is an inherently surface-sensitive technique, capable of probing only the outermost few nanometers of a material.

1.2 Liquid-microjet photoelectron spectroscopy

A key requirement of PES is that low enough pressures must be achieved in the experimental setup to avoid the absorption of incident radiation and, more importantly, scattering of electrons by gas molecules. Therefore, while solid and gas samples provide relatively easy targets, PES of liquids was initially limited to solutions with low vapour pressure (typically $\ll 1$ mbar),[18] as volatile liquids generate excessive pressure in the interaction chamber and undergo efficient evaporative cooling, ultimately freezing. This provided a serious limitation of PES since solutions are employed in many industrial processes and are the common medium for studying many biological systems. PES of liquids with low-volatility can be achieved using a variety of methods for generating liquid surfaces and replacing them quickly enough to avoid photoinduced charging, including liquid beams, wetted metal surfaces, and rotating cones.[18–20] Photoelectron spectra of pure methanol, ethanol, formamide, and ethylene glycol, electrolyte solutions in ethylene glycol and a cooled concentrated LiCl (7 M) aqueous solution were among those first recorded with these techniques.[18,19,21]

The application of PES to volatile liquids, particularly water, became feasible only in the 1990s with the development of liquid microjets.[22] A liquid microjet consists of a high-velocity, narrow-diameter liquid stream introduced into vacuum through a micrometer-sized nozzle. This stream maintains a laminar flow over several millimetres before breaking into droplets. To preserve vacuum conditions, the liquid is typically collected in a liquid nitrogen cold trap or removed via a catcher equipped with a small opening connected to a pumping system.[20,23]

The typical diameter D of liquid jets is on the order of 10-50 µm, which

is comparable to the mean free path (MFP) of water molecules at the vapour pressure of water at 0 °C (6.1 mbar) which has a value of ∼10 µm.[22] This satisfies the Knudsen condition for transitional flow (MFP ≈ D), where evaporating molecules experience a reduced number of intermolecular collisions.[22,24,25] As a result, due to the low local vapour pressure around the jet and small size of liquid jets, pressures between 10^{-4} mbar and 10^{-6} mbar can be achieved in experimental chambers, allowing for efficient detection of photoelectrons.

Another important effect of the small nozzle diameter is the generation of a high-velocity liquid flow (∼10-100 $\mathrm{m\,s^{-1}}$), which ensures rapid and continuous replacement of the liquid before it freezes as a result of evaporative cooling. This rapid replacement dramatically reduces photoinduced charging effects by constantly renewing the sample exposed to radiation. Additionally, the small nozzle size produces a laminar liquid flow, resulting in a constantly stable, uniform and smooth surface.

The development of liquid jets opened up new avenues for the investigation of electronic structure of solutions using liquid-microjet photoelectron spectroscopy (LJ-PES). The first LJ photoelectron spectra of pure water and several primary alcohols were reported in 1997 by Faubel et al.[29] They employed 21.218 eV photons from a He I discharge lamp to ionise liquid water. The resulting spectrum revealed the valence band structure of liquid water sitting on top of a large background of inelastically scattered photoelectrons, yielding a VIE for the highest occupied molecular orbital (HOMO) of water ($1b_1$) of 10.92 eV(Figure 1.3a). Subsequent experiments coupled synchrotron radiation, which has the advantage of providing tunability and higher photon flux, to liquid jets allowing for the investigation of the full valence band of water (VIE_{1b_1} = 11.16 eV, Figure 1.3b),[27] and of the O 1s peak (Figure 1.3c).[28] These studies demonstrated the feasibility and power of PES to investigate the electronic structure of liquid water. LJ-PES studies were soon extended to aqueous solutions and a large variety of aqueous systems have been studied to date, including alkali halides, inorganic salts, transition metal complexes

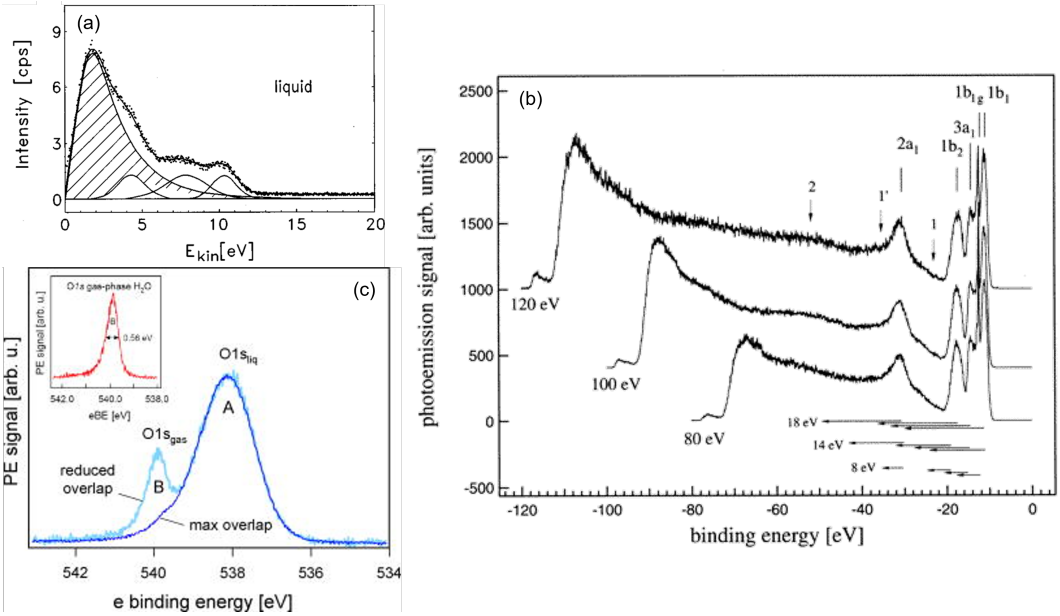

Figure 1.3: (a) First LJ photoelectron spectrum of water obtained with the He I line (21.218 eV) from a discharge lamp.[26] (b) First synchrotron LJ photoelectron spectra of water.[27] (c) First LJ spectrum of the O1s band of liquid water.[28] (a) Reprinted from Faubel, M., Steiner, B., Toennies, J. P., *J. Chem. Phys.* **1997**, *106*, 9013–9031, with the permission of AIP Publishing. (b) Reprinted with permission from Winter, B., Weber, R., Widdra, W., Dittmar, M., Faubel, M., Hertel, I. V., *J. Phys. Chem. A* **2004**, *108*, 2625–2632. Copyright 2004 American Chemical Society. (c) Reprinted from Winter, B., Aziz, E. F., Hergenhahn, U., Faubel, M., Hertel, I. V., *J. Chem. Phys.* **2007**, *126*, 124504, with the permission of AIP Publishing.

and nanoparticles.[30–37] These studies have typically relied on relatively high solute concentrations ($\gtrsim$ 100 mM) to ensure sufficient signal against the solvent background, which has limited the investigation of weakly soluble species such as many organic chromophores.[10]

1.3 Electrokinetic charging

A consequence of the high velocity of the liquid and small nozzle diameter is electrokinetic charging of the liquid stream.[31,38–40] This effect originates inside the nozzle, where an electric double layer forms at the interface between the liquid and the nozzle wall (Figure 1.4). In this interfacial region, the Stern layer, comprising ions closest to the wall, is tightly bound, while counterions in the diffuse layer are easily sheared off by the fast-flowing liquid. The resulting ion

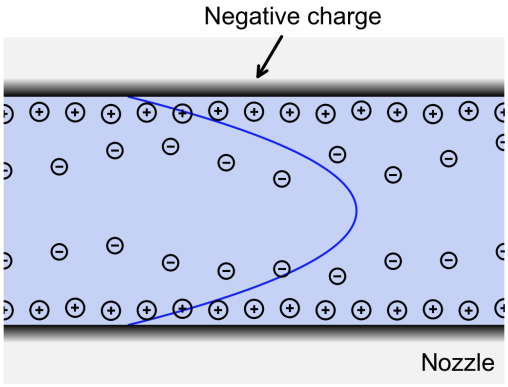

Figure 1.4: Diagram of the electric double layer inside a liquid jet nozzle. Nozzles are typically made of fused silica and hydration of silica forms negatively charged SiO^- groups at the liquid-glass interface. A layer of tightly bound positive ions (Stern layer) forms at the interface. The diffuse layer contains less strongly bound counterions which are rapidly displaced by the liquid. The blue line indicates the velocity profile of the liquid as a function of distance from the interface.

displacement generates a streaming potential, introducing a potential gradient between the liquid surface and the electron detector. Consequently, photoelectrons are accelerated or decelerated between the liquid jet and the detector, preventing the determination of accurate eBEs with LJ-PES. Experimental studies have demonstrated a strong dependence of the streaming potential on pH, flow rate, and ionic strength.[31,39,40] To correct its effect, two main methods have been commonly employed. The first method involves adjusting electrolyte concentration and flow rate to minimise the streaming potential.[31,40] This is typically verified by monitoring the ionisation of a gas, while moving the liquid jet away from the interaction region: a negligible streaming potential is achieved when the eKE distribution of the gas is independent of the jet's position.[31,40,41] The second method involves applying an external bias voltage to the liquid jet, which requires the addition of a salt to make the solution sufficiently conductive. The bias shifts the entire eKE distribution and exposes the full low eKE tail, which is observed for photon energies $\gtrsim$ 15 eV and comprises photoelectrons that have been inelastically scattered in the liquid (Figure 1.5). Its cutoff point represents electrons with 0 eKE, serving as a cali-

bration reference for the energy scale.[42] The VIE of water has been determined accurately to be 11.31 ± 0.04 eV using the first method,[31] and 11.33 ± 0.03 eV using the second method.[42] These values represent a significant improvement of the values obtained from earlier EUV and X-ray PES studies (10.92 eV,[29] 11.16 eV[27] and 11.23 eV[43]), in which the effect of the streaming potential was not accounted for fully.

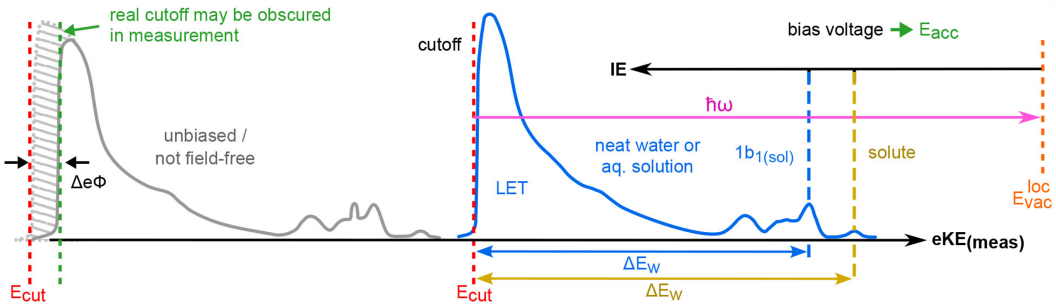

Figure 1.5: Diagram describing the application of a bias voltage to liquid jets to obtain accurate eBEs. The grey spectrum is obtained with no voltage applied and without accounting for the effect of the streaming potential, hindering the accurate determination of eBEs. The cutoff (E_{cut}) of the low energy tail (LET) may be obscured by the difference between the work function of the detector and the liquid ($\Delta e\Phi$). After applying a bias voltage the blue spectrum is measured. The full LET is revealed and E_{cut}, corresponding to 0 eKE, is employed to calibrate the eKE scale and obtain accurate eKE values (ΔE_W). E_{vac}^{loc} is the local vacuum level at the surface of the jet, $\hbar\omega$ is the photon energy. Adapted from Ref. 44, licensed under CC BY.

1.4 Probing depth in aqueous solution

Given the well-defined surface sensitivity of PES of solid surfaces, there has been a lot of interest in determining the probing depth of LJ-PES in water.[10,23,46–49] Two experimental studies have attempted to measure the effective attenuation length (EAL) of electrons in water (Figure 1.6).[46–48] The EAL is defined as the distance at which the flux of electrons that retain their initial eKE is $1/e$. The EAL is generally smaller than the IMFP and approaches the IMFP at high eKEs, as the elastic scattering cross sections become less important. Winter and co-workers estimated the EAL in water by measuring the O1s peak intensity across a range of eKEs (25-900 eV) with photon energies

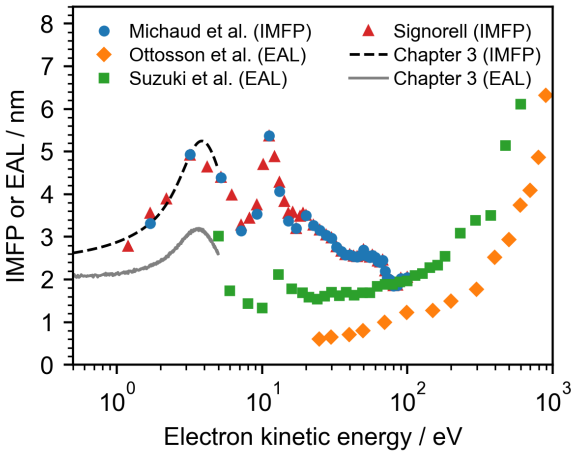

Figure 1.6: IMFP and EAL in liquid water and amorphous ice as a function of eKE. Blue circles: IMFP in amorphous ice.[45] Orange diamonds: EAL obtained from the intensity and photoemission anisotropy of the O1s peak of water,[46] as corrected in Ref. 47 (digitised data). Green squares: EAL determined from the relative intensity of the liquid and gas O1s peaks of water.[48] Red triangles: IMFP proposed by Signorell, based on amorphous ice cross sections[45] and photoelectron spectra of water droplets.[49] Dashed black line: IMFP obtained by interpolating the amorphous ice cross sections[45] with a cubic spline (Chapter 3). Gray solid line: EAL obtained from the Monte Carlo simulation described in Chapter 3 using the interpolated amorphous ice cross sections.

ranging 560-1440 eV, calibrating the absolute depth using the photoemission signals of Na^+ and I^-, and molecular dynamics simulations of their depth profiles.[46] After correcting for anisotropy in a subsequent study, they reported EALs below 1 nm for eKEs below 100 eV, monotonically increasing to around 6 nm at 900 eV.[47] In a later study, Suzuki and co-workers derived the EAL by comparing the O1s peak intensity of liquid water and water vapour recorded at photon energies ranging 540-1140 eV (eKE = 5-600 eV), assuming the same photoionisation cross-sections for both the liquid and gas.[48] Their results were consistent with the trend of the results of Winter and co-workers, showing no increase of the EAL at lower eKEs for eKEs above 20 eV. However, the absolute EAL values differed by a factor of approximately 2.

Signorell and co-workers subsequently derived scattering cross sections for low energy electrons (eKE $\lesssim$ 6 eV) in liquid water by adapting those measured in amorphous ice[45] and refining them through comparison of Monte Carlo sim-

ulations of electron transport in water with measured photoelectron spectra of water droplets.[49,50] Using the refined cross sections, the simulations were able to retrieve the true binding energy of the hydrated electrons from UV photoelectron spectra, despite the significant spectral distortion introduced by inelastic scattering of electrons with eKE $\lesssim$ 6 eV (see Section 1.5).[51] The IMFP obtained from the refined cross section which were extended to high eKEs by employing the amorphous ice cross sections is shown in Figure 1.6.[49] Additionally, Figure 1.6 shows the interpolated IMFP of electrons in amorphous ice below 5 eV (dashed line), and the EAL obtained from the Monte Carlo simulations using the interpolated cross sections, as described in Chapter 3.

1.5 Ultraviolet liquid-microjet photoelectron spectroscopy

Relatively few studies have focused on the electronic structure of small organic molecules in aqueous solution, particularly those of biological and atmospheric relevance.[52–64] Of particular interest are the valence band signals of these compounds as they contain information about the electronic states involved in chemical reactivity. However, X-ray and EUV LJ-PES studies have been limited to highly soluble compounds ($\gtrsim$100 mM), as solute signals often overlap with a strong water background.[10] This has hindered investigations of many poorly soluble organic compounds, such as DNA bases and protein chromophores,[10,42,64,65] despite their fundamental importance and considerable interest in their electronic properties.

An alternative approach involves the use of UV laser pulses to induce multiphoton ionisation of solutes in water, using photon energies $\lesssim$ 6 eV.[66] At these energies, UV photons do not have enough energy to directly ionise water molecules, thus concentrations as low as 20 µM can be used.[64] Furthermore, resonance-enhanced multiphoton ionisation (REMPI) can be employed to gain information about the excited state landscape of molecules. A small number of groups have investigated poorly soluble species in aqueous solu-

tion using UV LJ-PES.[62,65,67–70] However, these studies revealed that inelastic scattering of low-energy electrons in water significantly distorts photoelectron spectra. This distortion is less pronounced if high enough photon energies are employed ($h\nu \gtrsim 25$ eV),[71,72] because scattering of electrons with eKE $\gtrsim 15$ eV in water is dominated by electronic excitations, impact ionisation and electron attachment, which involve energy losses of several eV.[71] This results in a clear separation between the eKE distribution of scattered electrons and that of unscattered and elastically scattered electrons. Therefore, accurate eBEs can be extracted from X-ray and EUV photoelectron spectra. In contrast, scattering of photoelectrons with eKE < 6 eV formed after ionisation with UV light is dominated by small energy losses (< 1 eV), associated with excitation of translational, rotational, librational and vibrational modes of water. As a result, the nascent eKE distributions become distorted, preventing the determination of accurate eBEs with UV LJ-PES.

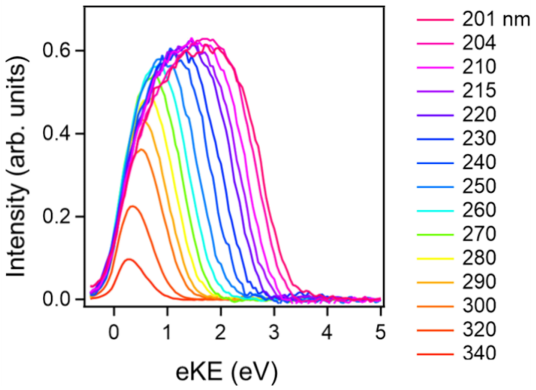

Figure 1.7: UV photoelectron spectra of the solvated electron recorded with wavelengths between 201 nm (6.17 eV) and 340 nm (3.65 eV). Adapted with permission from Yamamoto, Y. I., Suzuki, T., *J. Phys. Chem. A* **2023**, *127*, 2440–2452. Copyright 2023 American Chemical Society.

A notable example is the UV photoelectron spectrum of the hydrated electron, which has been recorded by several groups.[68–70,73–77] In these studies, solvated electrons were typically generated by promoting electrons to the charge-transfer-to-solvent (CTTS) states of I^- or $Fe(CN)_6^{4-}$ with a UV pulse. After a delay of several picoseconds, the photoelectron spectrum of the solvated electron was recorded with a second UV pulse. These experiments

yielded values for the eBE of the solvated electrons between 3.3 and 4.5 eV, with a significant dependence on photon energy, and consequently eKE (Figure 1.7).[68–70,74–77] Subsequent measurements of the hydrated electron using a EUV probe beam provided an accurate value for its eBE of 3.76 ± 0.05 eV.[78] These results highlighted the role of inelastic scattering of photoelectrons in water in hindering the determination of accurate eBEs when using UV light.

Successive efforts focused on gaining a deeper understanding of inelastic scattering of low-energy electrons in water and developing methods to account for spectral distortion in UV photoelectron spectra. A detailed account of these methods is presented in Chapter 3, so only a brief description is outlined here. Signorell and co-workers developed a Monte Carlo simulation to model the propagation of electrons in liquid water and their escape into vacuum,[51] employing scattering cross sections based on amorphous ice cross sections[45] and PES data of water droplets.[50] Suzuki and co-workers later introduced an empirically based spectral inversion method.[77,78] They employed the EUV spectrum of the solvated electron shifted to match UV photon energies and mapped it to the corresponding UV photoelectron spectra. By fitting a linear combination of these UV spectra to experimental data, the expansion coefficients were used to reconstruct true eKE distributions using the shifted EUV spectra. Our group combined these two approaches by employing Monte Carlo simulations to obtain the linear transformation between measured and true spectra required for spectral inversion.[79] Additionally, our approach was unique in that it accounts for non-uniform concentration depth profiles, which are common for poorly soluble organic molecules. Although these methods have significantly improved the interpretation of UV PES data, there remains some controversy over the choice of parameters employed in spectral retrieval procedures, such as the scattering cross sections and the value of the escape threshold electrons must overcome at the surface of the liquid.[49,51,79–82]

1.6 Outlook

The work presented in this thesis focuses on undertaking a systematic investigation of the parameters employed in Monte Carlo simulations of electron transport in liquid water and spectral retrieval of liquid-microjet photoelectron spectra, which are benchmarked against the photoelectron spectra of water, phenol and phenolate (Chapter 3). The refined parameters are then applied in Chapter 4 with the aim to obtain accurate eBEs from the UV photoelectron spectra of the photoactive yellow protein chromophore in aqueous solution. These results are complemented by EUV and X-ray photoelectron spectra. Chapter 5 describes experiments that employ UV pump-UV probe LJ-PES to record time-resolved photoelectron spectra of the photoactive yellow protein chromophore in aqueous solution. These experiments allow for the investigation of the excited state dynamics of the chromophore providing insight into its relaxation pathways and timescales.

Chapter 2

Experimental Methods

This chapter describes the UCL experimental setup and procedures employed for the collection of UV photoelectron spectra (PES) and UV-pump UV-probe time-resolved photoelectron spectra (TRPES) of the photoactive yellow protein chromophore analogue pCE$^-$ in aqueous solution (Chapters 4 and 5). UV PES and TRPES were recorded using the Ultrafast Laser Facility at University College London (UCL). Complementary EUV photoelectron spectra of pCE$^-$ were recorded in Bernd Winter's laboratory at the Fritz Haber Insitute (Berlin) in collaboration with Iain Wilkinson, and the key experimental details and analysis procedure are described in Chapter 4.

2.1 Femtosecond laser setup

The UCL femtosecond laser system is based on the commercially-available Coherent Astrella-HE laser. The Astrella-HE laser includes a mode-locked 80 MHz Ti:Sapphire laser (Vitara, Coherent) that is pumped by a continuous-wave 532 nm Nd:YLF laser (Verdi, Coherent) and produces femtosecond pulses with a central wavelength of 800 nm. The femtosecond pulses are propagated into a regenerative amplifier in which a Ti:Sapphire crystal is pumped by a 1 kHz nanosecond 527 nm Nd:YLF laser (Revolution, Coherent). Pulses are outputted at a 1 kHz rate with an energy of 9 mJ and a duration of 32 fs. 1.22 mJ of the output is employed to pump a commercially-available optical parametric amplifier (OPA, Coherent OPerA Solo) that generates pulses

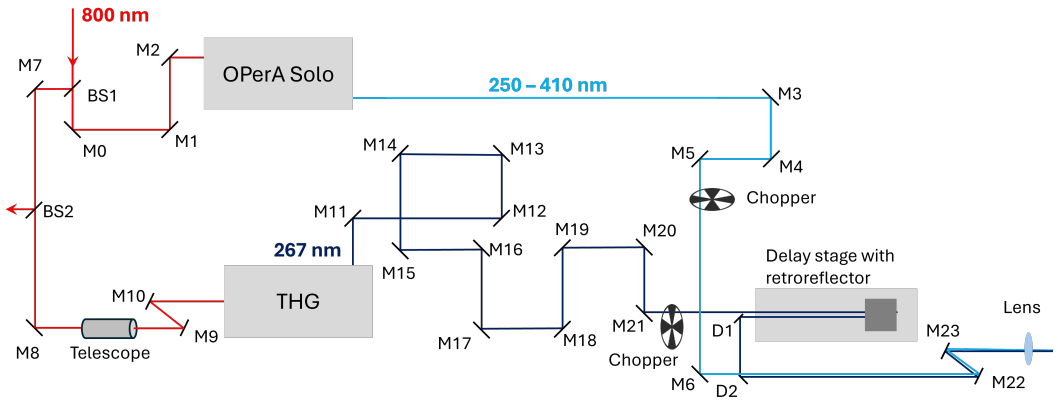

Figure 2.1: Diagram of the optical layout. The Astrella-He generates 800 nm pulses at a 1 kHz rate (red). A portion of the output is used to generate tunable pulses with an OPA (Coherent OPera Solo). Pulses between 250 and 410 nm were employed in this work (light blue). The OPA output may be used to record one-colour photoelectron spectra or as the pump for time-resolved experiments. For time-resolved experiments, another portion of the 800 nm is employed to generate 266.7 nm probe pulses via THG (dark blue). The pump and probe pulses are chopped at a rate of 250 Hz. The probe pulse is delayed using a retroreflector mounted on a delay stage and reflected from a D-mirror (D2) to achieve near collinearity with the pump pulse. The pump and probe beams are focused into the chamber using a lens with a 300 mm focal length. Beam splitters are labelled BS1 and BS2, mirrors are labelled M1-M23, and D-mirrors are labelled D1 and D2.

with wavelengths in the range 235-2600 nm. 1.47 mJ of the 800 nm pulse is employed to generate 266.7 nm pulses via third-harmonic-generation (THG) employing two β-barium-borate (BBO) crystals. For one-colour experiments only the OPA laser is employed, while for two-colour time-resolved experiments both the OPA and THG are employed. The 266.7 nm pulse is delayed with respect to the pulse from the OPA using a retroreflector mounted on a 325 mm delay stage (Newport, DL325), after which the probe pulse is reflected from a D-mirror to achieve near collinearity between the pump and probe pulses. Choppers (Thorlabs, MC1F10 blades, MC2000 controller) are placed in both the pump and probe paths and set at 250 Hz with a phase difference of 90°, in order to achieve pump-only, probe-only, pump-probe and background shots. Both pulses are focused into the interaction region of the liquid-microjet photoelectron spectrometer with a lens with a 300 mm focal length. A diagram of

the optical layout is shown in Figure 2.1.

2.2 UV liquid-jet photoelectron spectroscopy

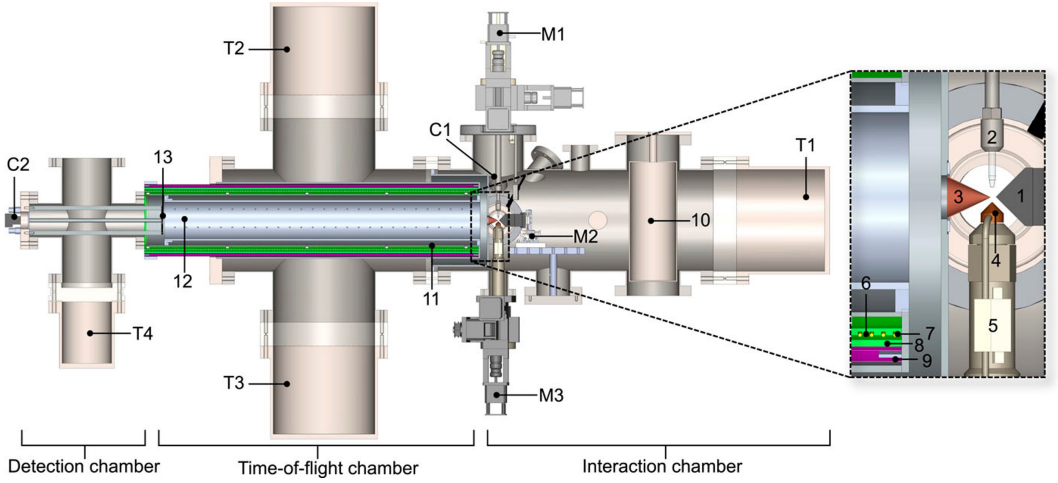

Figure 2.2: Diagram of the liquid-microjet photoelectron spectrometer employed in this experiment. The spectrometer is made up of three major parts: the interaction chamber, the time-of-flight chamber and the detection chamber. The inset shows (1) the magnet, (2) the liquid-microjet assembly, (3) the skimmer, (4) the liquid catcher, (5) the catcher's heater, (6) a polytetrafluoroethylene sleeve with a groove for the (7) solenoid, (8) an outer polytetrafluoroethylene sleeve and (9) a double µ-metal tube. In the setup employed in this work the catcher (4) was replaced by a liquid-nitrogen cold trap at the bottom of the chamber. A (T1) 1000 $\mathrm{L\,s^{-1}}$ turbomolecular pump and (10) a liquid-nitrogen cold trap differentially pump the interaction chamber. Three *xyz*-manipulators are responsible for translating (M1) the liquid-microjet, (M2) the magnet and (M3) the catcher. A CMOS camera (C1) is used to monitor the alignment. The time-of-flight chamber contains (11) a flight tube and (12) a drift tube and high vacuum is achieved thanks to two 600 $\mathrm{L\,s^{-1}}$ turbomolecular pumps (T2 and T3). The detection chamber contains (13) a double-stack microchannel plate detector and (C2) a CMOS camera to monitor the fluorescence of a phosphor screen placed behind the microchannel plates. The detection chamber is pumped with (T4) a 220 $\mathrm{L\,s^{-1}}$ turbomolecular pump. Reprinted from Riley, J. W., Wang, B., Parkes, M. A., Fielding, H. H.*Rev. Sci. Instrum.* **2019**, *90*, 083104, with the permission of AIP publishing.

A magnetic-bottle time-of-flight (TOF) photoelectron spectrometer was employed to perform the UV LJ-PES experiments outlined in this work (Figure 2.2).[41] The instrument consists of an interaction chamber, a TOF region and a detection region. The interaction chamber is pumped with a 1000 $\mathrm{L\,s^{-1}}$

turbomolecular pump (Leybold, TURBOVAC 1000c, component T1 in Figure 2.2) and a liquid-nitrogen cold trap (component 10 in Figure 2.2). The turbomolecular pump is backed by a rotary vane pump (Edwards E2M28), which is particularly effective at handling the high water vapour load of the interaction region. The stainless steel liquid-nitrogen cold trap has a surface area of ∼764 cm^2 and is cleaned after each liquid-jet measurement with deionised water and acetone to ensure optimal pumping efficiency. The TOF region is differentially pumped by two 600 $L\,s^{-1}$ turbomolecular pumps (Leybold TURBOVAC 600c) placed above and below the TOF tube (components T1 and T2 in Figure 2.2) and backed by a scroll pump (Leybold, ECODRY 35 plus). The MCP region is pumped by a 250 $L\,s^{-1}$ turbomolecular pump (Edwards, EXT250, component T4 in Figure 2.2) placed behind the MCP plates and backed by a scroll pump (Leybold, SC15D). The interaction and TOF regions backing pumps can also be connected directly to the chamber to achieve pressures around 10^{-2} mbar when pumping down the instrument. During liquid jet experiments, pressures between 7×10^{-5} and 1.0×10^{-4} mbar are achieved in the interaction region and pressures around 5×10^{-7} and 6×10^{-7} mbar are maintained in the TOF and detector regions, respectively.

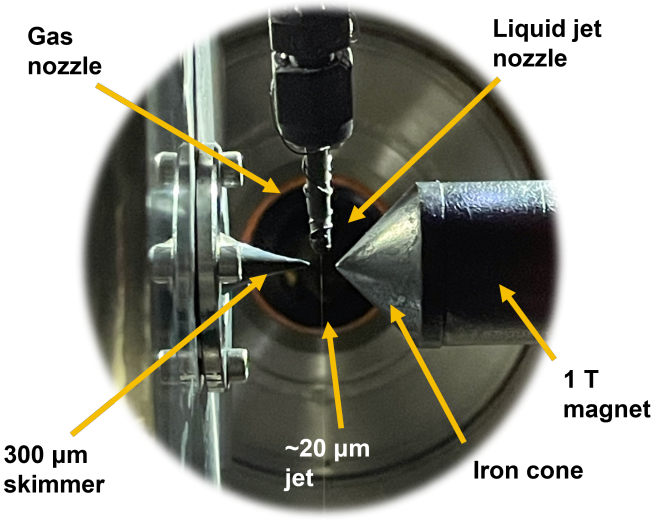

Figure 2.3: Annotated photograph of the interaction region under experimental conditions. The laser pulses propagate in the direction perpendicular to the plane of the photograph

A photograph of the interaction region is shown in Figure 2.3. The solution of interest is flowed through a 20 µm fused silica nozzle with a high-performance liquid chromatography pump (Microliquids 02). Typical flow rates are between 0.5 $\mathrm{mL\,min^{-1}}$ and 1.0 $\mathrm{mL\,min^{-1}}$ with backing pressures between 50 and 100 bar for aqueous solutions. Low flow rates are preferred, as they result in lower pressures in the interaction chamber and longer collection times. The flow rate must be carefully adjusted, together with electrolyte concentration, to ensure a flat electrostatic potential in the interaction region (see Section 2.2.1.3). The liquid retains a laminar flow for 3-4 mm before breaking into droplets and is intersected by the femtosecond laser in the laminar region 1-2 mm below the nozzle. Originally, a catcher with a 500 µm opening was placed a few mm under the liquid jet nozzle to collect the liquid. However, the motors used to translate the jet and catcher were broken at the time the experiments reported in this thesis were conducted. Therefore, a liquid-nitrogen cold trap with an entrance diameter of ∼2.4 cm and a volume of ∼530 mL was employed to freeze the liquid sample and placed ∼30 cm below the nozzle. A gas nozzle is also present in the interaction region to introduce Xe and NO gases, which are necessary for energy calibration. The liquid microjet is placed between a 1 T magnet with an iron cone tip and a 300 µm skimmer that separates the interaction region from the time-of-flight region, at a distance of ∼1 mm from both. The magnet, the skimmer, the liquid-jet nozzle and the gas nozzle are regularly coated with colloidal graphite to achieve a uniform vacuum level in the interaction region. The magnet, liquid-jet nozzle and gas nozzle are removed from the chamber and coated with colloidal graphite by either spraying or applying the coating with a small paintbrush. The skimmer is coated in situ using a small paintbrush. A copper wire is also wrapped around the nozzle before coating it in graphite and connected to the grounded jet assembly to reduce accumulation of charge on the surface of the nozzle. The time-of-flight region consists of a 630 mm drift tube in which photoelectrons are directed to the detector by a weak 2 mT homogeneous magnetic

field generated by a solenoid set at a constant current of 4.00 A (component 7 in Figure 2.2). In the detection region, a double-stacked microchannel plate (MCP) detector placed in front of a phosphor screen is responsible for the detecting electrons (BOS-25, Beam Imaging). Under normal operation, the front MCP is grounded, the back MCP is set to a voltage of 1900 V and the phosphor plate is set to 2200 V. The voltage of the phosphor plate can be set to 5000 V to visualise the electron signal with a CMOS (complementary metal-oxide semiconductor) camera, and aid alignment of the laser and sample. The signal generated by electrons hitting the phosphor plate is decoupled using a capacitor and the flight time relative to a laser trigger obtained from a photodiode placed near the exit of the Astrella-He system is collected by a digitiser card (Keysight U5309A) and binned in 0.5 ns steps.

2.2.1 Experimental considerations and data processing

Figure 2.4 shows the steps required to transform the TOF data obtained from the spectrometer to photoelectron spectra as a function of eKE. The retrieval of the photoelectron distributions prior to inelastic scattering of electrons in water is also shown. The following sections will describe these processes in detail.

2.2.1.1 Time of flight to electron kinetic energy calibration

Since the experimental data is collected as a histogram of electron counts versus TOF, a calibration curve is obtained to convert TOF to eKE. Their relationship is given by

$$\mathrm{eKE}(t) = \frac{m_\mathrm{e}}{2}\left(\frac{s}{\mathrm{TOF} - t_0}\right)^2 - E_0 \tag{2.1}$$

where m_e is the mass of an electron, s is the flight distance, t_0 is a time offset to account for the delay between the trigger and the laser and E_0 indicates the difference between the vacuum level in the interaction region and at the detector. The calibration is carried out by recording multiphoton photoelectron spectra of the NO ($\mathrm{X}^2\Pi_{1/2}$, $v'' = 0$) $\rightarrow$ NO^+ ($\mathrm{X}^1\Sigma^+$, v^+) vibronic transitions and the

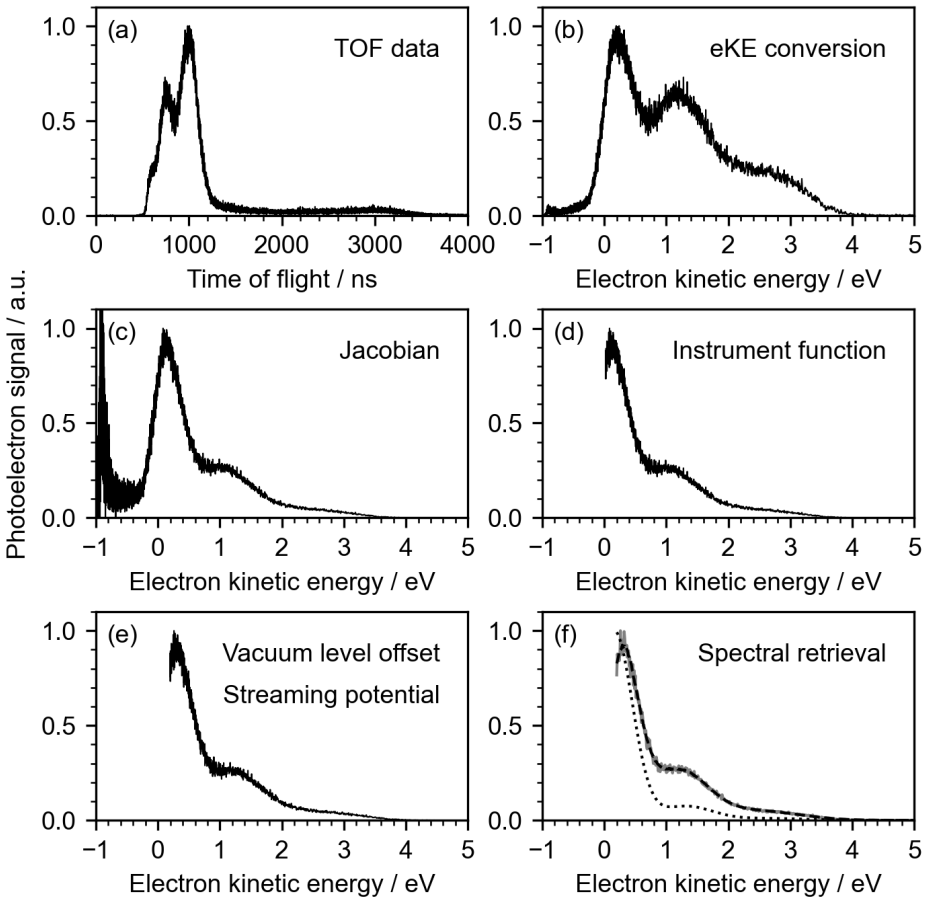

Figure 2.4: Steps to convert time-of-flight data to photoelectron spectra. (a) The TOF data of $p\mathrm{CE}^-$ recorded at 350 nm. (b) TOF was converted to eKE. (c) A Jacobian transformation was applied to the photoelectron counts. (d) The intensity of the spectrum was divided by the eKE-dependent collection efficiency of the spectrometer and the spectrum was cut off at 90% collection efficiency. (e) The spectrum was shifted by the difference between the potential at the liquid jet and the detector. (f) The true photoelectron distribution prior to any inelastic scattering in the liquid (dotted black line) was obtained by fitting the spectral retrieval (dashed black line) to the spectrum (solid gray line).

Xe $^1\mathrm{S}_0 \rightarrow {}^2\mathrm{P}_{3/2,\,1/2}$ transitions, which have well-known ionisation energies,[83,84] using wavelengths between 238 nm and 267 nm in the absence of the jet in the chamber (Figure 2.5). Photoionisation of NO occurs as a three-photon process when using 267 nm and a two-photon process when using wavelengths between 237 and 250 nm. Photoionisation of Xe occurs as a [2+1] resonant process when using 249.7 nm. This ensures that the full eKE range between 0 and 5 eV is covered. An example calibration curve is presented in Figure 2.6a.

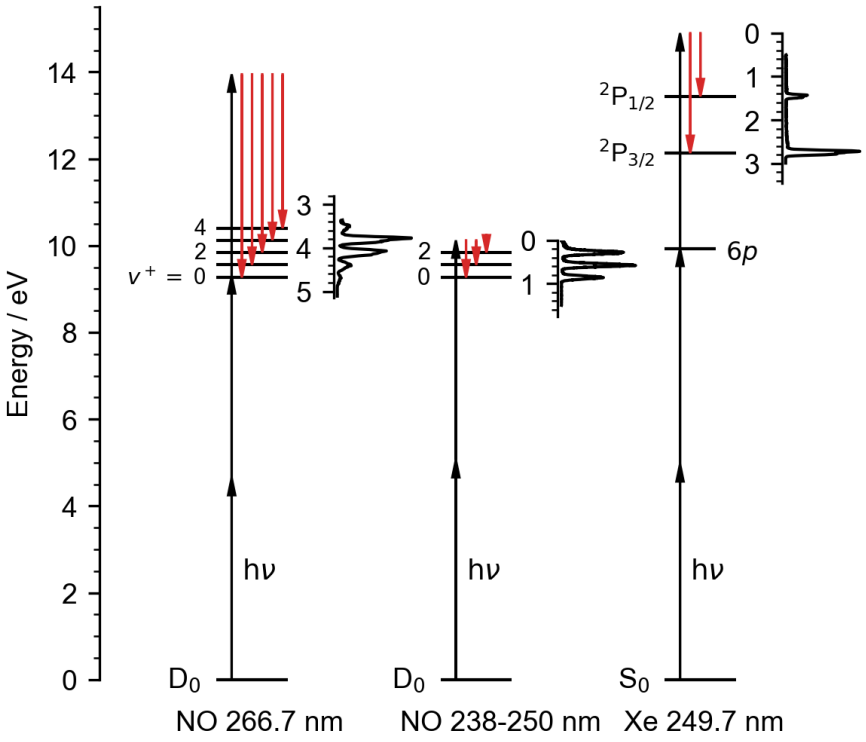

Figure 2.5: Energy diagram descibing the ionisation processes of NO and Xe employed in the energy calibration and determination of the collection efficiency of the spectrometer. Left: The three-photon photoelectron spectrum of NO is recorded at 266.7 nm. Two-photon photoelectron spectra of NO are recorded between 238 and 250 nm. The three-photon resonance-enhanced photoelectron spectrum of Xe is recorded at 249.7 nm. Black arrows indicate the energy of one photon and red arrows indicate the eKE of the photoelectrons. Example photoelectron spectra are shown as a function of eKE. The ionisation potentials of NO and Xe are taken from Refs 83 and 84, respectively.

As NO slowly adsorbs onto the graphite in the interaction region, the work function of the surfaces around the ionisation point changes, causing a shift in the vacuum level. This results in a shift in the recorded TOF (and eKE) of the photoelectron spectra of the calibration (Figure 2.6b). Therefore, NO is left in the chamber for more than 2 hours at a constant interaction chamber pressure (typically ranging 5×10^{-5} and 1×10^{-4} mbar) before recording the calibration spectra to allow the system to equilibrate. As NO and Xe cannot be simultaneously introduced into the chamber, the photoelectron spectrum of Xe is recorded last, quickly after switching from NO to Xe, to ensure minimal

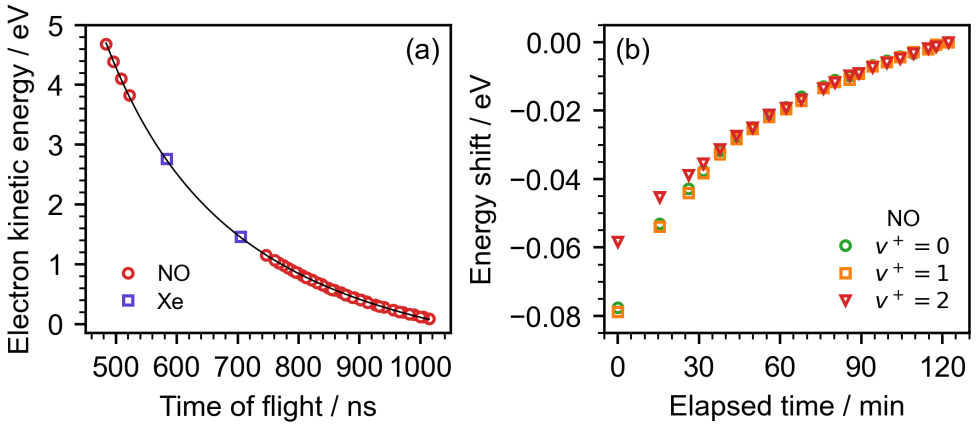

Figure 2.6: (a) Example calibration curve. Central eKE of the of the NO ($X^2\Pi_{1/2}$, $v'' = 0$) $\rightarrow$ NO^+ ($X^1\Sigma^+$, v^+) vibronic transitions and the Xe $^1S_0 \rightarrow {}^2P_{3/2,\,1/2}$ transitions as a function of time-of-flight. The solid line indicates the fit of Equation 2.1. (b) Shift in the central eKE of the first three vibronic transitions of NO as a function of time elapsed from the introduction of NO into the chamber recorded with 249.7 nm. The shift of the $v^+ = 2$ transition deviates from the trend because the collection efficiency of low energy electrons is lower at lower eKEs.

desorption of NO.

Due to the non-linear relationship between TOF and eKE, a Jacobian transformation is applied to correct for the varying density of data points, as low eKE values are compressed and high eKE values are stretched. The Jacobian takes on the following form:

$$\int_a^b S\left(\mathrm{eKE}\right)\, d\mathrm{eKE} = \int_d^c S\left(\mathrm{eKE}\left(t\right)\right) \cdot m_\mathrm{e} \cdot \frac{s^2}{\left(t - t_0\right)^3}\, dt \tag{2.2}$$

where a and b are two consecutive TOF (t) values, c and d are the respective eKE values and S is the photoelectron signal.

2.2.1.2 Instrument function characterisation

The collection efficiency of the photoelectron spectrometer is lower at low eKEs. In order to quantify this phenomenon, one-colour two-photon photoelectron spectra of NO are recorded at several wavelengths (Figure 2.7a). The peaks of the $v^+ = 0,\ 1,\ 2,\ 3$ vibronic transitions of NO are fit with Gaussians and the heights of the $v^+ = 1, 2, 3$ transitions are normalised to the $v^+ = 0$

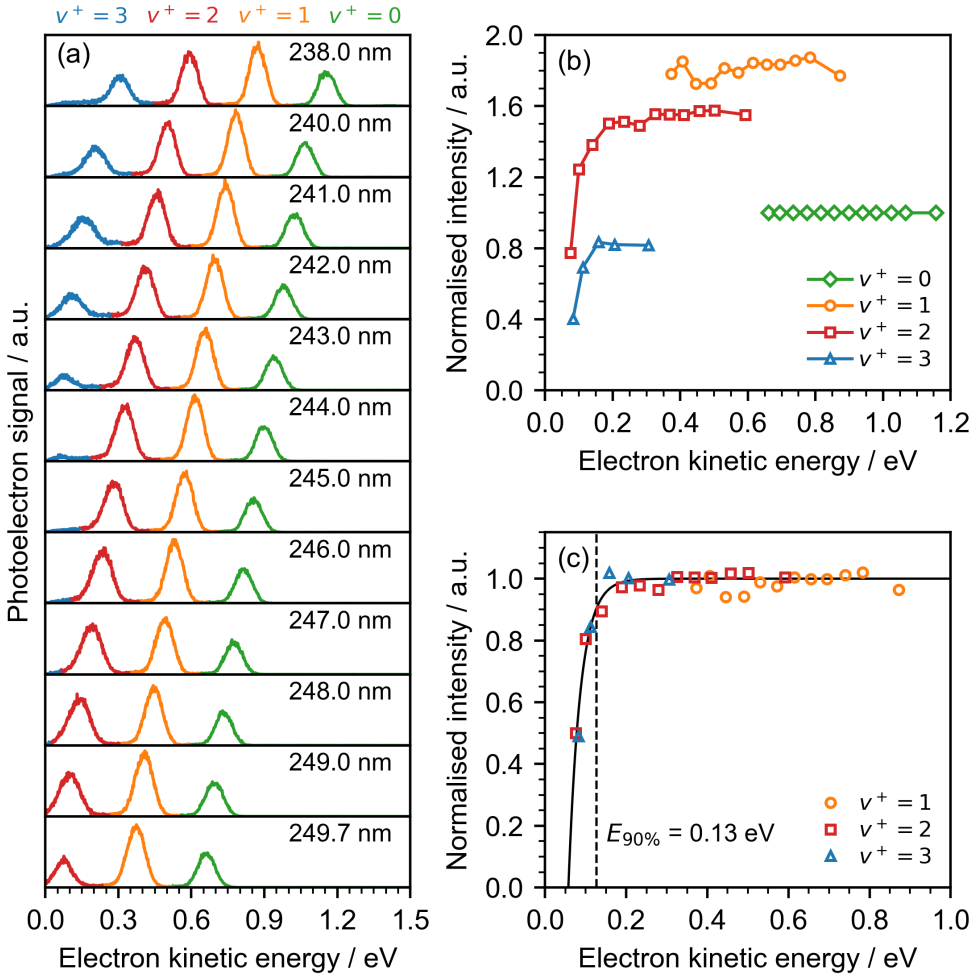

Figure 2.7: (a) Photoelectron spectra of NO recorded with different wavelengths. The $v^+ = 0, 1, 2, 3$ vibronic transitions are highlighted in green, orange, red and blue, respectively. The intensity of the peaks decreases with decreasing eKE due to the reduced collection efficiency of electrons below ~0.3 eV. (b) Intensities of the $v^+ = 0$ (green diamonds), $v^+ = 1$ (orange circles), $v^+ = 2$ (red squares) and $v^+ = 3$ (blue triangles) vibronic transitions of NO as a function of eKE normalised to the $v^+ = 0$ transition in each spectrum. (c) Intensities of the $v^+ = 1$ (orange circles), $v^+ = 2$ (red squares) and $v^+ = 3$ (blue triangles) vibronic transitions of NO as a function of eKE normalised to the average intensity above 0.3 eV. The data were fit with a cumulative exponential distribution (solid line). Photoelectron spectra are cutoff at 90% collection efficiency, which corresponds to an eKE of 0.13 eV in this case.

transition (Figure 2.7b). Each set of peak heights is then normalised to the average height of the peaks above ~0.3 eV eKE, which are unaffected by the reduced collection efficiency of the spectrometer (Figure 2.7c). The normalised

peak heights are then fit with a cumulative exponential distribution

$$I(\mathrm{eKE}) = 1 - e^{(\mathrm{eKE}-E_{\mathrm{cut}})/\tau} \tag{2.3}$$

where $I(\mathrm{eKE})$ is the peak height of the NO vibronic transitions or the collection efficiency, E_{cut} is the x-intercept which approximately indicates the cutoff for low energy electrons and τ is the scale parameter of the exponential. Photoelectron spectra are divided by $I(\mathrm{eKE})$ and cut off at 90% collection efficiency (Figure 2.4d). Typically, excellent instrument functions are obtained with 50% collection efficiency at eKEs $\lesssim 0.1$ eV and cutoff values below 0.2 eV.

2.2.1.3 Streaming potential and vacuum-level offset

Figure 2.8 shows important components of the spectrometer employed in UV LJ-PES experiments. When the liquid jet is not in the interaction chamber, the work function of the surfaces of the magnet, gas nozzle and skimmer are all equal, as they are coated in colloidal graphite. This results in a flat potential in the interaction region (Figure 2.8a). The addition of the liquid jet can cause a potential gradient between the ionisation point and the walls of the interaction chamber, which can accelerate or decelerate photoelectrons before they reach the detector (Figure 2.8b). This occurs because the liquid jet nozzles employed in this work were made of fused silica, which can undergo hydroxylation in contact with water, forming silanol groups on the inner surface of the nozzle. These groups are affected by the pH of the solution and, at pH values greater than ∼2, the surface of silica is negatively charged,[85,86] leading to the formation of an electric double layer at the glass-liquid interface. As the outer layers are loosely bound and the velocity profile of the liquid increases as a function of distance from the interface, a build-up of charge can occur in the liquid, inducing a streaming potential. The streaming potential can raise or lower the vacuum level of the surface with respect to the vacuum level in the interaction region, thus affecting the velocity of photoelectrons. Several parameters affect the magnitude of the streaming potential, including ionic

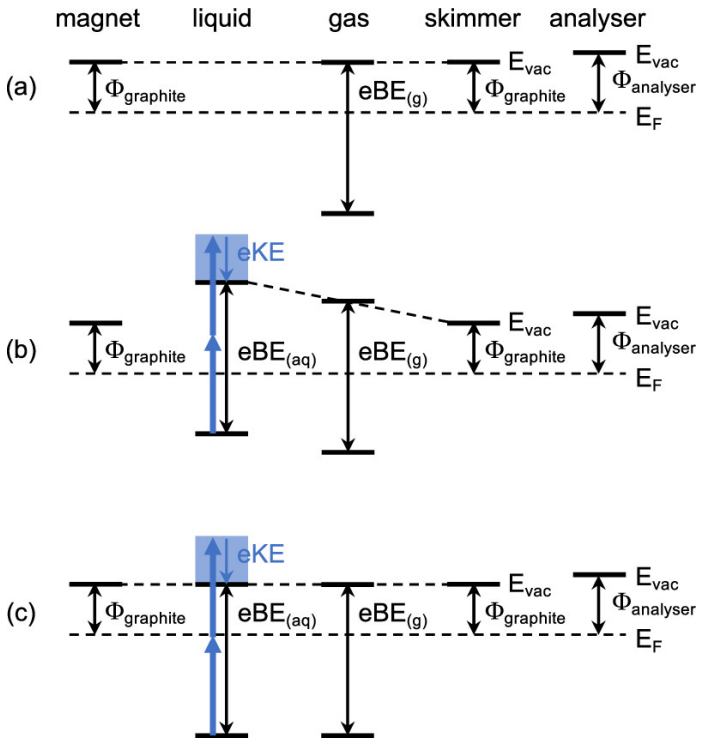

Figure 2.8: Schematics of the energy levels of key components of the photoelectron spectrometer. (a) In the absence of the liquid jet, there is no potential gradient in the interaction region. (b) Upon addition of the liquid jet, the potential at the surface of the liquid causes a potential gradient in the interaction region, which can cause electrons to accelerate or decelerate before reaching the detector. (c) After adjusting the concentration of electrolytes in liquid or the flow rate of the liquid jet, the potential in the interaction region can be flattened. Reproduced from Ref. 66, licensed under CC BY.

strength, pH, flow rate and temperature.[40] These can be adjusted in order to ensure a flat potential in the interaction region, i.e., the potential on the surface of the jet is the same as on the surface of the magnet and skimmer (Figure 2.8c).

An alternative approach is to apply a voltage to the solution, which, if the solution is made sufficiently conductive by adding a salt, maintains the jet at a fixed potential, and shifts the photoelectron spectra by a constant eKE value.[42] This method is particularly effective for LJ-PES measurements employing photon energies greater than ∼10 eV, as spectra are characterised by a low eKE tail made up of inelastically scattered electrons. The low eKE tail

sharply drops off to 0 at 0 eKE and can be used to determine the difference in potential between the liquid jet surface and the detector.[42] In the UV LJ-PES measurements undertaken at UCL, the concentration of NaOH and the flow rate of the liquid jet were adjusted. In the EUV measurements undertaken at the Fritz Haber Institute in Berlin, a bias was applied and the energy scale was referenced to the low eKE cutoff (Chapter 4).

When the liquid jet is introduced in the interaction chamber, evaporation of water molecules from its surface results in a significant adsorption of water molecules onto the walls of the chamber. Similarly to NO, the adsorption of water shifts the vacuum level in the interaction chamber, which can cause acceleration or deceleration of electrons between the interaction region and the detector. This shift is referred to as the vacuum level offset in this work, and must be measured in order to obtain accurate eKEs.

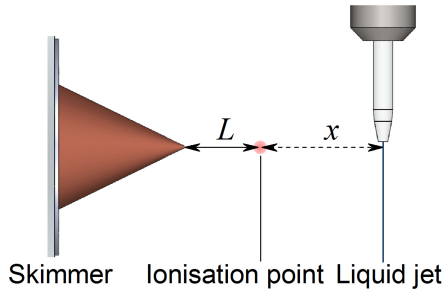

Figure 2.9: Diagram of the interaction region highlighting the geometry employed when determining ϕ_{str} and V_0. L, the distance between the ionisation point and the skimmer, remains constant. x, the distance between the liquid jet and the ionisation point, changes during the measurement. Adapted from Riley, J. W., Wang, B., Parkes, M. A., Fielding, H. H.*Rev. Sci. Instrum.* **2019**, *90*, 083104, with the permission of AIP publishing.

In order to quantify the vacuum level offset V_0 and measure the difference between the vacuum level at the surface of the jet and at the skimmer induced by the streaming potential ϕ_{str}, photoelectron spectra of Xe are recorded while the liquid jet is translated at set distances from the interaction region along the skimmer magnet axis (Figure 2.9). The rising edge of the Xe $^1S_0 \rightarrow {}^2P_{3/2}$ transition are fit with a Gaussian and the peak centres are fit with the following

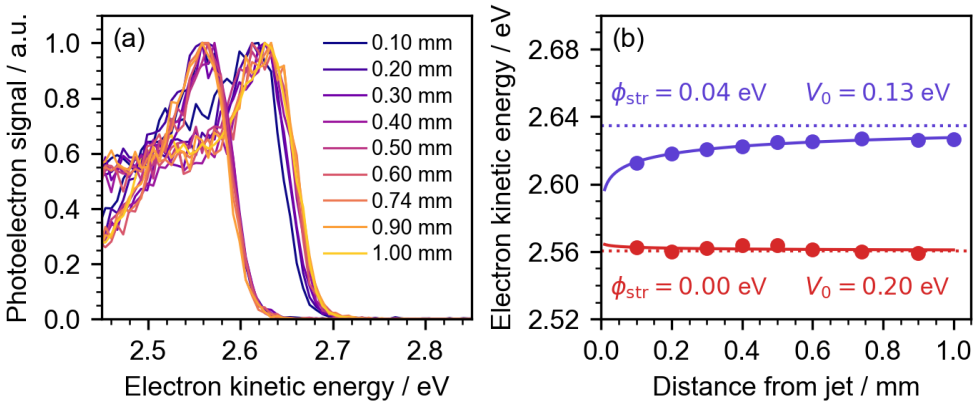

Figure 2.10: (a) Photoelectron spectra of the $^2P_{3/2}$ peak of Xe following [2+1] photoionisation at 249.7 nm recorded at set distances between the ionisation point and the liquid jet. The spectra at higher eKEs were recorded before a set of liquid jet measurements and the spectra at lower eKEs were recorded after a set of liquid jet measurements. (b) Measured eKE of the $^2P_{3/2}$ peak of Xe following [2+1] photoionisation at 249.7 nm as a function of distance from the liquid jet. The data were measured before (violet) and after (red) a set of liquid jet measurements. Solid lines indicate the fit of Equation 2.4 and dotted lines the asymptote at large distances, which corresponds to $\mathrm{eKE}_{\mathrm{true}} - V_0$.

equation[31]

$$\mathrm{eKE}_{\mathrm{obs}}(x) = \mathrm{eKE}_{\mathrm{true}} - \phi_{\mathrm{str}} \frac{\ln\left(\frac{2\mathrm{L}+x}{x}\right)}{\ln\left(\frac{2(\mathrm{L}+x)-r}{r}\right)} - V_0, \tag{2.4}$$

where $\mathrm{eKE}_{\mathrm{obs}}(x)$ is the peak eKE when the jet is translated by a distance x away from the interaction region, $\mathrm{eKE}_{\mathrm{true}}$ is the field-free eKE, L is the distance between the ionisation point and the skimmer and r is the radius of the jet. Under experimental conditions, $x = r$, i.e. the potential at the interaction region is given by the potential at the surface of the jet, and Equation 2.4 reduces to

$$\mathrm{eKE}_{\mathrm{obs}} = \mathrm{eKE}_{\mathrm{true}} - \phi_{\mathrm{str}} - V_0. \tag{2.5}$$

Since the vacuum level offset changes during the duration of the measurement as more water molecules adsorb onto the surfaces of the interaction

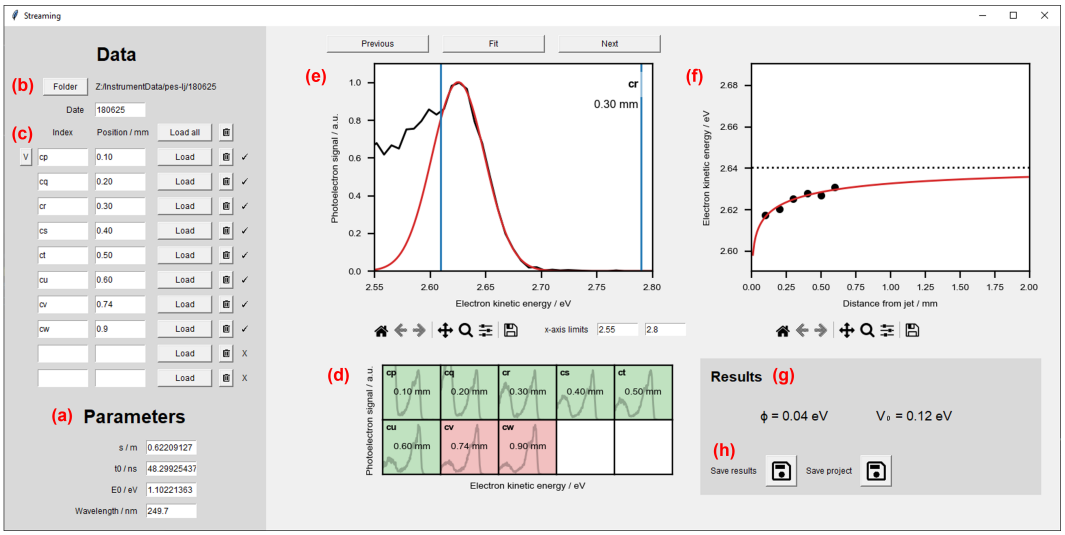

Figure 2.11: Graphical user interface of the software for on-the-fly determination of ϕ_{str} and V_0. (a) The TOF-to-eKE conversion parameters and the wavelength employed are obtained from a settings file that defines default quantities, which can be adjusted here. (b) The folder with the TOF data of the Xe spectra is selected and the date of the measurements in DD-MM-YY formate is inserted. (c) The file index of the TOF spectra and the liquid jet position at which they were recorded is inserted. Default positions are obtained from the settings file, and can be adjusted here. Inserting the first file index and pressing the downward arrow autofills the boxes that have a position with subsequent file indices. The spectra can be loaded with the "Load all" button or loaded individually. They can also be removed by pressing the "bin" button. (d) Once loaded a summary of the spectra is shown. A red background indicates that the spectrum has not yet been fit. Clicking on a spectrum in (d) displays the spectrum in (e). Here, clicking and dragging on the plot defines the fitting limits (blue lines) so that only the rising edge and the peak are fit with a Gaussian. Clicking "Fit" results in fitting a Gaussian to the spectrum within the fitting limits; the background of the spectrum in (d) turns green and the peak position is plotted in (f). "Previous" and "Next" can be clicked to switch between spectra. (f) After at least three peak positions have been determined Equation 2.4 is fit to the data, and (g) ϕ_{str} and V_0 are displayed. (h) Clicking on save results creates a yaml file that includes ϕ_{str}, V_0, the folder, date, file indices, liquid jet positions, peak eKEs, calibration parameters and wavelength.

region, the potential in the interaction cannot be fully flattened. Instead, ϕ_{str} is kept below an absolute value of 0.08 eV and it is measured together with the vacuum level offset before and after a set of measurements. An example measurement is shown in Figure 2.10. Measured photoelectron spectra are shifted

by the average of the sums of ϕ_{str} and V_0 (Figure 2.4e). The sums typically vary by a few tens of meV over the course of a measurement.

Software with a graphical user interface (GUI) was written in Python to determine ϕ_{str} and V_0 on the fly during measurements. Previously, the analysis was carried out in Origin (OriginLab), which required extensive manual user input and slowed down the process. The GUI was created to load the data and determine ϕ_{str} and V_0 more quickly. Figure 2.11 shows the GUI, labelled to highlight the role of different components.

2.2.1.4 Scattering correction

Photoelectrons generated in liquid water with UV light are affected by small energy losses (< 1 eV) due to inelastic scattering with water molecules. This causes the distribution of electrons that escape liquid jets to be distorted compared to that created upon photoionisation of the sample. Several groups have devised methods to retrieve the true photoelectron distribution from measured spectra.[51,77–80] The work in this thesis employs a revised version of a method developed in the group,[79] a detailed description of which can be found in Chapter 3. Figure 2.4f shows an example spectral retrieval.

2.2.1.5 Acquisition of time-resolved photoelectron spectra

Time-resolved experiments reported in this thesis employed a tunable pump beam generated by the OPA and a 266.7 nm probe beam generated by THG (Section 2.1) to study the ultrafast dynamics of $p\text{CE}^-$ in aqueous solution after electronic excitation. This section describes the experimental considerations associated with the acquisition of time-resolved photoelectron spectra.

In order to ensure that the point at which the probe beam intersects the liquid jet is independent of the position of the delay stage, the mirror before the retroreflector (M21 in Figure 2.1) is adjusted until moving the retroreflector to the start and end of the stage does not affect the position of the beam on a laser card placed in the beam path after the delay stage.

Spatial and temporal overlap of the pump and probe beams must be obtained to record time-resolved photoelectron spectra. Spatial overlap is easier

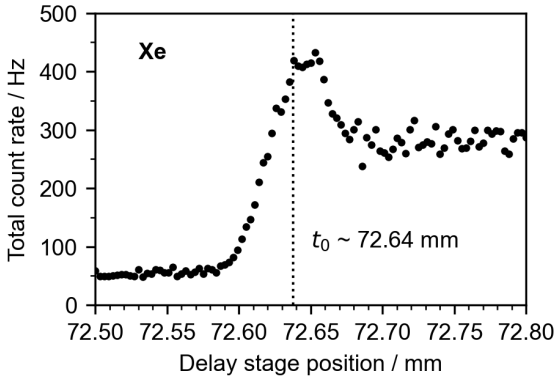

Figure 2.12: Total photoelectron count rate resulting from the photoionisation of Xe with a a 249.7 nm pump pulse and a 266.7 nm probe pulse, plotted as a function of delay stage position Before t_0, the signal consists solely of pump-only and probe-only contributions. After t_0, contribution from the excited state of Xenon, which is accessed by the pump pulse and ionised by the probe pulse is observed. At around t_0, a further contribution from non-resonant ionisation, involving the absorption of two 266.7 nm photons and one 249.7 nm photon is present.

to achieve with the liquid jet, since the jet occupies a smaller volume of the interaction region and maximising the counts of photoelectrons generated by each beam is generally sufficient to achieve partial spatial overlap. However, achieving temporal overlap can be more challenging as aqueous solutions can have short excited state lifetimes. Therefore, the delay stage position at which the pump and probe beams arrive at the sample at the same time (t_0) is determined in advance with Xe, using a pump wavelength of 249.7 nm, which is resonant with a long-lived excited state of Xe. To achieve this, photoelectron counts of Xe are maximised by aligning the pump and probe beams independently. The delay stage is then translated to long pump-probe delays and the pointing of the probe is adjusted to maximise the two-colour signal. An approximate value for t_0 is determined by moving the delay stage to shorter delays until the two-colour signal disappears (Figure 2.12). The kinetic trace in Figure 2.12 was fit using the sum of a Gaussian, representing the non-resonant contribution from two 266.7 nm photons and one 249.7 nm photon, and a Gaussian cumulative distribution function representing the population of the excited state of Xe after two-photon excitation with 249.7 nm and one-photon

ionisation with 266.7 nm. This value can be used as a starting point for determining t_0 with the liquid jet, as it can change by a few tenths of mm when changing the pump wavelength due to slightly different path lengths inside the OPA.

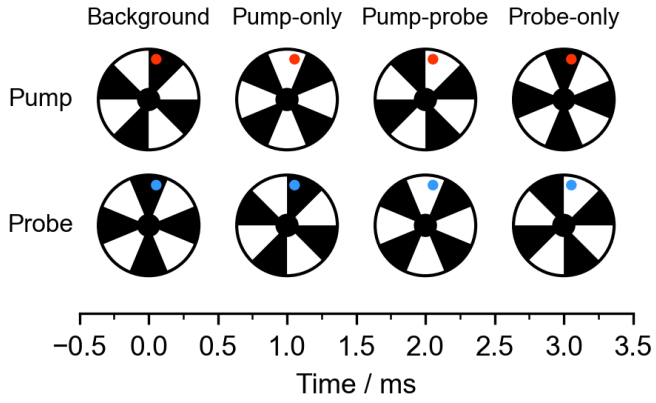

Figure 2.13: Diagram showing the chopper sequence used to separate pump–probe, pump-only, probe-only, and background signals. Red and blue dots indicate the positions of the pump and probe beams on the chopper wheel as a function of time, respectively.

Pump-probe measurements contain contributions from pump-probe, pump-only and probe-only signal. To accurately isolate the two-colour contribution, pump-only and probe-only signals are recorded separately and subtracted from the pump-probe signal during data processing. This is achieved by blocking the pump and probe beams in a controlled sequence using optical choppers, such that, over four consecutive shots, the interaction region receives (i) both pulses, (ii) only the pump, (iii) only the probe, and (iv) neither pulse (Figure 2.13). To ensure proper timing, the pump and probe beams are aligned onto the chopper blades at the same height and distance from the centre of the wheel. The choppers are then set with a relative phase of 90°. The phase with respect to the laser trigger is chosen by setting the revolution rate of the choppers to 1 kHz and adjusting the phase until both beams are blocked. The revolution rate of the choppers is then reduced to 250 Hz to achieve the configuration shown in Figure 2.13. A diagram showing the timing sequence

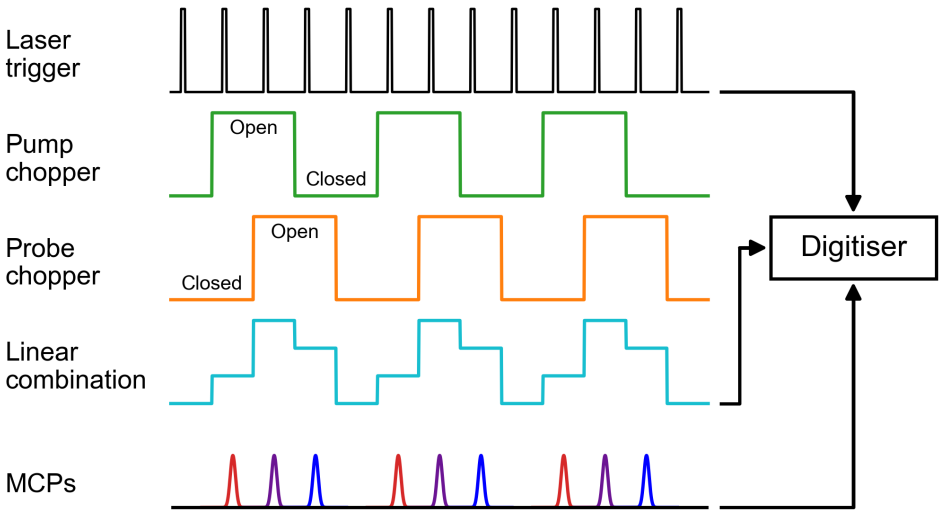

Figure 2.14: Diagram showing the timing sequence and signal gating used in the acquisition of time-resolved photoelectron spectra. The laser operates at a repetition rate of 1 kHz, and the choppers are set to 250 Hz, one quarter of the laser rate. Their phases are set to 90° of each other to ensure that pump-probe, pump-only, probe-only and background shots are recorded. The phase of the choppers relative to the laser trigger is adjusted to achieve the configuration shown in Figure 2.13. The signals from the choppers are combined to generate the trace labelled as "linear combination". The red, purple and blue peaks indicate the pump-only, pump-probe, and probe-only MCP signal. Their widths have been exaggerated for clarity. The digitiser combines the signals from the laser trigger, the choppers and the MCP detector to discriminate between pump-only, probe-only and pump-probe signal.

and signal gating is shown in Figure 2.14. Each chopper outputs a square-wave signal that indicates whether its respective beam is blocked or transmitted. These signals are merged to form a linear combination, which represents the beam configuration for each laser shot. The digitiser combines the signals from the laser trigger, the MCP detector, and the linear combination of the chopper signals to discriminate between the pump-only, probe-only, pump-probe and background signals. The desired two-colour spectra are obtained by subtracting the pump-only, probe-only and background spectra from the pump-probe spectra during data processing.

To determine the time resolution of the experiment, the cross-correlation

of the pump and probe beams is measured by recording time-resolved spectra of NO and Xe at delays around t_0. Efforts were made to record the cross-correlation with the pump wavelength employed in Chapter 5 (350 nm); however, one additional photon is required to ionise Xe and NO, and no two-colour signal could be observed. The cross-correlation was recorded with a 249.7 nm pump pulse and is expected to be nearly equal.

Figure 2.15 shows heatmaps of the time-resolved photoelectron spectra of Xe and NO, from which the pump-only, probe-only and background signals have been subtracted. Spectra were recorded with pump-probe delay steps of 20 fs for 10 s at each delay (2.5 s per channel). The photoelectron signal integrated over the non-resonant two-colour signals as a function of pump-probe delay was fit with Gaussians and values for the cross-correlation of 319 and 310 fs were obtained for NO and Xe, respectively.

When recording liquid-jet TRPES, t_0 is determined by measuring spectra at a series of time delays around the value of t_0 determined with Xe. The rising edge of the total counts is fit with a Gaussian or an exponential decay function convoluted with a Gaussian, where the Gaussian FWHM corresponds to the cross-correlation. The choice of pump-probe delays depends on the expected excited state population decay of the species of interest. A few negative delays are typically included to ensure no signal arises from probe-pump dynamics and to observe the rise in signal around t_0. Pump-probe delays are generally selected using a weighed exponential function of the form $t = T(e^{cx}-1)/(e^{c}-1)$, where t is a set of pump-probe delays, x is a set of evenly spaced values between 0 and 1, T is the total delay range and c is a weighting factor. Larger values of c bias the distribution toward finer time steps near t_0, allowing for higher temporal resolution during the early stages of the excited-state evolution.

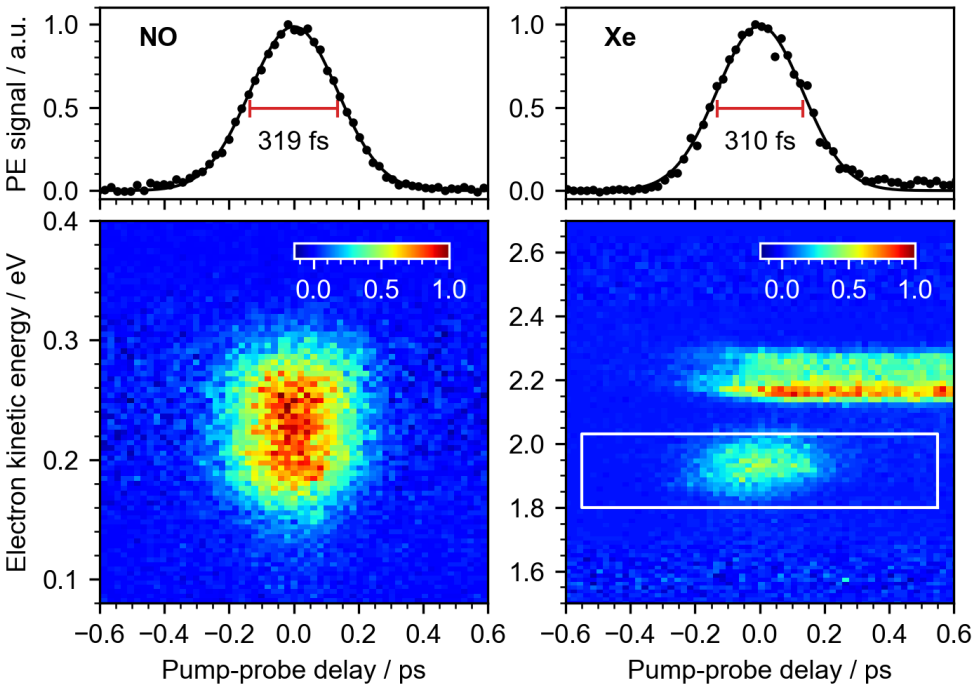

Figure 2.15: Cross-correlation determined from the time-resolved photoelectron spectra of NO and Xe. The heatmaps show the normalised photoelectron spectra of NO and Xe, from which the pump-only, probe-only and background signals have been subtracted. The NO signal was integrated between 0 and 0.4 eV, and the Xe signal was integrated between 1.8 and 2.0 eV (white box). The integrated signals were plotted as a function of pump-probe delay and fit with Gaussians, yielding cross-correlations of 319 and 310 fs.

2.2.2 Operation of the UCL liquid-microjet spectrometer

This section outlines the steps required to operate the liquid-microjet photoelectron spectrometer at UCL. When not in use, the spectrometer is typically under vacuum without the liquid jet assembly. In order to vent the instrument, the gate valves connecting the interaction chamber, the TOF region and the detector region to their respective turbomolecular pumps are closed. It is important to note that the pressure in the interaction chamber must always be larger or equal to the pressure in the TOF region to prevent damage to the skimmer, so the interaction chamber gate valve must be closed first. The venting needle valve of the interaction chamber is opened slightly until the

pressure in the TOF and detector regions is $\sim 1 \times 10^{-1}$ mbar. Then, the backing lines of the TOF region turbo pumps are closed and the roughing line of the TOF region is opened. This is done to aid the pumping down of the TOF region and minimise the pressures the MCP detector is exposed to. The interaction chamber venting valve is then opened fully and the interaction chamber is allowed to reach atmospheric pressure. The liquid jet assembly is placed into the interaction chamber. A CMOS camera (C1 in Figure 2.2) is used to ensure the liquid jet nozzle is placed in between the magnet and the skimmer, $\sim$1 mm above the magnet-skimmer axis. If the liquid catcher is used, careful alignment of the jet and the catcher is required to avoid freezing of the sample under vacuum. When using the cold trap, this requirement is less stringent as the cold trap opening has a diameter of $\sim$2.4 cm. The HPLC pump is turned on to allow the liquid to flow through the nozzle and the cold trap is removed to ensure that the liquid stream is centred on the entrance of the cold trap. The cold trap is then replaced and a dewar filled with liquid nitrogen placed around it. The chamber is now ready to be pumped down. The backing line of the interaction chamber turbo (C1 in Figure 2.2) is closed and the roughing line of the interaction chamber is opened. Once the pressures in the TOF and detector region drop below 10^{-1} mbar, the TOF roughing line is closed, the TOF backing lines are opened and the gate valves of the detector and TOF region turbos are opened (T2, T3 and T4 in Figure 2.2). This causes the pressures in the TOF and detector regions to drop to 10^{-5}-10^{-6} mbar. The interaction chamber cold trap is then filled with liquid nitrogen (10 in Figure 2.2). The roughing line of the interaction chamber is closed when the pressure of the interaction chamber pressure reaches 10^{-1}-10^{-2} mbar. Once the cold trap is completely filled with liquid nitrogen, the interaction chamber typically reaches pressures between 10^{-3} and 10^{-4} mbar. The backing line of the interaction chamber turbo is opened and its gate valve is opened (T1 in Figure 2.2). Pressures between 7×10^{-5} and 1.0×10^{-4} mbar are achieved in the interaction region, and pressures between 5×10^{-7} and 9×10^{-7} mbar in

the TOF and detector regions.

Next, the liquid jet is aligned with the entrance of the skimmer (3 in Figure 2.2) by maximising the pressure in the TOF and detector regions while translating in the direction perpendicular to the skimmer-magnet axis and the liquid jet flow, heron referred to as the y-axis. A 249.7 nm laser pulse is aligned onto the jet, by checking the diffraction pattern generated by the overlap of the laser and the liquid jet, and by maximising photoelectron counts. Typically, the position of the focus of 249.7 nm pulses along the y-axis is optimised for maximum Xe counts using the lens placed before the entrance to the chamber (Figure 2.1). The y position of the jet is further optimised by maximising photoelectron counts. Thereafter, ϕ_{str} and the vacuum level offset can be measured by recording photoelectron spectra of Xe while moving the jet away from the interaction region. Typically, pressures between 1×10^{-4} and 2×10^{-4} are employed when recording Xe spectra. This procedure is repeated until a sufficiently low ϕ_{str} (≤ 0.08 eV) is achieved by adjusting the flow rate of the HPLC pump. This measurement is also repeated at the end of a set of LJ-PES experiments.

One-colour experiments are performed by focusing a pulse of a specific wavelength into the jet. Photoelectron count rates $\lesssim 1$ kHz are typically achieved by attenuating the laser with neutral density filters to avoid saturation of the detector. Typical integration times are between 5 and 20 minutes depending on the count rate.

When performing time-resolved experiments, the probe pulse is aligned onto the delay stage by ensuring the pointing of the laser after the stage is independent of the stage position. The pump and probe pulses are then aligned onto the choppers, as described in Section 2.2.1.5. It must be noted that the foci of the pump and probe beams differ by a few mm, due to the difference in wavelength and slightly different divergence angles. Therefore, the focusing lens (Figure 2.1) is placed such that the liquid jet is between the two foci. The pump and probe pulses are then aligned onto the liquid jet. Checking

for the diffraction pattern created by the overlap of each beam and the jet and maximising photoelectron counts is generally sufficient to achieve some spatial overlap between the two beams, which allows for the determination of t_0. The delay stage position corresponding to maximum temporal overlap is determined by scanning over pump-probe delays close to the value of t_0 obtained in advance with Xe. Thereafter, spatial overlap is further optimised by maximising the pump-probe signal at t_0. Chopper alignment may be further verified by ensuring that the count rate in the pump-only channel matches that in the pump–probe channel when the probe beam is blocked, and vice versa when the pump beam is blocked. No signal should be present in the background channel. Finally, the pump and probe beam powers are carefully minimised, while ensuring that the pump–probe signal remains sufficiently enhanced for reliable detection and improved signal-to-noise ratio. Pump-only, probe-only, pump-probe and background spectra are then recorded at a series of delay stage positions to obtain time-resolved photoelectron spectra of the aqueous sample of interest.

2.3 Summary

This chapter has described the experimental apparatus and procedures employed to record the UV PES and TRPES spectra of *p*CE$^-$ in aqueous solution recorded at UCL presented in Chapters 4 and 5. Section 2.1 outlined the femtosecond laser system employed in the UCL experiments. The UCL magnetic-bottle liquid-jet photoelectron spectrometer was described in Section 2.2, and experimental considerations and data processing procedures associated with recording UV LJ-PES data were described in Section 2.2.1. In this section, the conversion from time of flight to eKE, the characterisation of the energy-dependent collection efficiency of the spectrometer and the importance of achieving a flat potential in the interaction region were discussed; the experimental considerations and procedures employed in the measurement of time-resolved photoelectron spectra were also outlined. Finally, the operating

procedure of the UCL photoelectron spectrometer was described in Section 2.2.2.

Chapter 3

Retrieval of genuine ultraviolet photoelectron spectra

Ultraviolet liquid-microjet photoelectron spectroscopy (UV LJ-PES) is a powerful technique for the determination of electron binding energies of molecules in aqueous solution and for exploring their photochemical dynamics. However, our poor understanding of inelastic scattering of low energy electrons (< 10 eV) in water has hindered the determination of accurate vertical ionisation energies and although several algorithms have been implemented to retrieve genuine binding energies from experimental spectra, a consensus on the parameters employed is yet to be reached. The work presented in this chapter builds on previous work in our group by investigating the effect of these parameters on the retrieval of true photoelectron spectra of water, phenol and phenolate. The results of this chapter show that the scattering cross sections obtained by extrapolating the cross sections in amorphous ice to zero electron kinetic energy describe the distortion observed in UV LJ-PES spectra accurately, that the description of the transmission of electrons at the liquid-vacuum interface is crucial to infer a value for the electron affinity of water at the surface, and emphasises the importance of considering concentration depth profiles when retrieving true photoelectron spectra of surface-active solutes. This work highlights the potential for accurate ultraviolet photoelectron spectroscopy of aqueous solutions of organic molecules.

3.1 Background

Photoelectrons generated in liquid microjets are subject to scattering with water molecules.[71,87] This can result in electrons losing energy as they travel inside the liquid, thus losing valuable information about the electronic states they originate from. Electrons can lose energy via different processes including excitation of resonances of water and impact ionisation, and the cross sections associated with these phenomena in liquid water have been subject to debate. Nonetheless, two general scenarios can be considered. On one hand, photoelectrons generated with X-ray and EUV light typically have high enough energy to access scattering channels that involve large energy losses (e.g., electronic excitations or impact ionisation), which dominate at electron energies greater than $\sim$ 10 eV.[71] A direct consequence is that the distribution of inelastically scattered electrons is completely separated from the distribution of the elastically scattered or unscattered electrons, which ensures that accurate binding energies can be extracted. On the other hand, photoelectrons generated with UV or low-energy EUV ($h\nu \lesssim 20$ eV) light can only access translational, rotational and vibrational modes of water which involve energy losses smaller than 1 eV.[51,77,79,80] In this case, spectra are characterised by distorted distributions.

Despite their ability to yield accurate binding energies, a limitation of X-ray and EUV photoelectron spectroscopy is that high solute concentrations must generally be used to obtain a sufficient signal-to-noise ratio against the water background (55.5 M). UV LJ-PES can overcome this limitation by exploiting multiphoton ionisation, which typically provides enough energy to ionise solute molecules while remaining below the ionisation threshold of water, thus making it a powerful technique for the study of weakly soluble organic molecules ($\lesssim$ 1 mM).[10,65] Furthermore, femtosecond time-resolved photoelectron spectroscopy (TRPES) employing a UV pump pulse and a UV or EUV probe pulse, which has proved invaluable for tracking ultrafast electronic dynamics in the gas phase and on surfaces, has also been extended to liquids by several groups.[56,57,67,88–90] TRPES with EUV probe pulses has the advantage

that the observation window is broad enough to track electronic relaxation from the excited-state potential energy surface back to the ground electronic state, but TRPES of sparingly soluble organic molecules benefits from the increased sensitivity that is best achieved using UV probe pulses. Therefore, UV LJ-PES has the potential to transform our understanding of the electronic structure and relaxation dynamics of photoexcited organic molecules in aqueous solution; however, scattering of the emitted electrons within liquid water is a major challenge that must be overcome for accurate interpretation of these photoelectron spectra.

Recent work has devised retrieval methods to obtain accurate eBEs from experimental UV photoelectron spectra.[51,77–80] The first method, developed by Signorell and co-workers,[51] is based on a Monte-Carlo electron transport model to simulate the scattering of low-energy electrons in water employing a set of scattering cross sections derived from amorphous ice and photoelectron spectra of water droplets.[50] Subsequently, Wörner and co-workers simulated spectra with eKEs between 0 and 50 eV and investigated the effect of different simulation parameters, focusing on photoelectrons generated with EUV pulses.[80] A different approach involving a spectral inversion method based on empirical results was developed by Suzuki and co-workers.[77,78] They measured photoelectron spectra of the solvated electron employing EUV light and a range of UV wavelengths. Each measured UV spectrum, $g_k(E)$, was mapped to an initial Gaussian distribution, $G_k(E)$, created by shifting the EUV spectrum by the difference between the UV and the EUV photon energies. To obtain true photoelectron spectra, a linear combination of $g_k(E)$ distributions was fit to experimental data, $I_{\text{meas}} = \sum_i c_i g_k(E)$, and the expansion coefficients, c_i, were used to expand the $G_k(E)$ distributions to obtain true photoelectron spectra, $I_{\text{true}} = \sum_i c_i G_k(E)$. Subsequent work in our group combined the spectral inversion approach with Monte Carlo simulations to determine the linear transformations between genuine and measured distributions, and introduced the ability to treat non-uniform concentration depth profiles.[79] In this ap-

proach, each $G_k(E)$ corresponds to a single photoionisation process and the transformation from $G_k(E)$ to $g_k(E)$ is obtained from Monte Carlo simulations of electrons in water.

There has been some discussion in the literature over the parameters employed in Monte-Carlo simulations and spectral retrieval methods. Signorell and co-workers derived a set of scattering cross sections by using the scattering cross sections measured in amorphous ice as the initial guess to fit to water droplet photoelectron imaging data,[50,51] which were also employed in the work of our group.[79] In a later study, Signorell and co-workers refined the set of cross sections they employed by refitting them to the droplet data using additional sampling points,[49] which reduced the value of the cross sections for eKEs below 1 eV. Wörner and co-workers employed a dielectric model of water to determine singly-differential inelastic cross sections and scaled the total integral inelastic cross sections to correspond to a constant 3 nm inelastic mean free path.[80]

Another important aspect is the treatment of the transmission of electrons at the surface of liquid jets. Signorell's group determined the escape for each electron individually,[51] while Wörner's group and our group applied a transmission function *a posteriori*, assuming a uniform distribution of escape angles.[79,80] Suzuki and co-workers fit this transmission function to the lower energy side of photoelectron spectra and obtained a value of 0.2 eV for the escape threshold.[77] This value contrasts with those employed by Signorell's group and our group (1.0 eV),[51,79] Wörner's group (0.8 eV)[80] and a value determined computationally (0.8 eV),[82] but is consistent with the value suggested by Bartels (0.1 eV).[81]

Inspired by this general lack of consensus on the parameters employed in UV-PES spectral retrieval methods, a systematic study of the impact of different parameters on the retrieval of UV photoelectron spectra was undertaken. The effect of several sets of cross sections, the way the transmission at the liquid-vacuum interface is determined and the value of the escape threshold on

the photoelectron spectrum of water were tested. The depth profiles employed to describe the photoelectron spectra of aqueous phenol and phenolate, which are being used by several groups to benchmark accurate procedures, were also revised.

3.2 Computational Details

3.2.1 Monte Carlo Simulations and Spectral Retrieval

The code employed in this Chapter, LJscatter, is an improved version of the code described in Ref. 79 (Scholz, M. S.; Fortune, W. G.; Tau, O.; Fielding, H. H. *JPCL* **2022**, *13*, 6889–6895), incorporating bug fixes and an enhanced physical description of the simulation. This refined version is freely available online.[91]

The Monte Carlo simulation describes the transport of electrons inside the liquid jet and their transmission at the liquid-vacuum interface. Several random walks are performed at each starting depth d, and initial kinetic energy E_i, which is expressed relative to the vacuum level around the liquid jet. In this work, 10^4 trajectories were run in a liquid jet with a 20 µm diameter at depths between 0.1 and 50 nm sampled in 0.1 nm steps and with starting energies between 0.01 and 5 eV sampled in 0.01 eV steps. Electrons are initialised in a cylinder with infinite height at each depth below the surface only on the x axis as the cross section of the jet has circular symmetry, which is accounted for at a later stage, and the model assumes that all electrons that escape are detected despite their z position.

In each step, the electron travels in a random isotropic direction, covering a distance sampled from an exponential distribution with the mean free path (MFP) of the electron as its mean. The MFP is determined using a set of integral cross sections as follows

$$\mathrm{MFP}(E) = \frac{1}{\rho_n \sigma_\mathrm{tot}(E)}, \tag{3.1}$$

where ρ_n is the number density of water and $\sigma_\mathrm{tot}(E)$ is the sum of all the

integral scattering cross sections at a specific eKE. If at the end of a step the electron is inside the jet, an energy-loss channel describing a translational, rotational or vibrational mode of water, is selected based on the relative intensity of the corresponding cross section and the electron loses energy sampled from a normal distribution. The scattering cross sections and energy-loss parameters employed in this work are described and discussed in detail in Section 3.2.3. If at the end of a step the position of the electron places it outside the jet, it must be determined whether the electron has enough energy to escape. Classically, the component of its velocity perpendicular to the surface must correspond to a kinetic energy higher than the electron affinity of water at the surface (E_0), i.e., the difference between the conduction band minimum at the liquid-vacuum interface and the vacuum level. Two approaches have been employed to describe transmission at the surface. The first approach assumes that the distribution of the velocity vectors of electrons hitting the surface is isotropic and uses the transmission probability

$$T(E) = 1 - \sqrt{\frac{E_0}{E + E_0}} \tag{3.2}$$

to filter electrons at the end of their trajectory (method **A**).[45,78] An alternative approach is to calculate the kinetic energy component perpendicular to the surface for every electron as it hits the surface and to allow it to escape only if this value is greater than E_0 (method **B**).[51] Trajectories are terminated when electrons successfully escape the jet or their kinetic energy becomes negative.

The final kinetic energies E_f are binned in 0.01 eV steps to form a series of distributions $S(E_\mathrm{f}; E_\mathrm{i}, d)$, which are scaled by the radius of the jet to account for greater volumes at lower depths. An example is shown in Figure 3.1a. The $S(E_\mathrm{f}; E_\mathrm{i}, d)$ distributions can be scaled by any arbitrary concentration profile and integrated over starting depth d, to give solute-specific basis sets composed of $S(E_\mathrm{f}; E_\mathrm{i})$ functions. A set employing a uniform concentration profile is shown in Figure 3.1b. The transformation from $G_k(E)$ to $g_k(E)$ is obtained by scaling the basis set by $G_k(E)$ and integrating over E_i (Figure

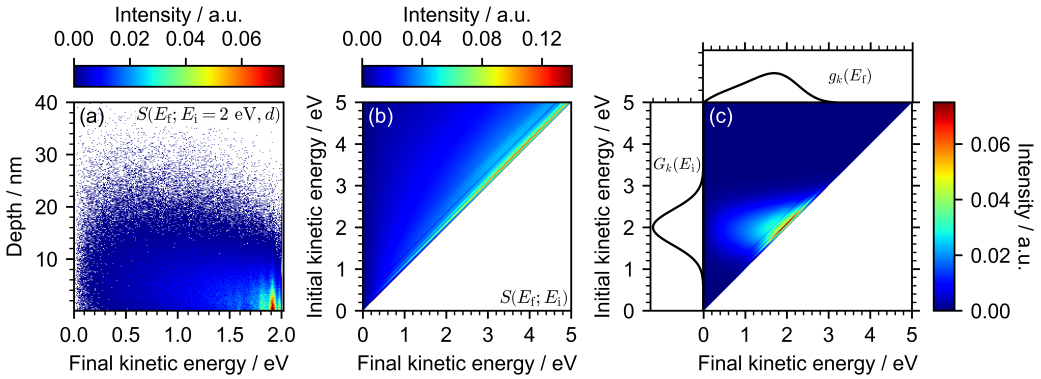

Figure 3.1: (a) Example normalised $S(E_f; E_i = 2\ \mathrm{eV}, d)$ distributions. Points with intensities between 0.075 and 1 only appear at 2 eV and represent electrons that have only been elastically scattered; this whole range was set to dark red to highlight the variation in the distribution of inelastically scattered electrons. Furthermore, points with 0 intensity were set to white. (b) Basis set composed of a series of $S(E_f; E_i)$ distributions representing a uniform concentration profile. Points with intensities between 0.14 and 1 only appear on the diagonal and represent electrons that have only been elastically scattered; this whole range was set to dark red to highlight the variation in the distributions of inelastically scattered electrons. (c) Transformation of a true Gaussian into a distorted Gaussian: $G_k(E) \Longrightarrow g_k(E)$. The basis set in (b) was scaled by $G_k(E)$ and integrated across E_i to generate $g_k(E)$. In this simulation we employed starting energies between 0.01 eV and 5 eV sampled in 0.01 eV steps, depths between 0.1 and 50 nm sampled in 0.1 nm steps, 10 000 electrons at each depth, an escape threshold of 1.0 eV, method **B** to treat the transmission at the surface and cross section set **III**. Reproduced from Ref. 92. Further permissions related to the material excerpted should be directed to the American Chemical Society.

3.1c). Measured photoelectron spectra are then interpolated onto a regular x-grid with 0.01 eV steps and fit with a linear combination of distorted Gaussian to obtain the corresponding genuine photoelectron distribution (Figure 3.1c).

3.2.2 Code Refinement

In the process of testing the various parameters, some small bugs in the earlier code were corrected. Interestingly, the combined effect of these bugs cancelled each other out and resulted in an accurate retrieval of the UV liquid-jet photoelectron spectrum of water.

The code employed cross sections digitised from Ref. 51. Curiously, the

cross sections had been plotted only above 0.1 eV but it had been assumed they were plotted from 0 eV. This was corrected although it was found to have a negligible impact on the final results. While investigating the effect of different cross section sets, it was found that the way the Julia language handles dictionaries led to energy-loss parameters being assigned to incorrect scattering cross sections. This had a minor effect on the final results and was corrected. Furthermore, a factor of 4π was present in the calculation for the MFP. This may have been introduced to represent a full solid angle, but increased the true MFP by an order of magnitude. As this factor was not required for calculating the MFP,[93] it was removed. Finally, each $S(E_\mathrm{f}; E_\mathrm{i})$ distribution was normalised by its area in an attempt to create a probability distribution for electrons with a specific initial kinetic energy. However, this fails to take into account the fact that electrons with different E_i do not have the same probability to escape the jet. This was corrected so that the relative intensity of the $S(E_\mathrm{f}; E_\mathrm{i})$ distributions is retained.

Having made the last correction it became apparent that the scattering cross sections reported in Ref. 51 needed some refinement for the lowest energy electrons (< 1.7 eV), which is described in detail in the next section.

3.2.3 Scattering Cross Sections and Energy-loss Parameters

The Monte Carlo simulation requires energy-loss parameters and cross sections in order to model the magnitude and likelihood of the energy loss that electrons experience in liquid microjets. The effect of four different sets of cross sections was tested (Figure 3.2). Set **I** employed cross sections digitised from the first spectral retrieval model reported by Signorell's group, based on amorphous ice cross sections and cross sections obtained by fitting to photoelectron spectra of water aerosol droplets.[50,51] It should be noted that the contribution from the 'other' scattering channel is missing from set **I** below 3 eV because the cross sections in Ref. 51 were only presented above 2×10^{-19} cm^2; this does not impact the retrieval, as discussed later in this section. This set allows for

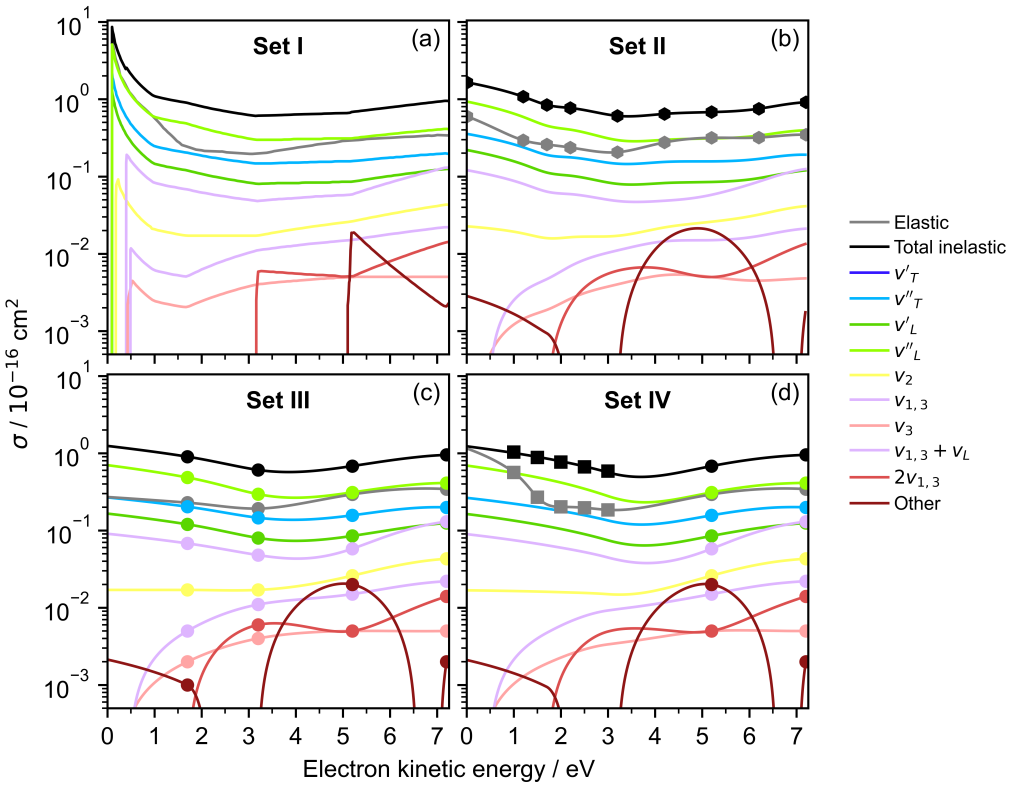

Figure 3.2: The four sets of cross sections employed in the scattering simulations, for specified energy loss channels as a function of electron kinetic energy. (a) Set **I**: cross sections digitised from Ref. 51 (b) Set **II**: cross sections derived from the refined total cross sections in Ref. 49 (hexagons). (c) Set **III**: cross sections interpolated and extrapolated using the cross sections determined in amorphous ice experiments (circles).[45] (d) Set **IV**: cross sections determined using photoelectron spectroscopy experiments of water nanodroplets (squares)[50] and amorphous ice experiments (circles).[45] Reproduced from Ref. 92. Further permissions related to the material excerpted should be directed to the American Chemical Society.

comparison with the original spectral retrieval model.[79] Set **II** employed total inelastic and elastic cross sections refined with additional sampling points, as reported by Signorell.[49] These were interpolated with a cubic spline, and the contributions of individual inelastic cross sections relative to the total inelastic cross section were determined by scaling the amorphous ice cross sections.[45] Set **III** employed the cross sections for amorphous ice[45]. These were extrapolated linearly to 0 eV below the lowest reported value of 1.7 eV, and interpolated with a cubic spline above 1.7 eV. Set **IV** employed total inelastic and elastic cross

sections reported by Signorell's group and derived by fitting photoelectron spectra of water droplets,[50] together with the cross sections for amorphous ice above 5.2 eV.[45] A straight line was fit through the total inelastic cross sections from 3 eV to 1 eV and extrapolated to 0 eV; the cross sections were interpolated with a cubic spline above 3 eV. The elastic cross sections were linearly extrapolated below 1 eV, and interpolated with a cubic spline above 1 eV. The contributions of individual inelastic cross sections relative to the total inelastic cross section were determined by scaling the amorphous ice cross sections.[45]

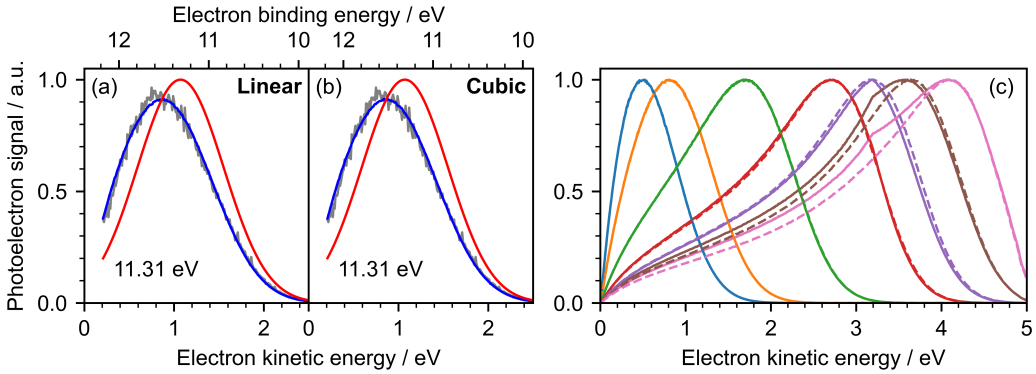

Figure 3.3: (a, b) Effect of interpolating cross section set **III** (a) linearly or (b) with a cubic spline on the retrieval of the spectrum of water. Gray lines are the experimental data, blue lines are fits to the data, red lines are retrieved spectra, and numbers in each panel are the retrieved eBEs. (c) Effect of interpolating cross section set **III** linearly (solid lines) or with a cubic spline (dashed lines) on the distortion of Gaussians centred at 0.5, 1, 2, 3, 3.5, 4 and 4.5 eV and a FWHM of 1 eV. All simulations were run using method **B** and an escape threshold of 1.0 eV. Reproduced from Ref. 92 with experimental spectra adapted from Ref. 79. Further permissions related to the material excerpted should be directed to the American Chemical Society.

A cubic spline was employed to interpolate the cross sections used in this work rather than linear interpolation to avoid the introduction of artificially sharp features in the distorted distributions (Figure 3.3c). The retrieval of the spectra employed in this study is unaffected by the choice of interpolation, as it only has an effect at central eKEs $\gtrsim$ 3 eV (Figure 3.3a, b).

The energy-loss parameters associated with each cross section were ob-

Table 3.1: Mean energy and FWHM of the energy-loss channels employed in this study, taken from electron-scattering measurements in amorphous ice.[45] v'_T and v''_T are translational modes, v'_L and v''_L are librational modes, v_2 is the bending mode, $v_{1,3}$ are the stretching modes, v_3 is the asymmetrical stretching mode, $v_{1,3}+v_L$ is the stretching-librational combination mode and $2(v_{1,3})$ is the overtone of the stretching modes of water. 'Other' includes higher energy channels and 'elastic' represents elastic scattering events, which do not involve any energy loss.

Channel	Mean / meV	FWHM / meV
v'_T	10	1
v''_T	25	24
v'_L	61	30
v''_L	92	40
v_2	204	16
$v_{1,3}$	471	50
v_3	460	5
$v_{1,3} + v_L$	500	40
$2(v_{1,3})$	835	75
other[a]	–	–
elastic	0	0

[a]These trajectories are terminated.

tained from the results of electron-scattering experiments of amorphous ice reported by Michaud et al.,[45] and are shown in Table 3.1. The energy-loss channels comprise intramolecular vibrational modes of water, as well as intermolecular modes (librations and translations) arising from the condensed nature of amorphous ice. In their model, Michaud et al. also included a channel 'other', which encompasses electron attachment, electronic excitation and ionization processes.[45] The energy loss of these processes was not quantified by the authors as they focused on energy losses below 1 eV.[45] For electrons within the eKE range employed in the work presented in this Chapter (0-5 eV), they suggested that the processes included in 'other' were dominated by electron attachment, followed by either dissociation or autodetachment from high vibrational levels of the electronic ground state of the water anion. The latter produces electrons that could be measured in UV LJ-PES experiment. Luckhaus et al. also employed these cross sections in their model and quoted energy losses > 5 eV for this channel.[51] Subsequently, our group employed a mean

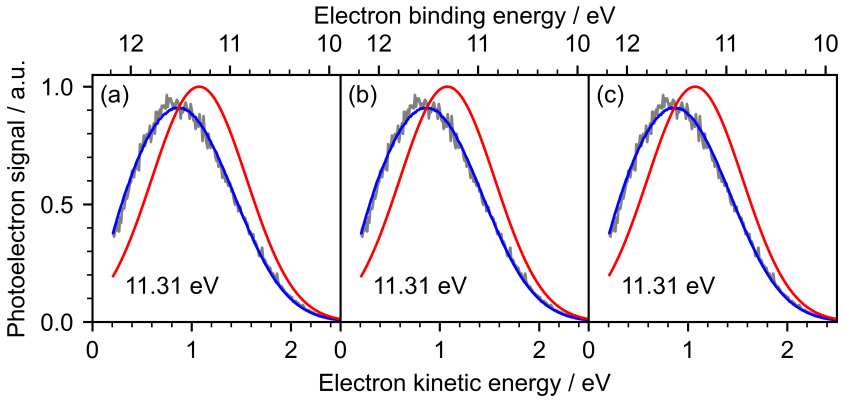

Figure 3.4: Retrieval of the 200.2 nm non-resonant two-photon photoelectron spectrum of water employing cross section set **III** and (a) setting the 'other' cross sections to 0, (b) setting the 'other' cross sections to 0 and rescaling the rest of the inelastic cross sections to yield the same total inelastic cross sections as set **III**, and (c) setting the 'other' energy loss to 1.5 eV with a FWHM of 0.25 eV. Gray lines are the experimental data, blue lines are fits to the data, red lines are retrieved spectra, and numbers in eV are the ionisation energies of water determined using each method. All simulations were run using method **B** and an escape threshold of 1.0 eV. Reproduced from Ref. 92 with experimental spectra adapted from Ref. 79. Further permissions related to the material excerpted should be directed to the American Chemical Society.

energy loss of 5 eV and a FWHM of 5 eV.[79] As Michaud et al. did not quote the energy loss or the relative likelihood of electron attachment and its cross sections are relatively low, trajectories that accessed 'other' were terminated in the simulations of this work, effectively only modelling electron capture. To test whether this assumption is justified, simulations employing cross section set **III** and (a) setting the 'other' cross sections to 0, (b) setting the 'other' cross sections to 0 and rescaling the rest of the inelastic cross sections to yield the same total inelastic cross sections as set **III**, and (c) setting the 'other' energy loss to 1.5 eV with a FWHM of 0.25 eV were performed. The results of these simulations are presented in Figure 3.4 and demonstrate that the 'other' channel does not have any significant effect on the retrieval of the 200.2 nm non-resonant two-photon photoelectron spectrum of water.

Another important quantity is the effective attenuation length as it provides a measure of the depth sensitivity of LJ-PES. It is defined as the distance

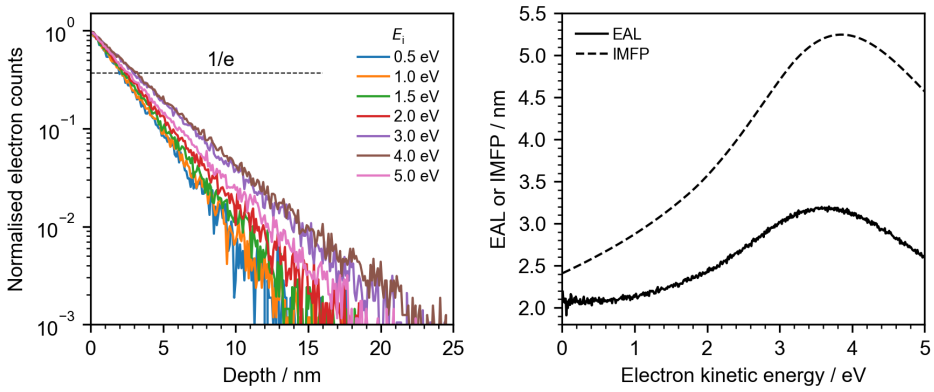

Figure 3.5: Left: Distribution of electrons that maintain their original eKE and successfully escape the jet as a function of depth for different initial kinetic energies. Right: EALs obtained from fitting an exponential decay to the data shown in the left panel. The IMFP obtained from the cross sections is also shown. This simulation was run using the refined code employing method **B** with an escape threshold of 1.0 eV and cross section set **III**.

at which the fraction of electrons that retain their initial eKE is $1/e$. Simulations run with the refined code using cross section set **III** and method **B** yielded effective attenuation lengths (EALs) between 2.1 and 3.2 nm (Figure 3.5). These values are consistent with EALs measured in liquid water at low eKEs: Suzuki et al. reported an EAL of 3.02 ± 0.46 nm at an eKE of 5 eV, although they noted that the instability of the background of secondary electrons made EALs less accurate at eKEs less than 10 eV.[48]

3.2.4 Escape of Electrons at the Liquid-Vacuum Interface

The effects of the approaches employed to determine the transmission of electrons at the liquid-vacuum interface was investigated. As previous studies have employed two approaches to describe transmission at the surface of liquid-jets, the effect of filtering electrons at the end of their trajectory with the transmission probability $T(E) = 1 - \sqrt{E_0/(E + E_0)}$ (Equation 3.2, method **A**) or determining the transmission of electrons by calculating the eKE component normal to the surface (method **B**) was explored. Additionally, the effect of the value of the escape threshold E_0 on the retrieval of the 200.2 nm spectrum of

water was investigated. Results are shown in Section 3.3.2.

3.2.5 Molecular Dynamics Simulations and Concentration Depth Profiles

Following the approach developed by Scholz et al.,[79] molecular dynamics (MD) simulations of phenol and phenolate in aqueous solution were performed using the OpenMM package (version 7.7.0)[94] to inform the choice of concentration profiles in this work. The initial coordinates of the solute were optimised using the Automated Topology Builder and Repository[95,96] at the B3LYP/6-31G* level of theory. The SMIRNOFF force field (version 0.11.4)[97] was employed to model the solute surrounded by a Transferable Intermolecular Potential with 3 Points (TIP3P) water environment.[98] One molecule of phenol or sodium phenolate was placed in a 5×5×9 nm box and surrounded with water molecules. The box was then expanded to 5×5×18 nm to simulate the liquid-vacuum interface and periodic boundary conditions were applied. This setup results in an infinite series of slabs with a thickness of 9 nm, separated by 9 nm of vacuum. MD simulations were run using Langevin dynamics with LFMiddle discretisation[99] with a heat bath set at 300 K, a 2 fs time step and a friction coefficient of 1 ps^{-1}. Long-range electrostatic interactions were described by the Particle Mesh Ewald (PME) with a 1 nm cutoff. A local energy minimization was performed and the velocities of all the atoms were set to random values chosen from the Boltzmann distribution at 300 K, before the system was allowed to equilibrate for 2 ns. Simulations were run for 120 ns, recording the position of all atoms every 4 ps. Six simulations per solute were carried out. The centre of mass of the solute was used to track its position along the axis perpendicular to the surface.

3.2.6 Uncertainties in Spectral Retrieval

The accuracy of the spectral retrieval depends on the uncertainties associated with the experimental data (± 0.07)[79] and the uncertainties in the model. Similarly to the previous version of the code,[79] the energy-loss parameters ob-

tained from electron-scattering experiments in amorphous ice are assumed to have an accuracy of at least 0.01 eV. The uncertainty in the magnitude of the cross sections is expected to yield an uncertainty in the retrieved peak maxima of less than 0.03 eV, based on the results of the sensitivity analysis shown in Section 3.3.3. The overall uncertainty associated with rounding, the number of electrons, the depth step size, the maximum probed depth, the radius of the jet employed in the simulations is expected to be less than 0.02 eV. Therefore, the errors associated with the retrieval of UV LJ-PES spectra are expected to be ±0.04 eV and the retrieved VIE and VDEs of water, phenol and phenolate are quoted to an accuracy of ±0.09 eV.

3.3 Results and Discussion

3.3.1 Scattering Cross Sections

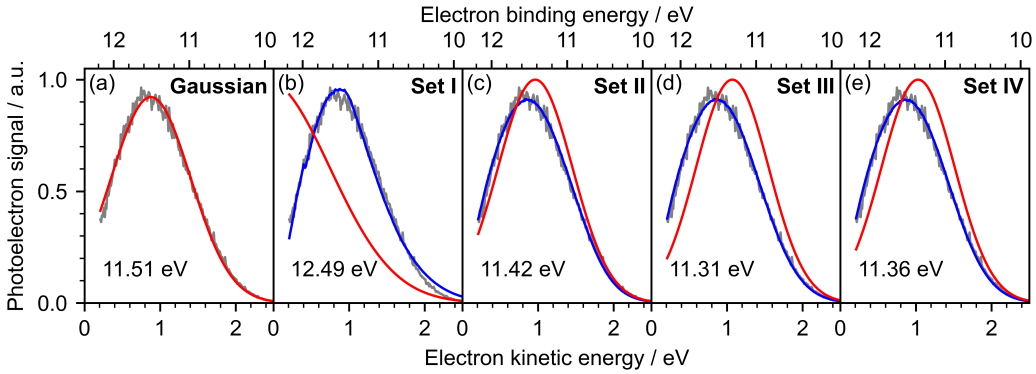

Figure 3.6: Photoelectron spectrum of water recorded at 200.2 nm as a function of electron kinetic energy interpolated in 0.01 eV steps (gray). The spectrum was fitted with a Gaussian (a), or fitted using the spectral retrieval code using cross section sets **I-IV** (b-e). Blue lines are fits to the data, red lines are retrieved spectra, and numbers in eV are the ionisation energies of water determined for each method. All spectral retrievals employed method **B** with an escape threshold of 1.0 eV. Reproduced from Ref. 92 with experimental spectra adapted from Ref. 79. Further permissions related to the material excerpted should be directed to the American Chemical Society.

Figure 3.6 shows the photoelectron spectrum of water following non-resonant two-photon ionisation with a 200.2 nm pulse[79] fit with (a) a Gaussian, or (b-e) using the spectra retrieval code and different sets of scattering cross

Table 3.2: Central eKEs, eBEs and FWHMs of the 200.2 nm spectrum of water[79] obtained by fitting a Gaussian, or with the spectral retrieval code employing cross section sets **I**–**IV**.

Method	eKE / eV	eBE / eV	FWHM / eV
Gaussian	0.88 ± 0.07	11.51 ± 0.07	1.21 ± 0.04
Set **I**	−0.11 ± 0.09	12.49 ± 0.09	2.00 ± 0.09
Set **II**	0.96 ± 0.09	11.43 ± 0.09	1.17 ± 0.07
Set **III**	1.08 ± 0.09	11.31 ± 0.09	1.13 ± 0.07
Set **IV**	1.02 ± 0.09	11.36 ± 0.09	1.14 ± 0.07

sections. Simulations were run using an escape threshold of 1.0 eV and method **B** was employed to determine the transmission of electrons at the surface. The results of the fits are summarised in Table 3.2. Fitting the spectrum with a Gaussian neglects inelastic scattering and incorrectly overestimates the VIE of water as 11.51 ± 0.07 eV, which is 0.2 eV higher than the accurate values determined using X-ray PES (11.31 ± 0.04 eV,[31] 11.33 ± 0.03 eV).[42] Employing cross section set **I**, which was introduced by Signorell and coworkers[51] and employed in the original retrieval code,[79] gave a negative central eKE corresponding to a VIE of 12.49 ± 0.09 eV. This indicates that the cross sections at eKEs less than around 1 eV are too high. In their revised set of cross sections, Signorell reduced the contribution of the cross sections below 1 eV;[49] using cross section set **II** resulted in a VIE of 11.43 ± 0.09 eV, which is much closer to the X-ray values.[31,42] Finally, the two sets of cross sections derived from the extrapolation of amorphous ice cross sections[45] (**III**) and the combined amorphous ice and water droplet photoelectron data[50] (**IV**) gave VIEs of 11.31 ± 0.09 eV and 11.36 ± 0.09 eV, respectively. Both values are consistent with the VIE of water determined using X-ray PES.[31,42] In fact, the only notable difference between the two cross section sets lies in the magnitude of the elastic cross sections, as the total and most intense inelastic cross sections are not affected greatly. As expected, this has a smaller effect on the central eKE of the retrieved spectra. Motivated by these results, the extrapolated amorphous ice cross section set **III** was employed in the following sections, as it provides good agreement with the literature.

3.3.2 Escape Threshold

3.3.2.1 Distribution of Escape Angles

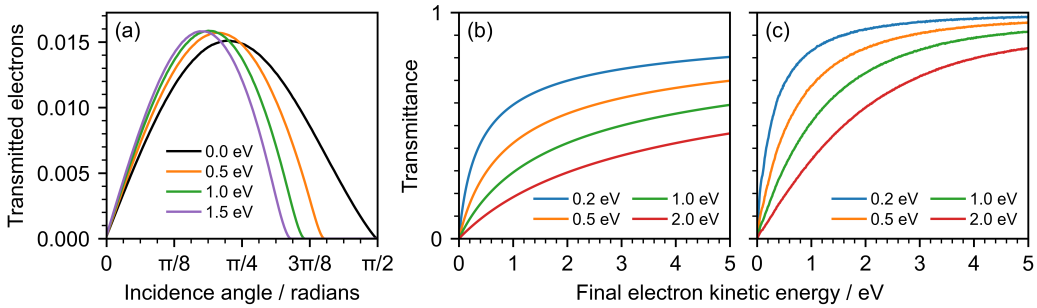

Figure 3.7: (a) Fraction of simulated electrons successfully escaping the jet as a function of the incidence angle with the surface, for different escape thresholds, determined using method **B**. (b-c) Ratio between the number of transmitted electrons in the presence of different escape barriers and the number of transmitted electrons without an escape barrier, as a function of final kinetic energy. Transmission was determined using (b) method **A**, and (c) method **B**. In these simulations, cross section set **III** was employed. Reproduced from Ref. 92. Further permissions related to the material excerpted should be directed to the American Chemical Society.

Figure 3.7a shows the distribution of the angles of incidence on the surface for electrons with kinetic energies between 0 and 5 eV that successfully escape the jet. Here, method **B** was employed, rather than assuming a uniform distribution of the velocity vectors of electrons reaching the surface. If the latter and no escape barrier are assumed, one would expect a $\sin\theta$ distribution of the incident angles.[45,77,78] However, these results show that the distribution more closely resembles a $\sin(2\theta)$ distribution and has a maximum slightly below $\pi/4$ radians.

To investigate this discrepancy, the angular distribution for a simplified model in which electrons are uniformly distributed below a flat surface, step lengths are sampled from an exponential distribution with a constant MFP, and all scattering events are elastic and isotropic was derived.[100] The distribution of incidence angles is given by

$$I(\theta, d, L) = \begin{cases} \frac{1}{2}\sin\theta & 0 \leq \theta \leq \arccos\left(\frac{d}{L}\right) \\ 0 & \arccos\left(\frac{d}{L}\right) < \theta \leq \frac{\pi}{2} \end{cases}. \tag{3.3}$$

where θ is the incidence angle, d is the depth and L is the step length. Integration over uniform d and L scaled by an exponential distribution gives the overall angular distribution

$$I(\theta) = \int_0^{d_{\max}} \int_0^{\infty} I(\theta, d, L) \frac{1}{\lambda} \mathrm{e}^{-\frac{L}{\lambda}} \,\mathrm{d}L \,\mathrm{d}d, \tag{3.4}$$

where $d_{\max}$ is the maximum depth and λ is the mean free path. As $L \geq \frac{d}{\cos\theta}$,

$$I(\theta) = \int_0^{d_{\max}} \int_{d/\cos\theta}^{\infty} \frac{1}{2\lambda} \mathrm{e}^{-\frac{L}{\lambda}} \sin\theta \,\mathrm{d}L \,\mathrm{d}d. \tag{3.5}$$

Integrating over L gives

$$I(\theta) = \frac{1}{2}\sin\theta \int_0^{d_{\max}} \mathrm{e}^{-\frac{d}{\lambda\cos\theta}} \,\mathrm{d}d. \tag{3.6}$$

Integrating over d gives

$$I(\theta) = \frac{\lambda}{2}\cos\theta\sin\theta\left(1 - \mathrm{e}^{-\frac{d_{\max}}{\lambda\cos\theta}}\right). \tag{3.7}$$

If $d_{\max} \ll \lambda$, as can be assumed for the amorphous ice films employed by Michaud et al.,[45] $1 - \mathrm{e}^{-\frac{d_{\max}}{\lambda\cos\theta}} \approx \frac{d_{\max}}{\lambda\cos\theta}$ and $I(\theta)$ is given by

$$I(\theta) = \frac{d_{\max}}{2}\sin\theta. \tag{3.8}$$

However, in a liquid jet, $d_{\max} \gg \lambda$, and $1 - \mathrm{e}^{-\frac{d_{\max}}{\lambda\cos\theta}} \approx 1$. $I(\theta)$ is thus given by

$$I(\theta) = \frac{1}{2}\lambda\cos\theta\sin\theta = \frac{1}{4}\lambda\sin(2\theta). \tag{3.9}$$

However, it is unlikely for the depth distribution to be uniform, as electrons near the surface have a higher probability of escaping. To verify this, a Monte Carlo simulation of this simplified model was performed by propagat-

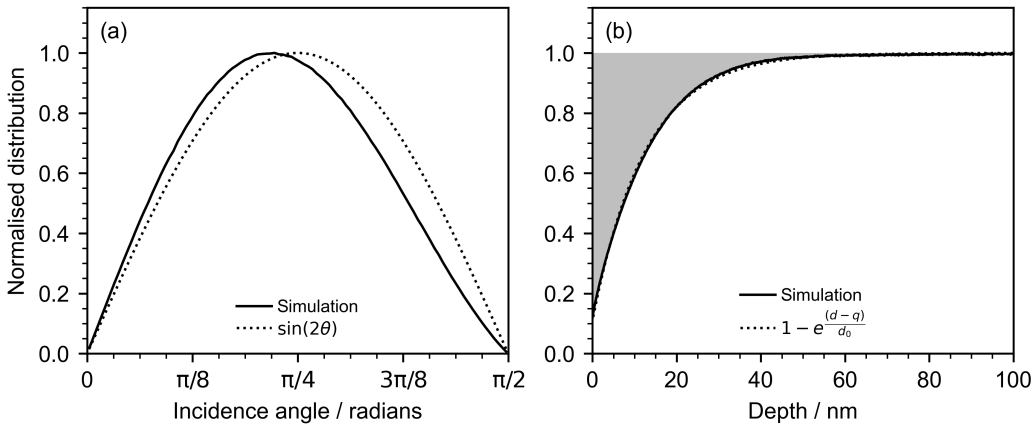

Figure 3.8: (a) Distribution of angles of incidence with the surface for electrons propagating under a semi-infinite flat surface. (b) Distribution of the depth of all electrons at all steps of the simulation (solid) fit with a shifted cumulative exponential distribution (dotted). The shaded area indicates the difference between the simulation and a uniform distribution. The distributions were obtained by performing random walks for electrons initialised at depths between 0.1 and 100 nm in 0.1 nm steps. Step lengths were sampled from an exponential distribution with a mean of 2.9 nm and electrons moved in a random direction. Trajectories were stopped after the electrons reached the surface. In (a) 10^5 electrons were propagated and trajectories were limited to 10^3 steps. In (b) 10^4 electrons were propagated and trajectories were limited to 10^2 steps. Reproduced from Ref. 92. Further permissions related to the material excerpted should be directed to the American Chemical Society.

ing 10^5 electrons with starting depths between 0.1 and 100 nm in 0.1 nm steps and limiting their trajectories to a maximum of 1 000 steps. If the depth of an electron became greater than 100 nm, the electron was specularly reflected to avoid unwanted depletion of electrons in the model. The trajectories of electrons that travelled through the surface were terminated and the angle of incidence on the surface determined. The results of this simulation show a distribution of angles with a peak below $\pi/4$ (Figure 3.8a). In an equivalent smaller simulation in which the number of electrons was 10^4 and trajectories were limited to 100 steps, the distribution of the depth from the surface of all electrons at each step was extracted and found to be well described by a cumulative exponential distribution (Figure 3.8b).

To test the effect of the distribution of depths, the distribution of the

angles of incidence using Monte Carlo integration and different depths profiles was determined as follows. Depths between 0 and 50 nm were sampled using a uniform distribution, an exponential distribution, or a cumulative exponential distribution. Step lengths were sampled from an exponential distribution and electrons moved one step in a random isotropic direction. If, after moving, the electron was outside the surface, the angle with the normal to the surface was measured; otherwise, it was discarded. This process was repeated 10^8 times yielding distributions of incidence angles for the three depth profiles (Figure 3.9). These results show that the presence of a non-uniform depth distribution of electrons inside the jet causes the distribution of incidence angles to deviate from a $\sin(2\theta)$ distribution, namely that the depletion of electrons near the surface shifts the maximum of the distribution to lower incidence angles while the accumulation of electrons near the surface shifts the maximum to higher incidence angles.

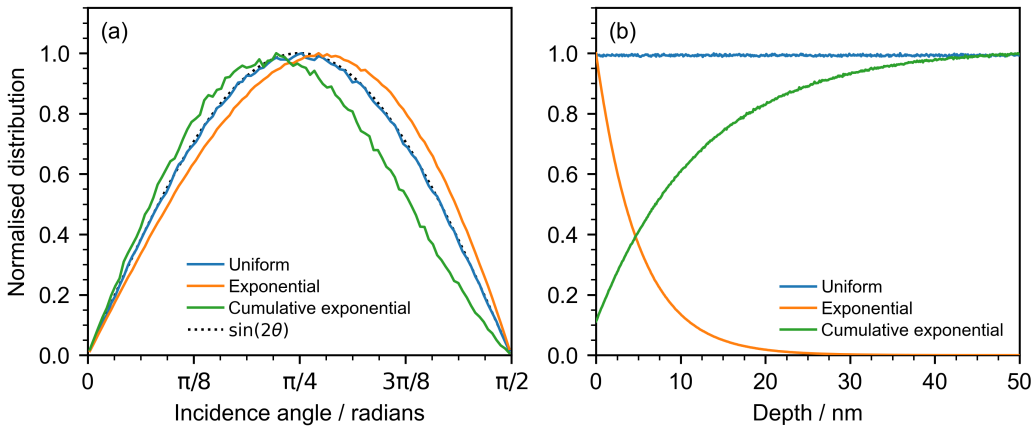

Figure 3.9: (a) Distribution of incidence angles obtained using Monte Carlo integration and a uniform distribution, an exponential distribution or a cumulative exponential distribution of depths (b) Distributions of depth employed to determine the angular distributions in (a) normalised to their maximum. Reproduced from Ref. 92. Further permissions related to the material excerpted should be directed to the American Chemical Society.

Inspired by the results in Figure 3.8, a cumulative exponential distribution with mean d_0 was used to scale d before integrating over d,

$$I(\theta) = \frac{1}{2}\sin\theta \int_0^{d_{\max}} \mathrm{e}^{-\frac{d}{\lambda\cos\theta}}\left(1 - \mathrm{e}^{-\frac{d}{d_0}}\right)\mathrm{d}d. \tag{3.10}$$

Assuming $d_{\max} \gg \lambda$ and $d_{\max} \gg d_0$ and integrating over d gives

$$I(\theta) = \frac{\lambda^2\cos^2\theta\sin\theta}{2(\lambda\cos\theta + d_0)}, \tag{3.11}$$

which has a maximum at an angle of less than $\pi/4$.

For nonzero escape barriers, the maximum shifts to lower angles as transmission does not occur above the maximum escape angle of electrons with an eKE of 5 eV (Figure 3.7a). Notably, the fraction of electrons transmitted at lower angles is greater when a barrier is present. This can be attributed to the fact that electrons that are reflected into the liquid will find themselves close to the surface and are thus likely to escape at a more favourable angle.

Overall, this phenomenon leads to a significantly different kinetic energy distribution of the transmitted electrons than when using method **A**. Figure 3.7b,c shows the ratio between the number of transmitted electrons in the presence of an escape barrier and the number of transmitted electrons without an escape barrier for both methods. Method **B** results in a larger number of transmitted electrons overall and a more significant contribution from lower energy electrons.

The obtained angular distributions can be employed to determine functions for the transmittance of electrons at the liquid-vacuum interface. In the presence of a potential energy barrier, the velocity component normal to the surface must exceed the escape velocity, i.e. $(E + E_0)\cos^2\theta > E_0$, where E_0 is the escape threshold. Therefore, the escape probability can be written as

$$P(\theta, E; E_0) = \begin{cases} I(\theta) & (E + E_0)\cos^2\theta > E_0 \\ 0 & \text{otherwise} \end{cases}. \tag{3.12}$$

Substituting the angular distribution obtained assuming a uniform distribution of escape velocity vectors (Equation 3.8) into Equation 3.12 gives the

following equation for the escape probability of electrons:

$$P(E;E_0) = \frac{d_{\max}}{4\pi}\int_0^{2\pi}\int_0^{\alpha(E)} \sin\theta\,\mathrm{d}\theta\,\mathrm{d}\phi, \tag{3.13}$$

where θ is the polar angle and ϕ is the azimuthal angle in spherical coordinates, and $\alpha(E) = \arccos\left(\sqrt{\frac{E_0}{E+E0}}\right)$. Integrating over θ and ϕ gives

$$P(E;E_0) = \frac{d_{\max}}{4}\left(1-\sqrt{\frac{E_0}{E+E_0}}\right). \tag{3.14}$$

The transmittance at the surface $T(E)$ is given by the escape probability relative to the escape probability when $E_0 = 0$,

$$T(E) = 1-\sqrt{\frac{E_0}{E+E_0}}, \tag{3.15}$$

which was employed by several groups.[45,77,78]

Similarly, substituting the angular distribution in which the radius of liquid jets being much larger than the MFP was accounted for and electrons are assumed to be uniformly distributed below the surface (Equation 3.9) into Equation 3.12 one obtains the following probability distribution:

$$P(E;E_0) = \frac{\lambda}{4\pi}\int_0^{2\pi}\int_0^{\alpha(E)} \cos\theta\sin\theta\,\mathrm{d}\theta\,\mathrm{d}\phi, \tag{3.16}$$

where $\alpha(E) = \arccos\left(\sqrt{\frac{E_0}{E+E0}}\right)$. Integrating over θ and ϕ gives

$$P(E;E_0) = \frac{\lambda}{4}\cdot\frac{E}{E+E_0}. \tag{3.17}$$

The transmittance at the surface $T(E)$ is given by

$$T(E) = \frac{E}{E+E_0}. \tag{3.18}$$

Finally, substituting the angular distribution obtained by using a cumulative exponential distribution to describe the distribution of electrons inside the jet (Equation 3.11) into Equation 3.12 one obtains the following probability

distribution:

$$P(E;E_0) = \int_0^{\alpha(E)} \frac{\lambda^2 \cos^2\theta \sin\theta}{2(\lambda\cos\theta + d_0)}\,\mathrm{d}\theta. \tag{3.19}$$

Integrating over θ gives

$$\begin{aligned} P(E;E_0) =& \frac{\lambda}{4}\cdot\frac{E}{E+E_0} + \frac{d_0}{2}\left(\sqrt{\frac{E_0}{E+E_0}} - 1\right) \\ &- \frac{d_0^2}{2\lambda}\ln\left(\lambda\sqrt{\frac{E_0}{E+E_0}} + d_0\right) + \frac{d_0^2}{2\lambda}\ln(\lambda + d_0). \end{aligned} \tag{3.20}$$

The transmittance is given by

$$T(E;E_0) = \frac{P(E;E_0)}{P(E;0)}. \tag{3.21}$$

Figure 3.10 shows a comparison between the transmittance determined using Equation 3.15, 3.18 and 3.21 (full lines) compared to the transmittance obtained from the Monte Carlo simulations shown in Figure 3.7c (shaded lines). Equation 3.21 was fit to the data in Figure 3.7c to obtain values for λ and d_0.

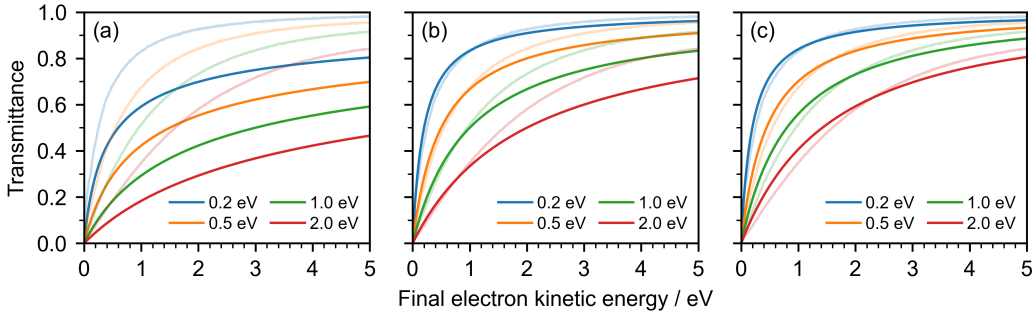

Figure 3.10: Transmittance determined using (a) Equation 3.15, (b) Equation 3.18 and (c) Equation 3.21 (full lines). Shaded lines indicate the transmittance obtained from the Monte Carlo simulations shown in Figure 3.7c using method **B** and cross section set **III**. Equation 3.21 was fit to the shaded lines to obtain values for λ and d_0. Reproduced from Ref. 92. Further permissions related to the material excerpted should be directed to the American Chemical Society.

3.3.2.2 Effect on Spectral Retrieval

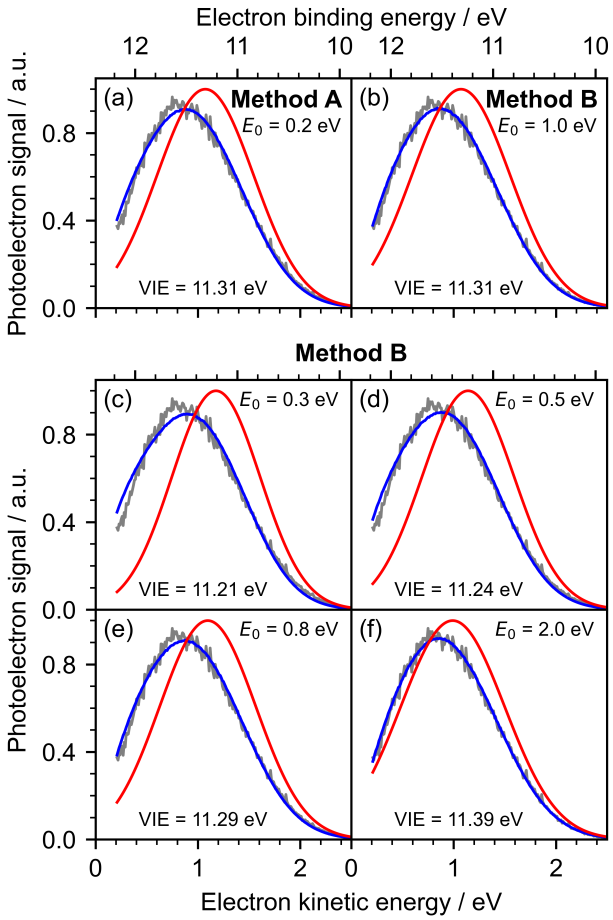

Figure 3.11: Photoelectron spectrum of water recorded at 200.2 nm retrieved using the two methods of calculating the transmission of electrons at the liquid-vacuum interface with different escape thresholds. Blue lines are fits to the data, red lines are retrieved spectra, and numbers in eV are the ionisation energies of water determined for each method. (a) Method **A** with an escape threshold of 0.2 eV was used. (b) Method **B** with an escape threshold of 1.0 eV was used. (c-f) Method **B** with escape thresholds between 0.3 and 2.0 eV was used. All spectral retrievals employed cross section set **III**. Reproduced from Ref. 92 with experimental spectra adapted from Ref. 79. Further permissions related to the material excerpted should be directed to the American Chemical Society.

The effect of using methods **A** or **B** can be observed when applying the spectral retrieval to the 200.2 nm photoelectron spectrum of water (Figure 3.11a, b). Method **A** requires an escape threshold 5 times lower than method **B** to describe the spectrum accurately. This suggests that the discrepancy

between the escape threshold obtained by Suzuki's group (0.2 eV)[77] and that employed by Signorell and co-workers[51] and previously in our group[79] (1.0 eV) can be attributed to the assumption that the distribution of incidence angles of electrons at the surface is $\sin(\theta)$.

Next, the effect of the value of the escape threshold on the retrieval of the 200.2 nm photoelectron spectrum of water was investigated using method **B** (Figure 3.11c-d). As the spectrum has a significant contribution from electrons with eKEs below 1 eV, the choice of escape threshold affects the position of the retrieved peak significantly, and higher E_0 values yield better fits and values more consistent with previous accurate measurements.[31,42] It is worth noting that the shape of distorted spectra at low eKE is also dictated by the scattering cross sections at these eKEs and more than one combination of cross section set and escape threshold yield the same result. An escape threshold of 1 eV was chosen and employed with cross section set **III** to retrieve the spectra of water, phenol and phenolate, because this value was consistent with previous studies and yields VIEs and VDEs consistent with X-ray PES experiments.

3.3.3 Sensitivity Analysis

In order to verify the choice of parameters employed in this work, the effect of changing several input parameters on the result of the spectral retrieval code was tested. For the sensitivity study described in this section, cross section set **III** and method **B** were employed in the Monte Carlo simulations.

Number of starting electrons. Figure 3.12 shows the retrieval of the photoelectron spectra of water, phenol and phenolate as a function of the number of starting electrons employed at each depth and starting eKE in the Monte Carlo simulation. The choice to employ 10^4 electrons per E_i and d was driven by the fact that the retrieved photoelectron spectra for bulk water and surface bound organic solutes were consistent with those retrieved using a larger number of electrons and the fits (blue) have an acceptable signal-to-noise ratio.

Simulation depth and step size. Figure 3.13 shows the effect of the step size used when sampling the depths from the surface of the jet on the retrieval

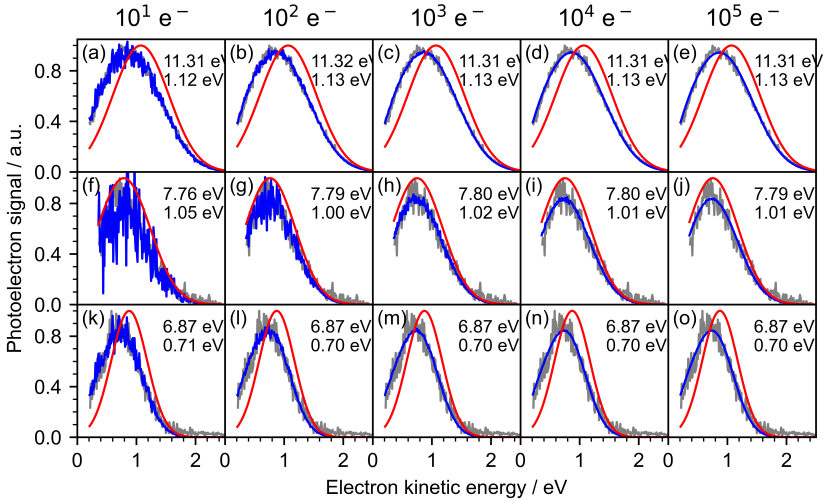

Figure 3.12: Effect of the number of starting electrons at each depth on the retrieval of the spectra of (a-e) water, (f-j) phenol and (k-o) phenolate. Gray lines are the experimental data, blue lines are fits to the data, red lines are retrieved spectra, and numbers in each panel are the retrieved eBEs (top) and FWHMs (bottom). Reproduced from Ref. 92 with experimental spectra adapted from Ref. 79. Further permissions related to the material excerpted should be directed to the American Chemical Society.

of the photoelectron spectra of water, phenol and phenolate. Using a step size of 0.1 nm or smaller gives consistent results. A step size of 1 nm shifts the eBE of water and phenolate by only a few tens of meV because most of the signal comes for the bulk. The eBE of phenol is shifted by 0.2 eV as the step size is too large to properly account for the enhanced surface contribution.

Figure 3.14 shows the distribution of electrons that escape the jet as a function of depth for depths between 0.1 and 100 nm and several starting eKEs. Most electrons originate from within a few tens of nm below the surface. A maximum depth of 50 nm was employed in the simulations as the contribution of electrons from below this depth is negligible.

Radius of the jet. Due to evaporation, the size of the jet at the interaction region is likely smaller than the size of the fused silica nozzle. Therefore, the effect of jet radii between 0.5 and 25 µm on the retrieval of the photoelectron spectra of water, phenol and phenolate was tested and virtually no difference in the retrieved spectra was found (Figure 3.15).

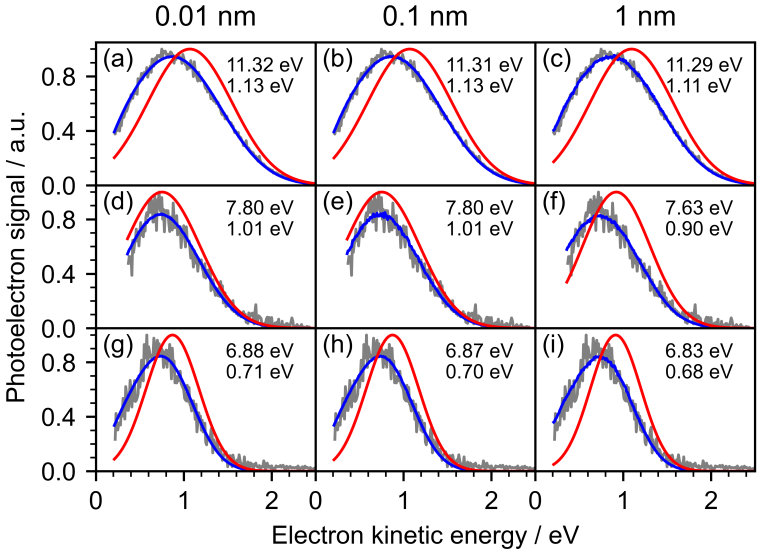

Figure 3.13: Effect of the step size used in the sampling of d on the retrieval of the photoelectron spectra of (a-c) water, (d-f) phenol and (g-i) phenolate. Electrons were initialised at depths between 0 and 50 nm. Gray lines are the experimental data, blue lines are fits to the data, red lines are retrieved spectra, and numbers in each panel are the retrieved eBEs (top) and FWHMs (bottom). Reproduced from Ref. 92 with experimental spectra adapted from Ref. 79. Further permissions related to the material excerpted should be directed to the American Chemical Society.

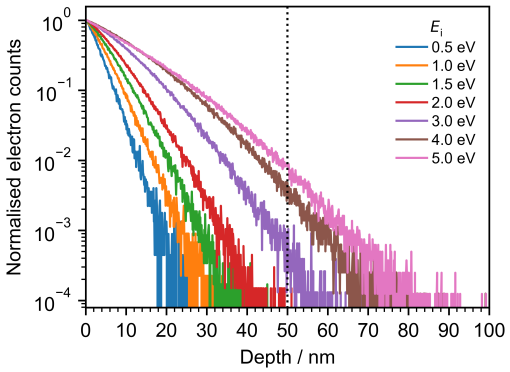

Figure 3.14: Distribution of electrons that successfully escape the jet as a function of depth for different initial kinetic energies, normalised to the number of electrons that originate at a depth of 0.1 nm. A step size of 0.1 nm was employed. This simulation was run using method **B** with an escape threshold of 1.0 eV and cross section set **III**. Adapted from Ref. 92. Further permissions related to the material excerpted should be directed to the American Chemical Society.

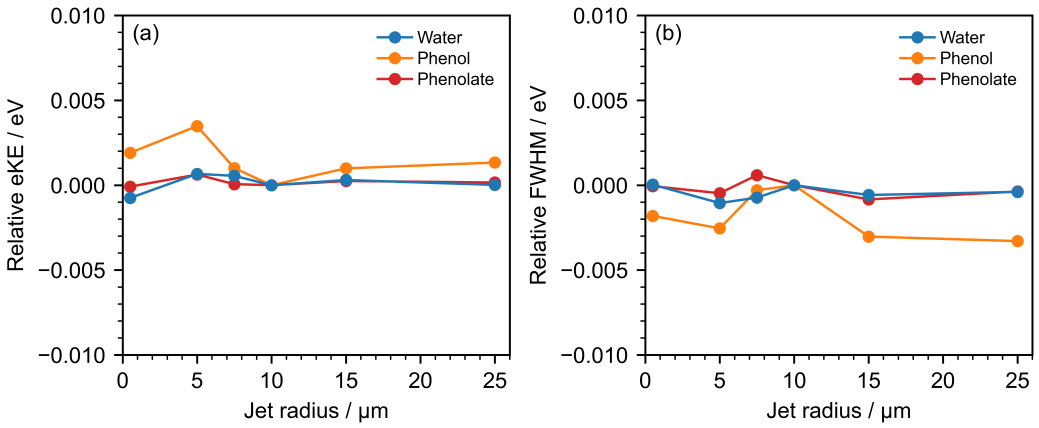

Figure 3.15: Effect of the radius of the jet on the retrieval of the photoelectron spectra of water, phenol and phenolate. (a) Change in the central eKE relative to the eKE retrieved with a radius of 10 µm. (b) Change in the FWHM relative to the FWHM retrieved with a radius of 10 µm. Simulations were run using method **B** with an escape threshold of 1.0 eV and cross section set **III**. Reproduced from Ref. 92. Further permissions related to the material excerpted should be directed to the American Chemical Society.

Relative contribution of elastic and inelastic cross sections. The effect of the relative contribution of the elastic and total inelastic cross sections on the retrieval of the photoelectron spectra of water, phenol and phenolate was tested by multiplying their ratio by a scaling factor, while keeping their sum constant (Figure 3.16). For Gaussians with centres below 1.5 eV, as is the case for the UV photoelectron spectra presented in this work, there is very little difference (< 0.03 eV) as the escape threshold has a large effect. For Gaussians centred at higher eKEs, increasing the relative contribution of the elastic cross sections has a noticeable effect on the distorted distribution (Figure 3.17).

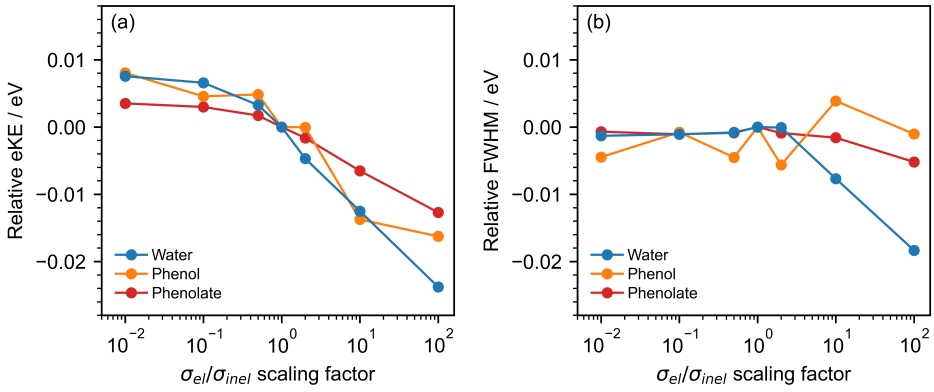

Figure 3.16: Effect of the relative contribution of the total inelastic and elastic cross sections on the retrieval of the photoelectron spectra of water, phenol and phenolate. The ratio of elastic to total inelastic cross sections was multiplied by a scaling factor, while their sum was kept constant. (a) Change in the central eKE relative to the eKE retrieved with no scaling factor applied. (b) Change in the FWHM relative to the FWHM retrieved with no scaling factor applied. Simulations were run using method **B** with an escape threshold of 1.0 eV and cross section set **III**. Concentration profiles with Gaussian-offset ratios of 20 and 1 were employed for phenol and phenolate, respectively. Reproduced from Ref. 92. Further permissions related to the material excerpted should be directed to the American Chemical Society.

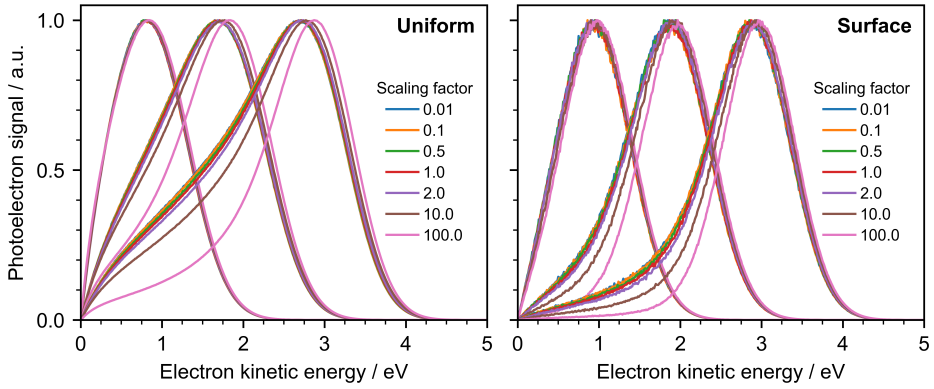

Figure 3.17: Effect of the relative contribution of the total inelastic and elastic cross sections on the distortion of Gaussians centred at 1, 2 and 3 eV. The ratio of elastic to total inelastic cross sections was multiplied by a scaling factor, while their sum was kept constant (a) A uniform concentration profile was employed. (b) A concentration profile with a Gaussian to offset ratio of 20 was employed. Simulations were run using method **B** with an escape threshold of 1.0 eV and cross section set **III**. Reproduced from Ref. 92. Further permissions related to the material excerpted should be directed to the American Chemical Society.

3.3.4 Concentration Depth Profiles

Figure 3.18a shows the distribution of phenol and phenolate as a function of depth below the surface, determined using molecular dynamics simulations. Both molecules have an enhanced surface concentration and a bulk contribution to the concentration depth profile. The ratio between the surface and bulk contributions is consistent with surface tension and photoelectron spectroscopy studies of phenol and phenolate, which showed a stronger surface propensity for phenol.[54,101] Since the simulation does not model the fall in the density of water at the interface, the depth dependence of the concentration was approximated as the sum of a Gaussian centred 0.1 nm below the surface with a 0.4 nm FWHM and a vertical offset (Figure 3.18a), and ratios between the height of the Gaussian and the offset of 20 and 1 were obtained for phenol and phenolate, respectively.

Figure 3.18b, c shows the dependence of the retrieved eKEs of phenol and phenolate on the ratio between the height of the Gaussian and the offset. Here, the retrieval process was employed on the non-resonant 1+1 MPI photoelectron spectra of 0.1 mM solutions of phenol and phenolate.[79] For both molecules, the retrieved eKE decreases rapidly with the height of the Gaussian and reaches a plateau at around 10, resulting in a shift of up to around 0.15 eV between a purely bulk and a purely surface species. Vertical dotted lines indicate the Gaussian-offset ratio observed in the MD simulations.

Figure 3.19a-d shows the retrieval of the non-resonant photoelectron spectra of 0.1 mM solutions of phenol and phenolate, obtained with Gaussian-offset ratios of 20 and 1, respectively. The spectra in Figures 3.19a,b show contributions from both the solute (pink Gaussians) and the solvent (green Gaussians), while those in Figures 3.19c,d were obtained by subtracting the fits of solvent-only spectra.

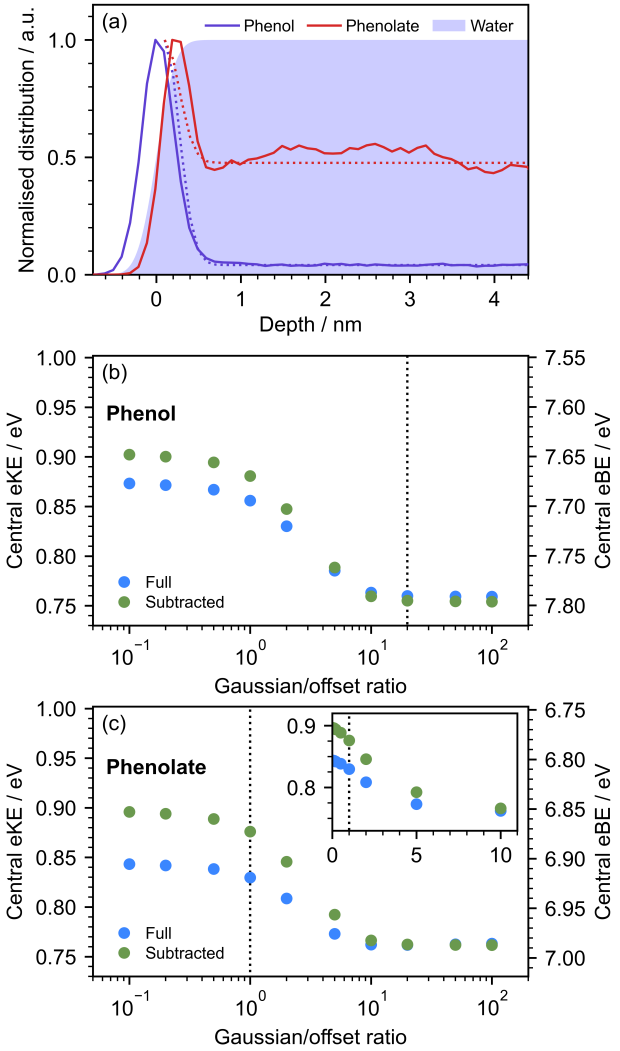

Figure 3.18: (a) Normalised concentration depth profile of phenol (violet) and phenolate (red) in aqueous solution near the liquid-vacuum interface, determined from MD simulations using the centre of mass of each solute along the normal to the surface. The blue shaded area represents the distribution of the oxygen atoms of water molecules fit with a cumulative normal distribution normalised to 1; its mean is taken as the liquid-vacuum interface. Dotted lines are the concentration profiles employed in the retrieval of the photoelectron spectra of phenol and phenolate. Retrieved eKEs and eBEs of the (b) 290 nm two-photon non-resonant MPI phenol spectrum and (c) the 320 nm two-photon non-resonant MPI phenolate spectrum including (blue) and excluding (green) solvent contributions as a function of relative height of the surface Gaussian. Inset: retrieved eKEs plotted on a linear scale. Vertical dotted lines indicate the ratios obtained from (a). Reproduced from Ref. 92. Further permissions related to the material excerpted should be directed to the American Chemical Society.

Table 3.3: Vertical binding energies of aqueous phenol and phenolate.

	Phenol		Phenolate	
	Conc. / mM	VIE / eV	Conc. / mM	VDE / eV
UV LJ-PES full (retr.)	0.1	7.79 ± 0.09	0.1	6.92 ± 0.09
UV LJ-PES subtracted (retr.)	0.1	7.80 ± 0.09	0.1	6.87 ± 0.09
X-ray LJ-PES[a] (200 eV)	750	7.8 ± 0.1	750	7.1 ± 0.1
EUV LJ-PES[b] (40-56.5 eV)	25	7.90 ± 0.04	50	7.3 ± 0.1
UV droplet PES[c] (4.30 eV)	10	7.9 ± 0.1		

[a]Ref. 102. [b]Ref. 101. [c]Ref. 103

The spectrum of 0.1 mM phenol comprises a 'surface' Gaussian and a 'bulk' Gaussian originating from two-photon non-resonant ionisation of phenol and three-photon non-resonant ionisation of water. VIEs of 7.79 ± 0.09 eV and 7.80 ± 0.09 eV were obtained for the full and subtracted spectra, respectively. Several studies have reported the VIE of aqueous phenol. An X-ray PES work found a VIE of 7.8 ± 0.1 eV for a 750 mM solution,[102] which was obtained by calibrating the spectrum using a value for the VIE of water of 11.16 eV.[27] A more recent study by Yamamoto et al. investigated the VIE of phenol recorded with 40.0 eV femtosecond pulses as a function of phenol concentration.[101] They observed a decrease in the VIEs of water and phenol at higher phenol concentrations, which they attributed to a decrease in surface potential caused by a higher surface concentration of the solute. For a solution of 25 mM, the measured VIE of water was the same as the VIE of pure water, suggesting that surface potential effects were insignificant and thus they quoted a value of 7.90 ± 0.04 eV for the VIE of phenol.[101] Furthermore, a velocity-map photoelectron imaging study of aqueous phenol aerosol droplets also observed a decrease in the VIE of phenol from 7.9 ± 0.1 eV for a 10 mM solution to 7.4 ± 0.1 eV for a 800 mM solution and attributed this trend to the formation of aggregates of phenol at the surface at higher concentrations.[103] These results are expected to be unaffected by a shift in surface potential or

the formation of aggregates, as the surface concentration for a 0.1 mM solution is at least two orders of magnitude lower than surface concentrations investigated in previous studies.[54,101,103] There is good agreement between the VIE of phenol retrieved with the spectral retrieval code and previously reported VIEs in liquid jets and aerosol droplets.[101–103]

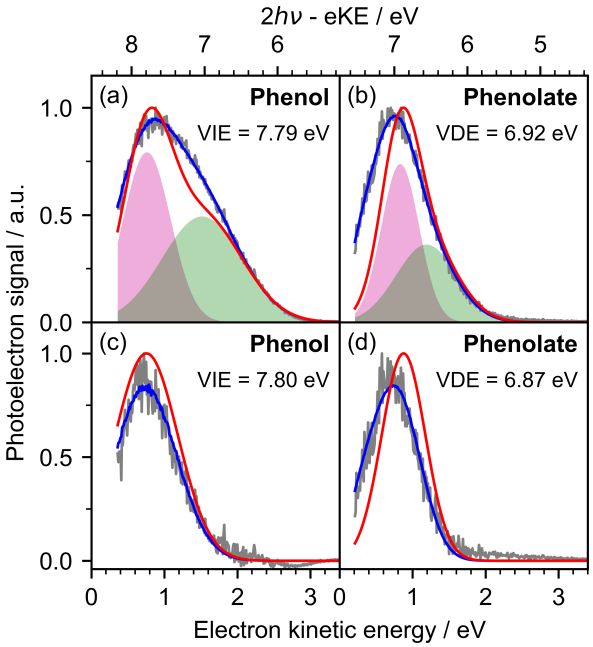

Figure 3.19: Retrieval of the (a, c) 290 nm photoelectron spectra of 0.1 mM phenol and (b, d) 320 nm photoelectron spectra of 0.1 mM phenolate. Spectra (a) and (b) include solute (pink Gaussians) and solvent (green Gaussians) contributions. Solvent-only spectra were fit with a 'bulk' Gaussian and subtracted from spectra (a) and (b) to give the solute-only spectra in (c) and (d). Grey lines are the experimental spectra, blue lines are fits to the data, red lines are retrieved spectra. All spectral retrievals employed cross section set **III**, and method **B** with an escape threshold of 1 eV. Reproduced from Ref. 92 with experimental spectra adapted from Ref. 79. Further permissions related to the material excerpted should be directed to the American Chemical Society.

The spectrum of 0.1 mM phenolate can also be described as the sum of a 'surface' Gaussian originating from ionisation of phenolate and a 'bulk' Gaussian originating from ionisation of the solvent. The phenolate contribution has a peak at 6.92 ± 0.09 eV, which agrees well with the value obtained from the subtracted spectrum, 6.87 ± 0.09 eV. The VDE of phenolate measured

with X-ray PES was reported to be 7.1 ± 0.1 eV for a 750 mM solution,[102] which was also determined with a value of 11.16 eV for the VIE of water.[27] More recently, Yamamoto et al. performed EUV measurements and measured a VDE of 7.3 ± 0.1 eV for a 50 mM solution.[101] Curiously, the value obtained in this work is 0.3 eV less than the value obtained from EUV measurements and within error of the VDE obtained from an X-ray measurement that was calibrated using a value for the VIE of water that has been subsequently refined. A possible explanation for this difference could be that UV LJ-PES has a greater bulk sensitivity than EUV LJ-PES, and the UV measurements reported by Scholz et al. were able to capture the significant bulk contribution of phenolate.[79] In fact, changing the surface Gaussian and bulk offset in the modelled concentration profile of phenolate yields a VDE closer to values measured with EUV light (Figure 3.18c). One must also note that the experimental conditions differ from those employed in EUV and X-ray experiments; namely, concentrations at least 2 orders of magnitude lower than those that are feasible in EUV and X-ray measurements were used, and no bias was applied to the liquid jet.

3.4 Conclusions and Outlook

The work presented in this chapter focused on conducting a systematic investigation of the parameters required to describe electron transport in liquid water and retrieve accurate photoelectron spectra from UV liquid-microjet spectroscopy measurements, which have been been subject to debate in the literature. The effect of the low-energy (< 5 eV) electron scattering cross sections in water, the parameters employed to describe the transmission of electrons through the water-vacuum interface, and the effect of the propensity of poorly-soluble organic molecules for the surface of water were explored. A VIE for water that is in excellent agreement with the VIE obtained from accurate X-ray measurements was obtained by employing the cross sections derived from amorphous ice extrapolated to 0 eKE, determining the transmission of

electrons at the liquid-vacuum interface using the component of the electron kinetic energy perpendicular to the surface, and employing an escape threshold of 1 eV. The VIE and VDE of sub-mM solutions phenol and phenolate were also presented and found to be in agreement with earlier X-ray photoelectron spectroscopy measurements in liquid jets and liquid droplets. Overall, the findings presented in this chapter enhance the accuracy of the spectral retrieval of UV liquid-jet photoelectron spectra and highlight the potential of UV LJ-PES for studying electronic structure and excited state dynamics of aqueous solutions.

Future work will focus on extending the Monte Carlo simulation to higher eKEs by including the effects of electronic scattering to model EUV photoelectron spectra. A EUV and X-ray photoelectron study of aqueous phenol and phenolate has revealed that the the dependence of their photoelectron signal intensity on concentration can be described by the Langmuir adsorption model.[54] Concentration studies of phenol and phenolate using UV pulses and several EUV photon energies could provide experimental insight into the probing depth of UV and EUV LJ-PES. Additionally, an investigation of the effect of applying a bias voltage to the liquid jet, which represents a major difference between UV PES measurements and X-ray and EUV LJ-PES, is planned.

Chapter 4

X-ray, EUV and UV photoelectron spectroscopy of the photoactive yellow protein chromophore in aqueous solution

The photoactive yellow protein (PYP) is a prototypical biological photoreceptor. Its photocycle is initiated by the absorption of a photon of blue light by its chromophore *para*-coumaric acid, inducing *trans-cis* isomerisation about its double bond. A detailed picture of the electronic structure of the PYP chromophore is essential to improve our understanding of photoactive proteins. While several studies have investigated the electronic structure of model PYP chromophores in the gas-phase, no study to date has addressed the influence of a more complex environment on their electronic structure. In this chapter, a combined X-ray, EUV and UV liquid-microjet photoelectron spectroscopy (LJ-PES) study of the methyl ester analogue of the PYP chromophore ($p\mathrm{CE}^-$) in aqueous solution is presented. The first two vertical detachment energies of $p\mathrm{CE}^-$ were determined with X-ray and EUV LJ-PES. Resonance-enhanced multiphoton detachment of $p\mathrm{CE}^-$ via its first excited state allowed the identifi-

cation of a high-lying excited state near the detachment continuum, previously implicated in the formation of solvated electrons, and the first observation of a resonance embedded within the detachment continuum for an anion in solution. These results shed new light on the electronic structure of a model PYP chromophore in solution and, more generally, anions in water.

4.1 Introduction

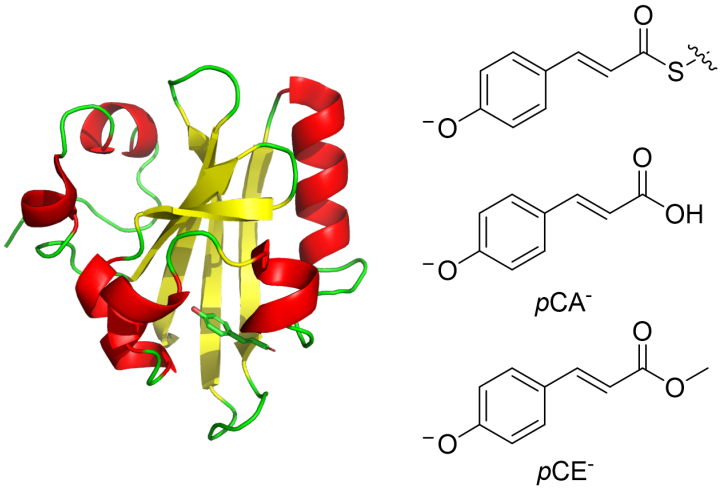

Figure 4.1: Left: Ribbon representation of the structure of the photoactive yellow protein. The image was created with PyMOL with the structure obtained from the Protein Data Bank (rcsb.org) with ID: 2PHY.[104] Right: Structure of $p\text{CA}^-$ bonded to the protein, isolated $p\text{CA}^-$ and isolated $p\text{CE}^-$.

Photoactive proteins are ubiquitous in biological systems and often control the response of living organisms to light in their environment. One notable example is the photoactive yellow protein (Figure 4.1), which has been studied extensively as a prototypical photoreceptor and is responsible for the negative phototaxis of the *Halorhodospira halophila* bacterium.[105] At the heart of PYP is its chromophore (Figure 4.1), deprotonated *trans*-*p*-coumaric acid ($p\text{CA}^-$), which is bound to a cysteine residue via a thioester link and stabilised by a network of hydrogen bonds. The photocycle of PYP (Figure 4.2) has been investigated using several experimental techniques including X-ray crystallography,[106–109] transient absorption[110–114] and infrared spectroscopy.[115–117] It is

initiated by the absorption of a photon of blue light (λ_{max} = 446 nm) and the consequent *trans-cis* isomerisation of the double bond of the chromophore induces a cascade of structural changes of the protein, signalling the presence of harmful radiation. A clear picture of the electronic structure of the chromophore and how complex environments can tune its photoresponse is essential to obtain a comprehensive understanding of the isomerisation process involved in the photocycle.

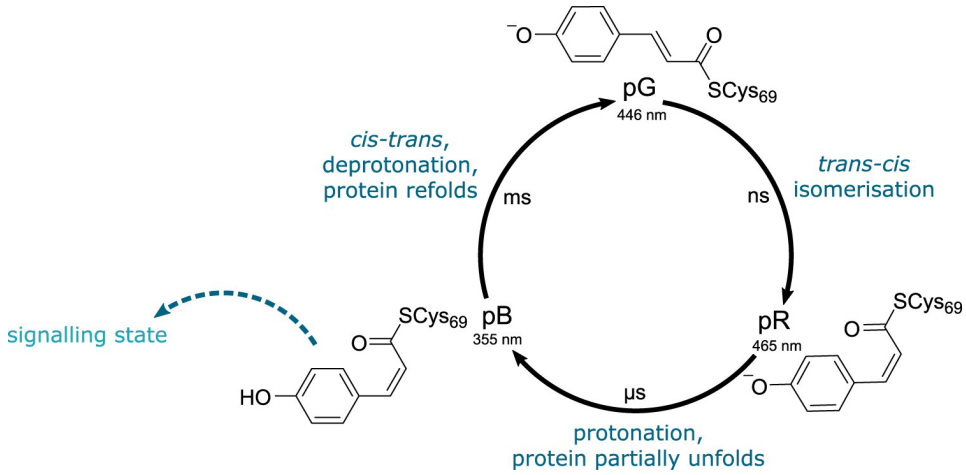

Figure 4.2: Main steps of the photocycle of PYP, showing the major intermediates and associated timescales. The photocycle is initiated by the absorption of blue light by the chromophore *p*CA$^-$. *Trans-cis* isomerisation of the chromophores ultimately leads to the formation of a red-shifted intermediate pR. Protonation of the chromophore results in partial unfolding of the protein, which is thought to be the signalling state. Recovery of the *trans* ground states is achieved by the deprotonation of *p*CA, *cis-trans* isomerisation and refolding of the protein. Reproduced Henley, A.; Fielding, H. H., *Int. Rev. Phys. Chem.* **2019**, *38*, 1–4. Copyright 2019, reprinted by permission of Informa UK Limited, trading as Taylor & Francis Group.

As *p*CA has two deprotonation sites and the carboxylic acid moiety has a lower pK_a than the phenol moiety, the work in this chapter focuses on the electronic structure of the methyl ester analogue of *p*CA$^-$ (*p*CE$^-$, Figure 4.1), to ensure only the phenolate form is present and better represent the structure of the chromophore inside the protein. The excited state dynamics of this PYP chromophore are discussed in detail in Chapter 5.

One of the most powerful experimental techniques for the study of elec-

tronic structure of molecules is photoelectron spectroscopy (PES) as it most directly accesses electron binding energies. While gas-phase anion PES studies have focused on the electronic structure of the isolated PYP chromophore and several of its derivatives,[118–125] no PES studies of the PYP chromophore have been conducted in more complex environments, such as aqueous solution.

In the gas phase, the first vertical detachment energy (VDE) of $p\mathrm{CA}^-$ was determined to be 2.92 ± 0.05 eV,[120] and, as the vertical excitation energy of the first excited state lies close to the detachment continuum, photoelectron spectra of $p\mathrm{CA}^-$ are characterised by autodetachment features. Studies of the impact of chemical and structural modifications of the isolated PYP chromophore have highlighted the role of substituent groups at the carbonyl tail (Figure 4.3) on the electronic structure and excited state dynamics.[118–126] It was found that chromophores with stronger electron-accepting groups had higher VDEs, due to higher stabilising effects of the substituents.[119] Studies on chromophores with either the double bond or one of the single bonds adjacent to the double bond locked led to the understanding that both rotations about the single bond between the double bond and the phenolate and the double bond (Figure 4.3) guide the molecule towards conical intersections with the ground state.[120]

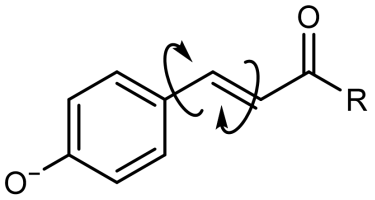

Figure 4.3: The PYP chromophore and its analogues can undergo rotation about the double bond or the single bond between the phenolate moiety and the double bond. R indicates the position of the substituting groups, which include O^-, NH_2, OMe, CH_3, SMe and SPh.

Similar observations have been obtained from time-resolved experiments of PYP chromophore analogues in aqueous solution.[127–137] It was found that the electron-accepting character of the substituting group at the carbonyl tail dictates whether isomerisation occurs and affects the timescales associated

with relaxation. Chromophores with strong electron acceptors, like $p\mathrm{CE}^-$ or the ketone analogue, quickly relax via a phenolate-twisted ground-state intermediate to the *trans* isomer, whereas chromophores with weak electron acceptors, such as the amide derivative or the dianion of $p\mathrm{CA}$ ($p\mathrm{CA}^{2-}$), relax directly to the *cis* isomer on a slower time scale.[133,134,137] Notably, $p\mathrm{CA}^{2-}$, which contains the weakest electron accepting group, relaxes on a 10 ps timescale, while the ketone derivative, which contains the strongest electron acceptor, relaxes on a 1.2 ps timescale.[132–134,136,137]

The formation of solvated electrons after excitation of PYP and PYP chromophores in aqueous solution has been observed in transient absorption spectroscopy (TAS) experiments.[111,113,114,127,130,131,133,134,136] It was proposed to arise from a resonant two-photon excitation, due to the quadratic dependence of the solvated electron signal on the excitation pulse energy. However, the mechanism of its formation is still debated, particularly regarding whether it arises from a charge-transfer-to-solvent state or from a resonant intermediate in a [1+1] excitation process.[114] For PYP in aqueous solution, the diffusion of the solvated electron controls geminate recombination with the radical of the chromophore, and the diffusion coefficient determined from the geminate recombination timescale was similar to that in water.[114] Therefore, investigating the higher-lyingh states proposed to be involved in the formation of solvated electrons in aqueous solution can provide information about the photoredox properties of this important chromophore, which can be used as a basis for understanding similar processes *in vivo*.

In the work presented in this chapter, a combination of X-ray, EUV, and UV LJ-PES has been carried out to investigate the electronic structure of $p\mathrm{CE}^-$. The first two vertical detachment energies of the chromophore were determined with X-ray and EUV radiation. The photodetachment pathways and the role of the first and higher-lying excited states in the photoisomerisation process and formation of solvated electrons were investigated with UV LJ-PES.

4.2 Experimental Details

Aqueous solutions of pCE$^-$ were prepared with pCE (>98.0%, Tokyo Chemical Industries) and NaOH (Sigma Aldrich). In the X-ray and EUV LJ-PES measurements, NaF and NaCl were also added to the solutions, respectively, to ensure sufficient electrical conductivity of the solutions. The concentrations for each measurement are given in Sections 4.2.1, 4.2.2 and 4.2.3. UV-visible steady-state absorption spectra of (i) 50 µM pCE in 2.0 mM aqueous NaOH and (ii) 2.0 mM aqueous NaOH were recorded with a UV-2600i spectrophotometer (Shimadzu) and a 4 mm path length. Steady-state fluorescence spectra of 50 µM pCE in 2.0 mM aqueous NaOH were recorded with a FluoroMax-4 spectrofluorometer (Horiba).

4.2.1 X-ray photoelectron spectroscopy

X-ray LJ-PES experiments of pCE$^-$ were performed by collaborators in the group of Bernd Winter at BESSY (Berlin) and first analysed by Alice Henley (PhD thesis).[138] However, as the value for the VIE of water used to calibrate the spectra has since been refined,[31,42] this analysis is revisited in this chapter.

The experimental procedure is described in detail in Ref. 138. Briefly, photoelectron spectra of 5.0 mM pCE in aqueous solution with 5.5 mM NaOH and 30 mM NaF were recorded at the U49/2 PGM-1 beamline (20×80 µm^2 focal size) of BESSY II (Berlin), using a photoelectron spectrometer detailed elsewhere,[139] which consists of a differentially pumped hemispherical electron analyser and an interaction chamber. Solutions were cooled to 12 °C and introduced in the interaction chamber via a 25 µm diameter fused silica nozzle with an approximate velocity of 20 m s^{-1}. No bias was applied to the liquid jet. The photon energy was 180 eV and the energy resolution of the experiment was < 125 meV, determined by the energy resolution of the detection scheme (∼100 meV) and of the beam line (∼100 meV).

4.2.2 Extreme ultraviolet photoelectron spectroscopy

EUV LJ-PES measurements of pCE$^-$ were performed in collaboration with Iain Wilkinson in Bernd Winter's laboratory at the Fritz Haber Institute (Berlin). Photoelectron spectra were recorded using the He I α ($h\nu$ = 21.22 eV) and He II α ($h\nu$ = 40.81 eV) discharge lines of a helium lamp. Experiments were performed using the EASI (Electronic structure of Aqueous Solutions and Interfaces) setup,[140] which consists of a differentially pumped hemispherical electron analyser and an interaction chamber housing a liquid microjet. A solution of 5.0 mM pCE in aqueous 5.5 mM NaOH and 50 mM NaCl was cooled to 20 °C, and a −25 V bias was applied to the solution before being introduced in the chamber through a 26 µm diameter fused silica nozzle using a high performance liquid chromatography pump at a flow rate of 1.5 ml/min. The pressure in the interaction region was maintained between 1×10^{-4} and 4×10^{-4} mbar. The liquid jet was intersected by radiation originating from the helium lamp and photoelectrons were detected by the hemispherical analyser in 25 meV energy bins.

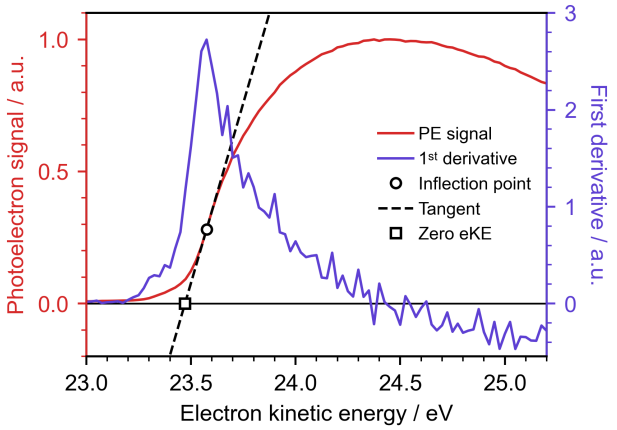

Figure 4.4: Cutoff method: the inflection point of the low eKE tail of a photoelectron spectrum (red) is determined by computing the first derivative of the spectrum (violet). The tangent (dashed line) to the spectrum at the inflection point, i.e. the maximum of the first derivative, (circle) is extrapolated to 0 intensity to determine the 0 eKE point (square).

The −25 V bias exposed the low eKE tail of the spectra, which is characterised by a broad asymmetrical distribution dominated by inelastically scat-

tered electrons. The energy scale of the photoelectron spectra was referenced to the energy of electrons that escape the jet with 0 eV.[42] This was done by extrapolating the tangent going through the inflection point of the rising edge of the low eKE tail to 0 intensity and setting the corresponding x value to 0 eKE, following the procedure described by Thürmer et al.[42] Figure 4.4 shows an example plot describing the procedure.

4.2.3 Ultraviolet photoelectron spectroscopy

Details of the set up and the operation of the UV liquid microjet instrument were described in Chapter 2. In the experiments presented in this chapter, wavelengths between 410 nm (3.02 eV) and 310 nm (4.00 eV) were employed to measure one-colour multiphoton detachment photoelectron spectra of pCE$^-$ in aqueous solutions. A pCE concentration of 50 µM was employed in all measurements except the power dependent measurements, in which 5 µM pCE was employed. This lower concentration ensured that higher laser power could be employed without saturating the detector. Concentrations of NaOH between 1.0 and 3.5 mM were used to ensure full deprotonation of pCE$^-$ and, together with flow rates between 0.50 and 0.95 ml/min, to compensate for the effect of the streaming potential of the liquid microjet.

4.2.4 Molecular dynamics simulations

Following the approach required for the spectral retrieval explained in Chapter 3, molecular dynamics of pCE$^-$ at the water-vacuum interface were carried out to determine its concentration depth profile. Simulations were carried out with the OpenMM package (version 7.7.0).[94] The initial coordinates of pCE$^-$ were optimised using the Automated Topology Builder and Repository[95,96] at the B3LYP/6-31G* level of theory. The SMIRNOFF force field (version 0.11.4)[97] was employed to model the solute surrounded by a Transferable Intermolecular Potential with 3 Points (TIP3P) water environment.[98] A pCE$^-$ molecule and Na^+ ion were placed in a 5×5×9 nm box and surrounded with water molecules. The box was then expanded to 5×5×18 nm to simulate the

liquid-vacuum interface and periodic boundary conditions were applied. This setup results in an infinite series of slabs with a thickness of 9 nm, separated by 9 nm of vacuum. MD simulations were run using Langevin dynamics with LFMiddle discretisation[99] with a heat bath set at 300 K, a 2 fs time step and a friction coefficient of 1 ps^{-1}. Long-range electrostatic interactions were described by the Particle Mesh Ewald (PME) with a 1 nm cutoff. A local energy minimization was performed and the velocities of all the atoms were set to random values chosen from the Boltzmann distribution at 300 K, before the system was allowed to equilibrate for 2 ns. Simulations were run for 120 ns, recording the position of all atoms every 4 ps. Six simulations were carried out. The centre of mass of the solute was used to track its position along the axis perpendicular to the surface.

4.3 Results and Discussion

4.3.1 Steady-state UV-visible absorption

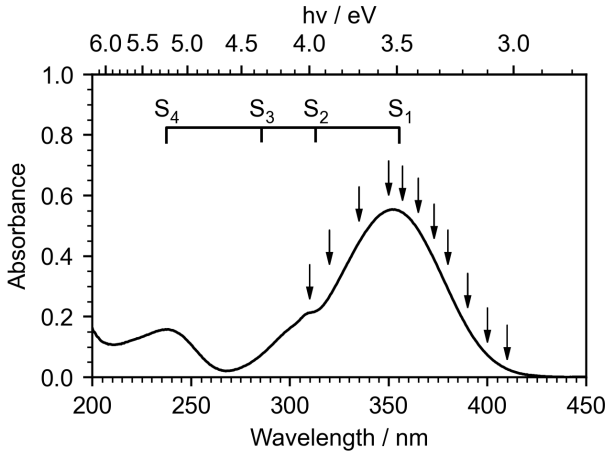

Figure 4.5: UV-visible absorption spectrum of 50 µM pCE$^-$ in water taken as the difference between spectra of 50 µM pCE in 2.0 mM aqueous NaOH and 2.0 mM aqueous NaOH, recorded with a 4 mm path length. Arrows indicate the wavelengths employed in this study and the comb indicates the vertical excitation energies of the first four electronically excited states of aqueous pCE$^-$, calculated at the XMCQDPT2/CASSCF level of theory (Section 4.3.3). These calculations were carried out by Anton Boichenko and Anastasia Bochenkova at the University of Moscow.[141]

Figure 4.5 shows the UV-visible steady-state absorption spectrum 50 µM pCE$^-$ taken as the difference between spectra of 50 µM pCE in 2.0 mM aqueous NaOH, and 2.0 mM aqueous NaOH, recorded with a 4 mm path length. The peak at longer wavelengths has a maximum at 351.5 nm, which is blue-shifted with respect to the absorption maxima in the protein (446 nm)[105] and in vacuum (430 nm).[123,142] The comb marks the first four vertical excitation energies of aqueous pCE$^-$, calculated at the XMCQDPT2/CASSCF level of theory.[141]

4.3.2 Sample composition

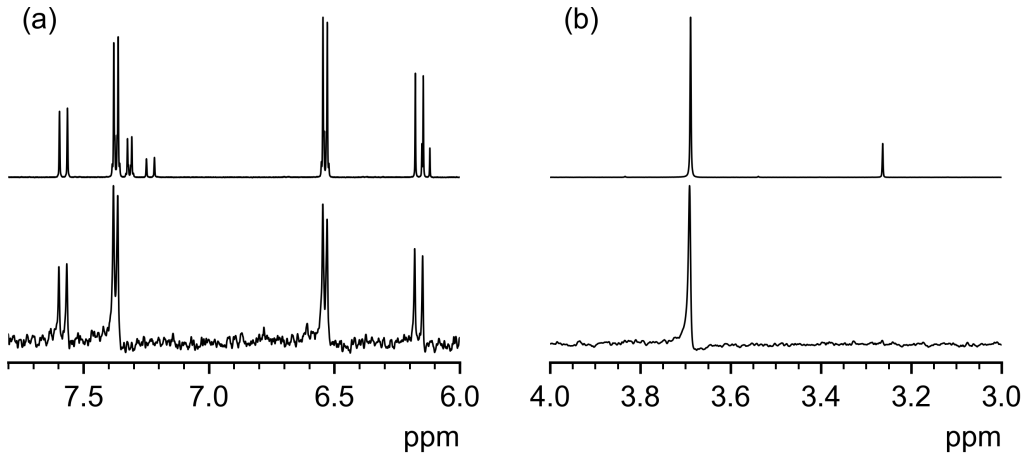

Figure 4.6: NMR spectra of 5.0 mM pCE 5.5 mM NaOD in D_2O (top) and 50 µM pCE 1.25 mM NaOD in D_2O (bottom), plotted between (a) 6.0 and 7.8 ppm, and (b) 3.0 and 4 ppm.

Nuclear magnetic resonance (NMR) spectra of 5.0 mM pCE and 5.5 mM NaOD in D_2O, and 50 µM pCE and 1.25 mM NaOD in D_2O are presented in Figure 4.6 (see Appendix A.1 for the full spectra and assignment). The NMR spectrum of 5.0 mM pCE$^-$ shows extra peaks not present in the spectrum of 50 µM pCE$^-$. These peaks are consistent with the dianion of para-coumaric acid and methanol, indicating that hydrolysis has occurred. The ratio of the NMR signals of the methyl groups of methanol and pCE$^-$ is 0.16:1, and that of the high-ppm vinyl and aromatic protons of the dianion of pCA (pCA^{2-}) and pCE$^-$, which are well separated, is 0.29:1. Due to the low solubility of pCE$^-$,

the solution employed in the EUV experiments was sonicated for ∼2 h, which caused a significant increase in the temperature of the solution. Since lower concentrations were used in the UV experiments, solutions were only sonicated for a maximum of 30 minutes, resulting in little to no hydrolysis of $p\mathrm{CE}^-$.

These results illustrate the there is no noticeable aggregation or hydrolysis in the UV measurements. However, EUV spectra may contain some contribution from the dianion of *p*CA. Similarly, the X-ray spectra of $p\mathrm{CE}^-$ may also contain contribution from $p\mathrm{CA}^{2-}$. However, the solution was sonicated for 30 minutes,[143] which suggests that the contribution from $p\mathrm{CA}^{2-}$ could be minimal.

4.3.3 Electronic structure

The calculations presented here were carried out by Anton Boichenko and Anastasia Bochenkova at the University of Moscow.[141] The first four VEEs and VDEs of $p\mathrm{CE}^-$ in aqueous solution were determined at the XMCQDPT2/CASSCF/PBE0/(aug)-cc-pVDZ level of theory (Figure 4.7). The electronic configurations of the singlet states of the anion and doublet states of the neutral radical are also shown and can be used to infer likely detachment processes based on Koopmans' correlations, e.g., photodetachment from S_1 most likely results in the formation of D_0 and D_3.

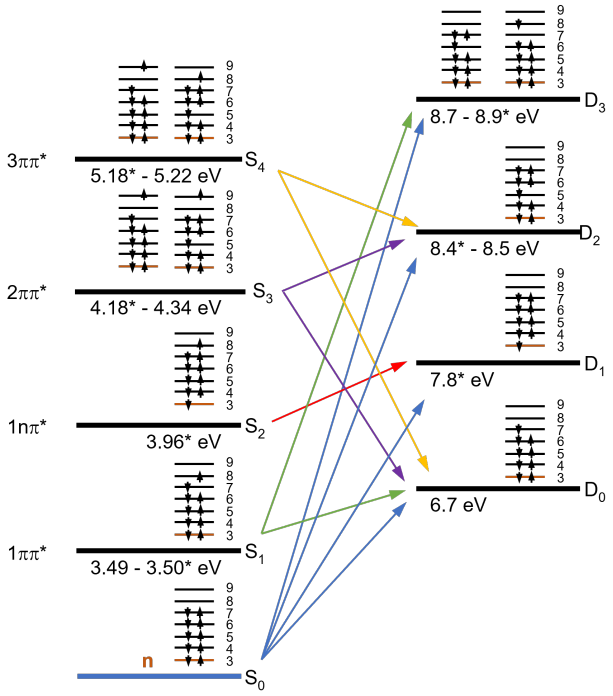

Figure 4.7: First four VEEs and VDEs of *p*CE$^-$ in aqueous solution determined at the XMCQDPT2//CASSCF/PBE0/(aug)-cc-pVDZ level of theory. VEEs and VDEs with an asterisk are calculated using a mixed n/π active space, while the rest are calculated using a pure π active space. The horizontal black and red lines labelled with numbers indicate the π and n orbitals and their occupation in each state, respectively. Arrows indicate likely detachment processes based on the electronic configuration of the states involved. These calculations were carried out by Anton Boichenko and Anastasia Bochenkova at the University of Moscow.[141]

4.3.4 Vertical detachment energies from the ground state

4.3.4.1 X-ray LJ-PES

Figure 4.8 shows the X-ray PES spectrum of 5 mM *p*CE in aqueous solution with 5.5 mM NaOH and 30 mM NaF, recorded with a photon energy of 180 eV. The spectrum was fit as a sum of Gaussians describing photodetachment from *p*CE$^-$ and photoionisation of liquid and gaseous water. The widths of the Gaussians contributing to the liquid water photoelectron signal were kept fixed and their centre positions were fixed relative to the $1b_1$ peak, based on parameters reported in recent accurate measurements of the valence band of

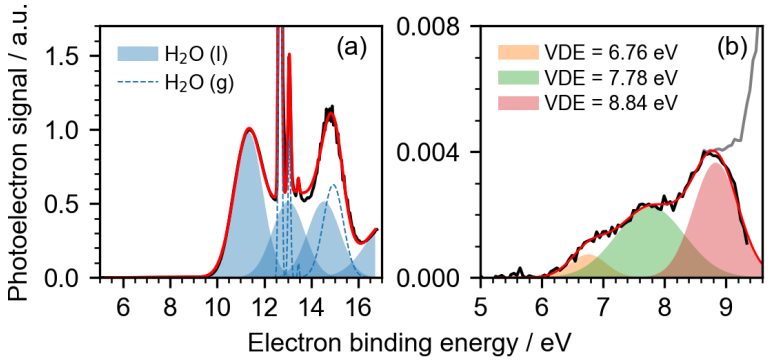

Figure 4.8: X-ray photoelectron spectrum of 5 mM *p*CE in aqueous solution with 5.5 mM NaOH and 30 mM NaF recorded with a photon energy of 180 eV. (a) The spectrum was fit as a sum of Gaussians representing photoionisation of liquid and gaseous water and photodetachment of $p\text{CE}^-$ and a vertical offset to capture the baseline noise. The widths and relative positions of the liquid water Gaussians were constrained to literature values for water.[42,144] The parameters of the gaseous water and $p\text{CE}^-$ Gaussians were not constrained. The eKE was calibrated to the $1b_1$ peak of water which was set to 11.33 eV.[42] (b) Enlarged view of the spectrum in (a) highlighting the contribution of $p\text{CE}^-$ to the photoelectron signal (gray). The water contribution to the spectrum was subtracted and the signal below 9.35 eV (black line) was fit with three Gaussians. Experimental spectrum reproduced from Ref. 138.

water.[42] The energy scale was then calibrated by setting the $1b_1$ central eBE to the accurate eBE value reported in the same study (11.33 ± 0.03 eV).[42] The small signal at eBEs below 9 eV could be fit with four Gaussians. The non-linear least squares fitting procedure was very sensitive to the initial guess parameters, yielding several suitable fits (Appendix A.2). The parameters obtained for the liquid and gaseous water peaks were virtually the same in all fits. Therefore, the difference between the spectrum and the water contribution was fit with three Gaussians below 9.35 eV (Figure 4.8c). Above this value the difference spectrum is dominated by the noise of the signal. The dependence of the centres of the Gaussians on the cutoff is shown in Appendix A.2. Similarly to the analysis performed by Henley,[138] the first two VDEs are quoted in this work using the values obtained from the fit of the subtracted data: 6.76 ± 0.13 eV and 7.78 ± 0.13 eV. Similar values were obtained without constraining the liquid water peaks (Appendix A.2). The position of the red Gaussian

centred at 8.84 ± 0.13 eV was sensitive to the value of the cutoff and cannot be quoted with confidence. Furthermore, signal from OH^- may overlap with the valence band of pCE$^-$, as it has a VDE of 9.2 eV.[32,145]

4.3.4.2 EUV LJ-PES

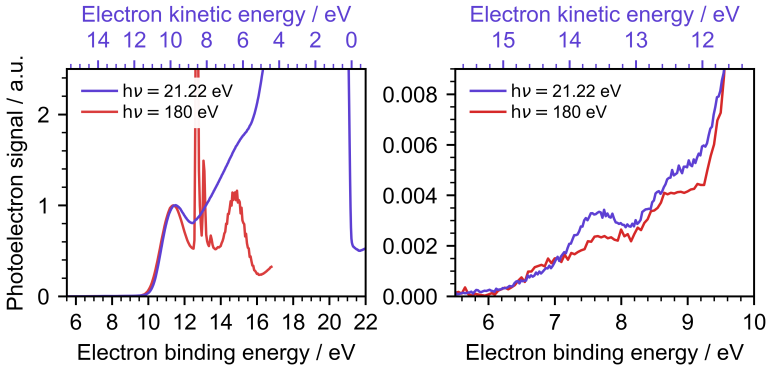

Figure 4.9: EUV photoelectron spectrum of 5 mM pCE in aqueous solution with 5.5 mM NaOH and 50 mM NaCl, recorded with He I α line ($h\nu$ = 21.22 eV, violet) together with the X-ray spectrum of 5 mM pCE in aqueous solution with 5.5 mM NaOH and 30 mM NaF (red) as a function of eBE. The top axis indicates the eKE of the EUV spectrum. The whole spectrum (left) and the zoomed in valence band of pCE$^-$ (right) are shown. The energy scale of the EUV spectrum is referenced to the low-eKE cutoff which corresponds to 0 eKE and the energy scale of the X-ray spectrum was calibrated by setting the $1b_1$ peak of water to 11.33 eV[42] (Section 4.3.4.1).

The valence spectrum of 5 mM pCE in aqueous solution with 5.5 mM NaOH and 50 mM NaCl was recorded with EUV radiation, employing the He I α and He II α emission lines of a helium discharge lamp. The photoelectron spectrum recorded with the He I α line ($h\nu$ = 21.22 eV) is shown in Figure 4.9 together with the X-ray spectrum from Figure 4.8.[138] For the EUV measurements, the liquid jet was biased with −25 V and the energy scale of the spectrum was referenced to the cutoff at low eKE which corresponds to 0 eV. The distribution of unscattered and elastically scattered electrons is on top of a background of inelastically scattered electrons, which is typical of valence spectra with eKEs below 10-14 eV.[71] The spectral shape of the pCE$^-$ signal observed in the X-ray spectrum is partially retained in the He I α spectrum,

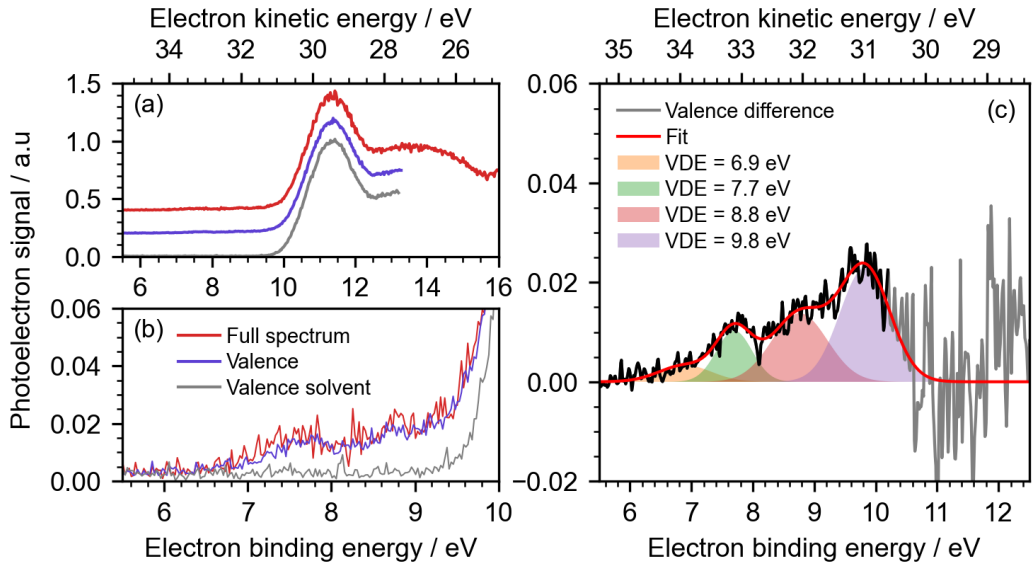

Figure 4.10: EUV photoelectron spectra of 5 mM *p*CE in aqueous solution with 5.5 mM NaOH and 50 mM NaCl, recorded with He II α ($h\nu$ = 40.81 eV). (a, b) Photoelectron spectrum of 5 mM *p*CE in aqueous solution with 5.5 mM NaOH and 50 mM NaCl recorded between 0 and 35 eV (red), photoelectron spectrum of 5 mM *p*CE in aqueous solution with 5.5 mM NaOH and 50 mM NaCl recorded between ∼ 27.6 and 35 eV (violet), and photoelectron spectrum of 50 mM aqueous NaCl recorded between ∼ 27.6 and 35 eV (gray). The spectra in (a) are offset vertically to better highlight their features. (c) Difference between the *p*CE$^-$ spectrum and the NaCl spectrum smoothed with a 12-point quadratic Savitzky-Golay filter (gray) fit with four Gaussians below 10.2 eV (red). The FWHM of the lowest energy peak (orange) was constrained to a maximum of 1 eV and the centre obtained from the fit has a large associated error (0.2 eV).

although accurate VDEs cannot be extracted due to the spectral distortion introduced by the strong vibrational electron scattering in this range and the lack of an accurate description of the inelastic scattering background is available.

Photoelectron spectra of an aqueous solution of 5 mM *p*CE$^-$ in 5.5 mM NaOH and 50 mM NaCl, and an aqueous solution of 50 mM NaCl recorded with the He II α discharge line ($h\nu$ = 40.81 eV) are presented in Figure 4.10a,b. The liquid jet was biased with −25 V. Spectra were recorded both from ∼0 to ∼36 eV eKE to capture the low eKE cutoff and from ∼27 to ∼36 eV focusing on the valence band of *p*CE$^-$ and the $1b_1$ peak of water to reduce collection

times and improve the signal-to-noise ratio. The energy of the full spectrum was calibrated using the cutoff method and the energy of the valence band spectra was calibrated by overlaying the signal of the $1b_1$ peak of water with the same signal in the full spectrum.

As the eKEs measured with the He II α line are higher than ∼15 eV, the valence signal is essentially free from distortion caused by inelastic scattering.[71] The valence spectrum of 50 mM NaCl was subtracted from the *p*CE$^-$ spectrum and the difference was fit with four Gaussians (Figure 4.10c). The FWHM of the lowest energy peak was constrained to a maximum of 1 eV and a large error (0.2 eV) is associated with the centre. Without constraining the fit, the two lowest energy Gaussians have the same eBE (∼7.7 eV) and a FWHM of 2 eV and 0.2 eV. These values are inconsistent with typical FWHM of organic solutes in water and it is unlikely that two states of the neutral radical derived from *p*CE$^-$ have the same energy but different associated FWHM.

The centres of the first three peaks obtained in the fit are 6.9±0.2, 7.7±0.1 and 8.8 ± 0.1 eV, which agree remarkably well with those of the subtracted X-ray data (6.76 ± 0.13, 7.78 ± 0.13 and 8.84 ± 0.13 eV, Figure 4.8). A peak at 9.8 eV is present in the He II α spectrum that is not observed in the X-ray spectrum that cannot be assigned. A possible explanation is that there are overlapping contributions from OH$^-$ (VDE= 9.2 eV)[32,145] and higher VDEs of *p*CE$^-$.

Interestingly, the intensity of the *p*CE$^-$ signal relative to the $1b_1$ peak of liquid water recorded with the He II α line is around 5 times larger than the same signal in the X-ray spectrum (Figure 4.10c and Figure 4.8). A possible explanation is that *p*CE$^-$ and water exhibit different detachment and ionisation cross sections as a function photon energy. Alternatively, this may be indicative of an enhanced concentration of *p*CE$^-$ at the surface and a low probing depth at these eKEs, as the experimentally derived EAL of electrons in water increases monotonically for eKEs above ∼20 eV.[47,48] The *p*CE$^-$ signal intensity in the He I α spectrum has the same order of magnitude as in the X-ray spectrum.

The EAL at eKEs around 10 eV has a larger variation than at higher eKEs,[48] making predictions on the probing depth less reliable.

4.3.4.3 UV LJ-PES

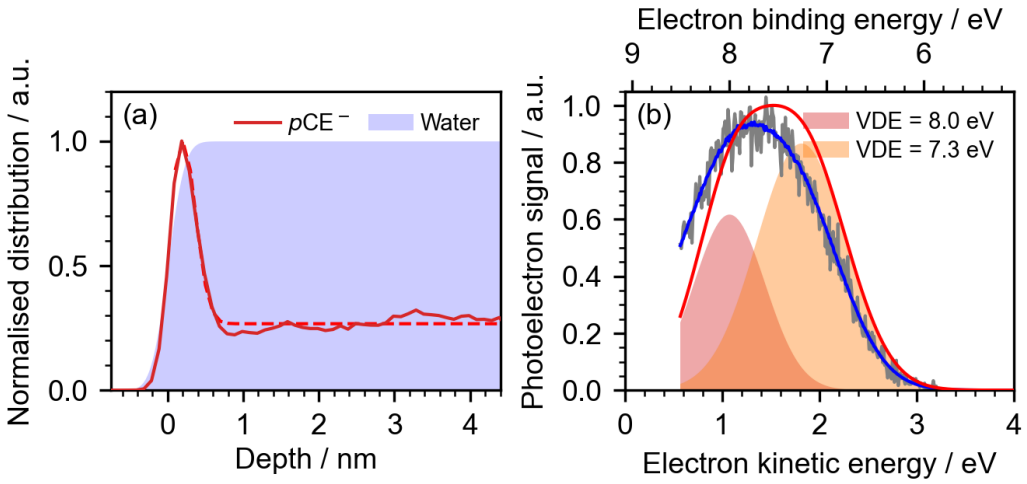

Figure 4.11: (a) Normalised concentration depth profile of pCE$^-$ in aqueous solution near the liquid-vacuum interface, determined from molecular dynamics simulations. The centre of mass of pCE$^-$ was used to track its position along the axis normal to the surface. The blue shaded area is the cumulative normal distribution fit to the distribution of the oxygen atoms of the water molecules and normalised to 1. The dashed line indicates the concentration depth profile employed in the retrieval of the pCE$^-$ spectra. (b) 410 nm (3.02 eV) spectrum of 50 µM pCE in 1.0 mM aqeuous NaOH. The spectrum was fit as a sum of two surface Gaussians (filled) with LJscatter. The blue line is the fit to the data, and the red line is the retrieved spectrum.

Efforts were also made to determine the VDEs of pCE$^-$ using UV femtosecond laser pulses at UCL, by recording the photoelectron spectrum of pCE$^-$ with a wavelength that is non-resonant with excited states of pCE$^-$. However, since pCE$^-$ has a significant absorption cross section in aqueous solution at wavelengths below around 400 nm, non-resonant processes require at least three photons. A consequence of this is that two-photon resonances make non-resonant one-colour multiphoton detachment PES impossible, since pCE$^-$ absorbs light at wavelengths above 200 nm (Figure 4.5).

The photoelectron spectrum of 50 µM pCE in 1.0 mM aqueous NaOH recorded with 410 nm is presented in Figure 4.11b. A concentration of pCE$^-$

100 times smaller than in the X-ray and EUV experiments was employed with improved signal-to-noise ratio. This is due to a lack of solvent background, as photoionisation of water would require four photons of 410 nm. In order to determine the concentration depth profile of $p\text{CE}^-$ needed for the retrieval of the true UV photoelectron spectra of $p\text{CE}^-$ with LJscatter (Chapter 3), molecular dynamics (MD) simulations at the liquid-vacuum interface were carried out (Figure 4.11a). A histogram of the positions of $p\text{CE}^-$ as a function of depth was extracted, and $p\text{CE}^-$ was found to have an enhanced surface concentration compared to the bulk. The concentration depth profile was modelled as a sum of a Gaussian centred 0.2 nm below the surface with a FWHM of 0.4 nm and a vertical offset. The ratio between the height of the Gaussian and the offset was taken as 2.75. This function was employed to fit the 410 nm spectrum with LJscatter. Due to the slightly poorer signal-to-noise ratio of the 410 nm spectrum of $p\text{CE}^-$ compared to the spectra employed to benchmark the retrieval software in Chapter 3, the data were binned in 0.01 eV steps rather than interpolated onto a 0.01 eV grid. This approach ensures that all measured signal is retained, instead of only the values closest to the grid points. Two surface Gaussians were fit and VDEs of 7.3 ± 0.1 eV and 8.0 ± 0.1 eV were obtained.

4.3.4.4 Summary of vertical detachment energies

Table 4.1: S_0-D_0 and S_0-D_1 VDEs and corresponding eKEs of aqueous $p\text{CE}^-$ determined using X-ray and EUV LJ-PES. Calculated VDEs obtained with XMCQDPT2/CASSCF.[141] For comparison, the experimental S_0-D_0 VDE of isolated $p\text{CE}^-$ is included.[120] All values are in eV.

	X-ray LJ-PES	EUV LJ-PES	Calculated	Gas-phase PES[120]
$h\nu$	180	40.81	-	3.58-4.00
S_0-D_0 eKE	173.24 ± 0.13	33.9 ± 0.2	-	-
S_0-D_0 VDE	6.76 ± 0.13	6.9 ± 0.2	6.7	2.85 ± 0.05
S_0-D_1 eKE	172.22 ± 0.13	33.1 ± 0.1	-	-
S_0-D_1 VDE	7.78 ± 0.13	7.7 ± 0.1	7.8	-

Table 4.1 summarises the experimental and calculated VDEs of aqueous $p\text{CE}^-$ and the experimental value for the VDE of gas-phase $p\text{CE}^-$.[120] Upon solvation, the VDE of $p\text{CE}^-$ is blue-shifted by more than 4 eV, due to the stabilising

effect of water on the negative charge of the anion. The experimental values for the S_0-D_0 and S_0-D_1 VDEs obtained with X-ray and EUV LJ-PES are in excellent agreement with each other and with the calculated VDEs. The VDEs determined with 410 nm laser pulses are 0.4 and 0.3 eV higher, due to the presence of one and two-photon resonances of pCE$^-$. A discussion of the phenomena behind this is presented in Section 4.3.6. In the rest of this chapter, values from the X-ray data are reported to one significant figure of the associated error, i.e. 6.8 ± 0.1 and 7.8 ± 0.1 eV.

4.3.5 Adiabatic detachment energies from the ground state

Photoelectron spectra can be employed to approximate adiabatic detachment energies, by extracting the eBE of the onset of the photoelectron signal. A common procedure involves fitting straight lines to the rising edge of the signal and the noise baseline in log space.[61,65] Figure 4.12 shows this procedure for the photoelectron spectra of pCE$^-$ recorded with X-ray (180 eV, top), EUV (40.81 eV, middle) and UV (3.02 eV, bottom) radiation. The values obtained are between 5.8 and 5.9 eV, in excellent agreement with one another. The reorganisation energy of pCE$^-$ is thus estimated as $\sim$0.9 eV. This demonstrates that despite the presence of two-photon resonances, estimated ADEs can be extracted from the 410 nm spectrum. More generally, it means that UV LJ-PES can be used to determine ADEs, even when the presence of resonances prevents VDEs from the ground electronic state being determined accurately.

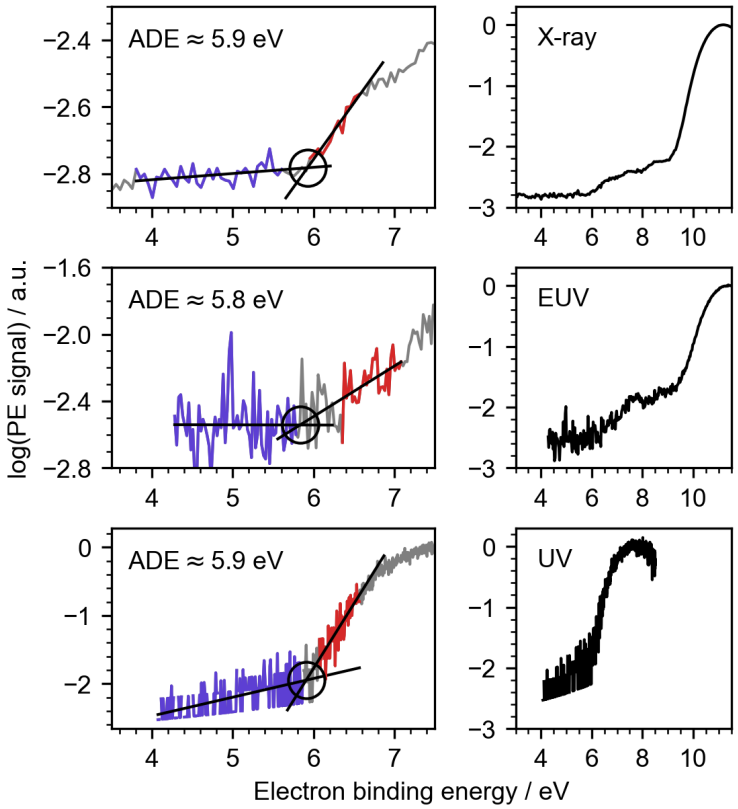

Figure 4.12: Adiabatic detachment energies of pCE$^-$ determined by fitting straight lines to the log signals of the baseline noise and the rising edge of the photoelectron spectra of pCE$^-$ measured with X-ray (180 eV, top), EUV (40.81 eV, middle) and UV (3.02 eV, bottom) radiation. The UV spectrum is plotted as $3h\nu - \text{eKE}$. Plots on the left highlight the area of the plots employed in the fits. Plots on the right show the spectra plotted between 3.0 and 11.5 eV.

4.3.6 Vertical detachment energies from electronically excited states

Figure 4.13 shows the photoelectron spectrum of pCE$^-$ recorded with 350.0 nm, which is approximately at the absorption maximum of pCE$^-$ in aqueous solution (see Figure 4.5). The spectrum was fit with a sum of three distorted surface Gaussians, indicating that three distinct photodetachment processes are present. Based on the electronic structure calculations presented in Section 4.3.3, direct photodetachment via the S_1 state of pCE$^-$ is most likely to form the neutral radical in its ground (D_0) and third excited (D_3) states. As a first approximation, photodetachment to form D_0 is expected to be a two pho-

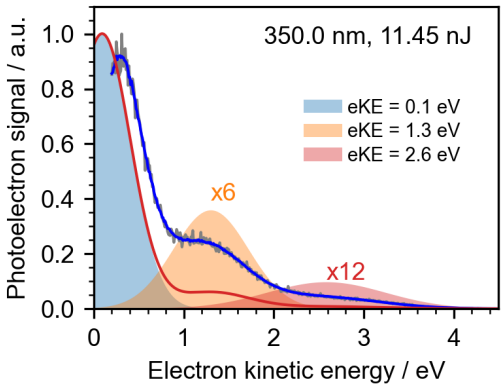

Figure 4.13: 350 nm spectrum of 5 µM *p*CE in 2.0 mM aqueous NaOH recorded with a pulse energy of 11.45 nJ (gray). The spectrum was fit as a sum of 3 surface Gaussians (filled) with LJscatter. The blue line is the fit to the data, and the red line is the retrieved spectrum, which is given by the sum of the filled Gaussians.

ton process as the first VDE is around the energy of 2 photons ($2h\nu = 7.08$ eV), while photodetachment to form D_3 is expected to be a three photon process as the calculated VDE has a value of 8.7-8.9 eV, which would result in an eKE between 1.7 and 1.9 eV. In principle, the third process could be due to ionisation of the solvent. However, solvent-only measurements taken at similar and higher laser powers yielded no photoelectron signal, indicating that all features arise from photodetachment of $p\text{CE}^-$. Therefore, in order to the elucidate the nature of the detachment processes involved, the dependence of the photoelectron signal of $p\text{CE}^-$ on the power and wavelength of the laser pulse was investigated.

The transition probability W for off-resonance N-photon ionization or detachment of a molecule[146] follows the relationship

$$W^{(N)} = \hat{\sigma}_N I^N \tag{4.1}$$

where I is the photon flux, and $\hat{\sigma}_N$ is the total generalized cross section which depends on the number of photons, photon energy, the energy of the outgoing electron, and the nature and energy of the states involved. Therefore, the change in signal intensity as a function of laser power can be employed to

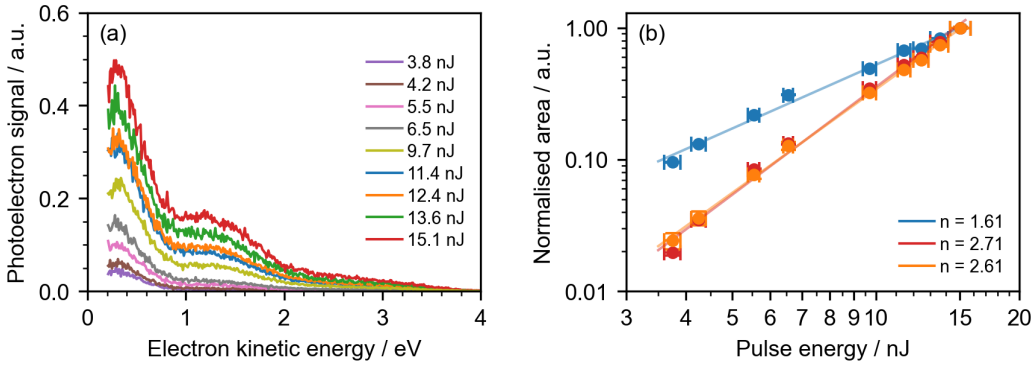

Figure 4.14: (a) 350 nm spectra of 5 µM *p*CE in 2.0 mM aqueous NaOH recorded with different pulse energies. The spectra were fit with LJscatter keeping the width and centre of the Gaussians fixed. (b) Log-log plot of the peak area of the retrieved Gaussians normalised to their intensity at the highest pulse energy as a function of pulse energy for the three peaks. Blue, red and orange circles represent the area of the low, middle and high eKE peaks. Solid lines are the linear fits of the log of the peak area and pulse energy.

identify the number of photons involved in photodetachment processes.

Figure 4.14b shows the dependence of the peak area of the three features present in the 350 nm photoelectron spectrum of $p\text{CE}^-$ on the energy of the laser pulses plotted on a log-log scale. The peak areas were obtained by fitting three surface Gaussians to the photoelectron spectra of $p\text{CE}^-$ recorded at 350 nm with different powers. The centre and FWHM of the peaks were fixed to those in the fit in Figure 4.13. Slopes of 1.61±0.06, 2.71±0.09 and 2.63±0.07 were obtained by fitting straight lines to the data in Figure 4.14b, suggesting that the low energy peak arises from a two-photon process and the two higher energy peaks arise from a three-photon process. The deviation from integer values is likely due to the fact that photodetachment occurs via resonances and there are different transition probabilities for absorption and detachment.[146]

Figure 4.15 shows photoelectron spectra of $p\text{CE}^-$ recorded with wavelengths between 400 nm and 310 nm. The spectra were fit with distorted surface Gaussians using the spectral retrieval code. The 400 nm spectrum was fit with two Gaussians; the 380, 365 and 350 nm spectra were fit with three Gaussians; and the 310 nm spectrum was fit with one Gaussian. Although

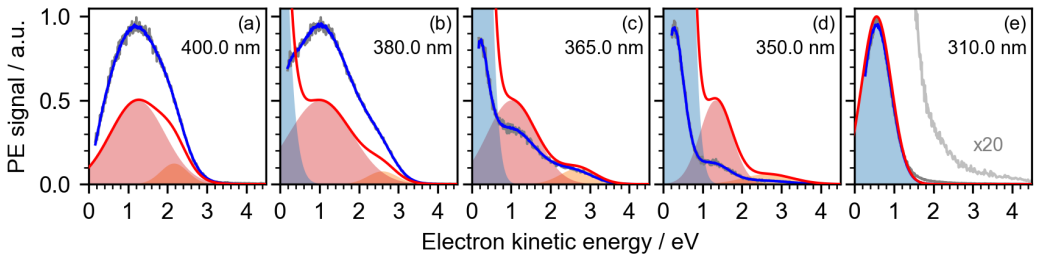

Figure 4.15: Photoelectron spectra of $p\text{CE}^-$ recorded with different wavelengths (gray). The (a) 400 nm spectrum was of 50 µM *p*CE in 3.5 mM aqueous NaOH and was fit with two surface Gaussians using LJscatter. The (b) 380 nm, (c) 365 nm and (d) 350 nm spectra were of 50 µM *p*CE in 1.0 mM aqueous NaOH and were fit with three surface Gaussians. The (e) 310 nm spectra was of a 50 µM *p*CE in 2.0 mM aqueous NaOH and was fit with a surface Gaussian. Blue lines are the fit to the data and red lines are the retrieved spectra.

the 310 nm spectrum also has a small contribution on the high eKE side of the main peak (magnified 20 times in Figure 4.15e), which qualitatively corresponds to the red and orange peaks present in the other spectra, the low intensity of these features rendered the fitting unreliable. While the red and orange higher energy peaks are present in all spectra, the blue low energy peak is not observed at 400 nm and its contribution increases as wavelength decreases. The blue peak dominates the spectrum at 310 nm. This suggests that it is a near-threshold process and the peak is revealed as the total photon energy becomes higher than the VDE.

In order to capture the changes in the eKE of the red and orange peaks as a function of photon energy, additional photoelectron spectra of $p\text{CE}^-$ were measured at wavelengths between 400 and 310 nm. The spectra were recorded at a later date than the data in Figure 4.15 at a time when the collection efficiency of the instrument was slightly worse, which is why the data are cut off at a slightly higher eKE (0.53 eV compared to 0.34-0.44 eV). The data were retrieved using LJscatter, as shown in Figure 4.16. Similarly to the 310 nm data presented in Figure 4.15, the 320 nm and 310 nm spectra could not be fit with three Gaussians due to the low signal-to-noise and overlap of the high eKE features. As the processes giving rise to the two higher eKE peaks require

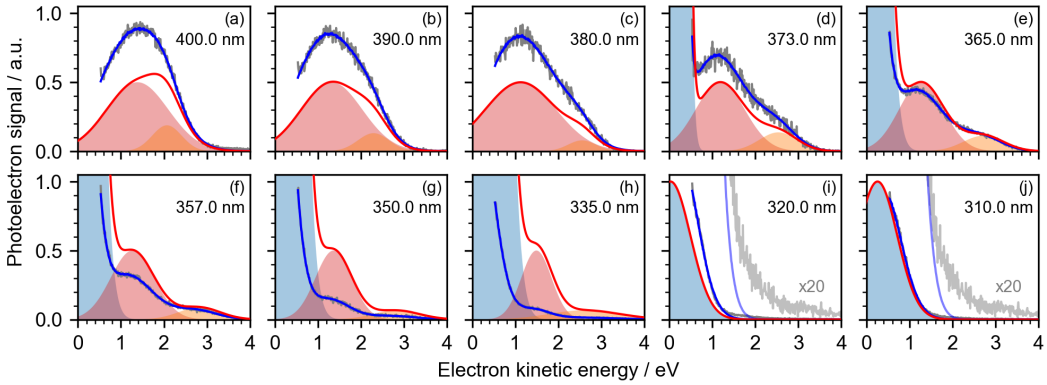

Figure 4.16: Photoelectron spectra of a 50 µM *p*CE 1.0 mM NaOH solution recorded with different wavelengths (gray). The spectra in (a-c) were fit with two surface Gaussians. The spectra in (c-h) were fit with three surface Gaussians. The spectra in (i, j) were fit with one surface Gaussian. Blue lines are the fit to the data and red lines are the retrieved spectra.

more than one photon after excitation to S_1, plotting their central eKE as a function of photon energy can provide valuable information about the states involved in the detachment process (Figure 4.17). Here, the data from Figure 4.15 are shown as empty circles, and the data from Figure 4.16 together with the data from the 410 nm spectrum in Figure 4.11 are shown as full circles.

The central eKE of the red peak remains approximately constant with

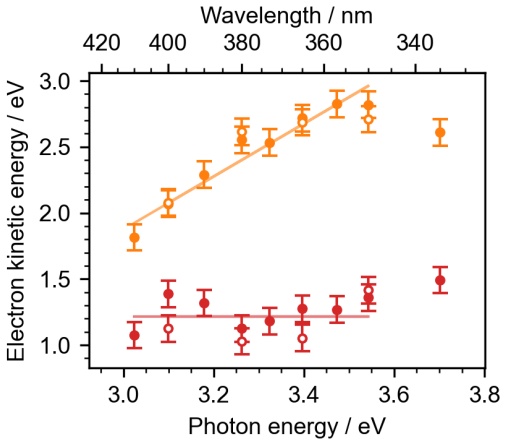

Figure 4.17: Central eKE of the high (orange) and middle (red) eKE peaks of the photoelectron spectra of $p\mathrm{CE}^-$ between 410 nm and 335 nm as a function of photon energy $h\nu$. Full and empty circles are data obtained from the fits in Figure 4.16 and Figure 4.15, respectively. The red and orange straight lines have slopes of 0 and 2, respectively

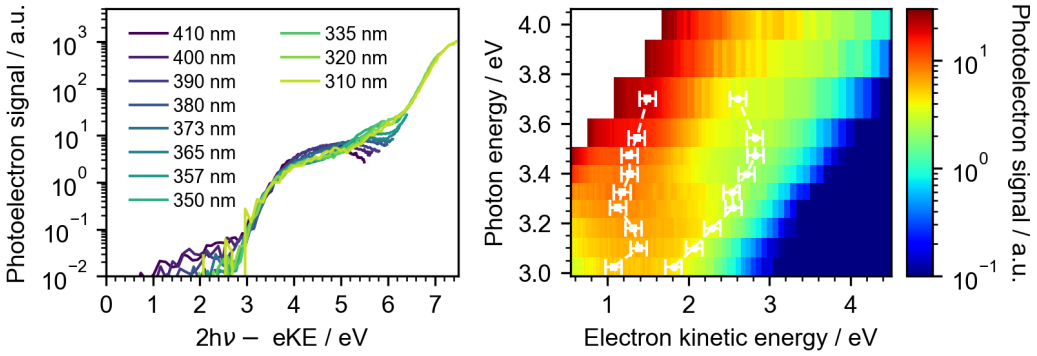

Figure 4.18: Photoelectron spectra of a 50 µM *p*CE in 1.0 mM NaOH solutions recorded with wavelengths between 410 and 310 nm. Left: The photoelectron spectra were plotted as a function of $2h\nu - \text{eKE}$ and scaled to align the rising edge. Right: Heat map of the scaled photoelectron spectra plotted as a function of eKE and photon energy. The contribution from signal above 30 in the left panel is not shown in the heatmap to highlight the shift in the two high eKE peaks. The spectra recorded with wavelengths below 380 nm were fit with two surface Gaussians, and the spectra recorded with wavelengths between 373 and 335 nm were fit with three surface Gaussians. The 320 and 310 nm spectra have a small relative contribution of the two higher eKE peaks compared to the low eKE rendering reliable fitting of the high eKE features infeasible. The white scatter points represent the centres of the retrieved peaks.

photon energy for photon energies below ∼3.6 eV. Conversely, the central eKE of the orange peak increases at a rate of about 2 with photon energy. This behaviour is represented visually in the right panel of Figure 4.18, which presents a heatmap in which the photoelectron spectra are normalised to the falling edge at high eKEs and plotted as a function of eKE and photon energy.

In the gas phase, molecular anions that do not experience large geometry changes upon photodetachment have a propensity to conserve vibrational energy.[147] This behaviour was observed for isolated *p*CE$^-$ using anion photoelectron spectroscopy,[120] and would hold true for *p*CE$^-$ in solution if solvent relaxation is slower than the instrument response function (∼300 fs). The trend of the eKE of the orange peaks supports this idea: the vibrational energy gained upon excitation to S_1 is conserved upon detachment, since the measured eBE of S_1 ($2h\nu$ − eKE) is independent of photon energy (Figure 4.19a), with an average value of 4.1 ± 0.1 eV. The corresponding $3h\nu$ − eKE

values range from 7.2 to 7.9 eV and are consistent with the formation of hot D_0, as the non-resonant VDE is 6.8 ± 0.1 eV (Section 4.3.4.4). The constant eKE of the red peak as a function of photon energy indicates the presence of a resonance embedded in the detachment continuum S_n from which indirect detachment occurs (Figure 4.19b), and represents the gap between S_n and the resulting neutral radical state D_m.

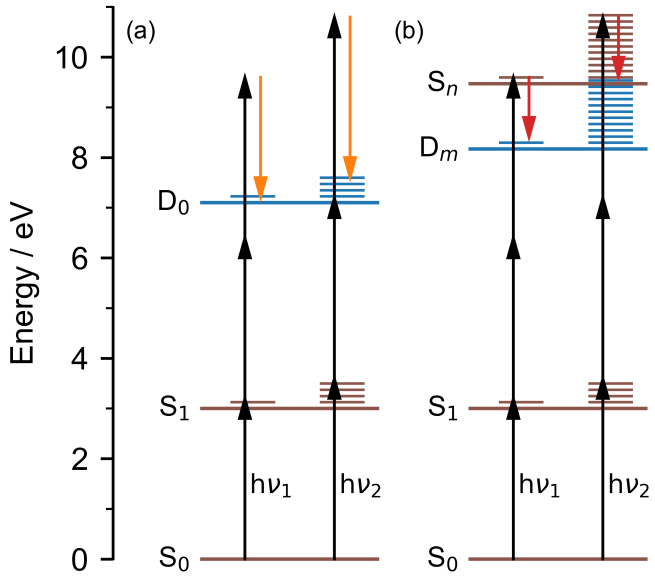

Figure 4.19: Scheme highlighting the processes that give rise to the high (left) and middle (right) eKE peaks of the spectra recorded with wavelength resonant with S_1. (a) Direct detachment: the vibrational energy of S_1 is conserved upon detachment. eKE increases linearly with the energy of two photons. (b) Indirect detachment: the vibrational energy of S_n above the detachment threshold is conserved upon detachment. eKE is independent of photon energy.

In the absence of resonances, the average eBE of S_1 represents the difference between the adiabatic detachment energy (ADE) of D_0 and the adiabatic excitation energy (AEE) of S_1. The ADE can be approximated as

$$\mathrm{ADE} \approx nh\nu - \mathrm{eKE} - (h\nu - \mathrm{AEE}) \tag{4.2}$$

which can be rearranged for $n = 3$ to give

$$\text{ADE} - \text{AEE} = 2h\nu - \text{eKE}. \tag{4.3}$$

An estimate for the ADE was obtained in Section 4.3.5 (ADE ≈ 5.9 eV). Using Equation 4.3 and $2h\nu - \text{eKE} = 4.1$ eV, the AEE would have a value of ∼1.8 eV. However, this value is unlikely as the maximum of the fluorescence spectrum is ∼2.7 eV (Figure 4.20a), which roughly corresponds to the vertical emission energy from S_1. As the vertical emission energy is likely to be smaller than the AEE (Figure 4.20b), this suggests that a higher-lying two-photon resonance may be present.

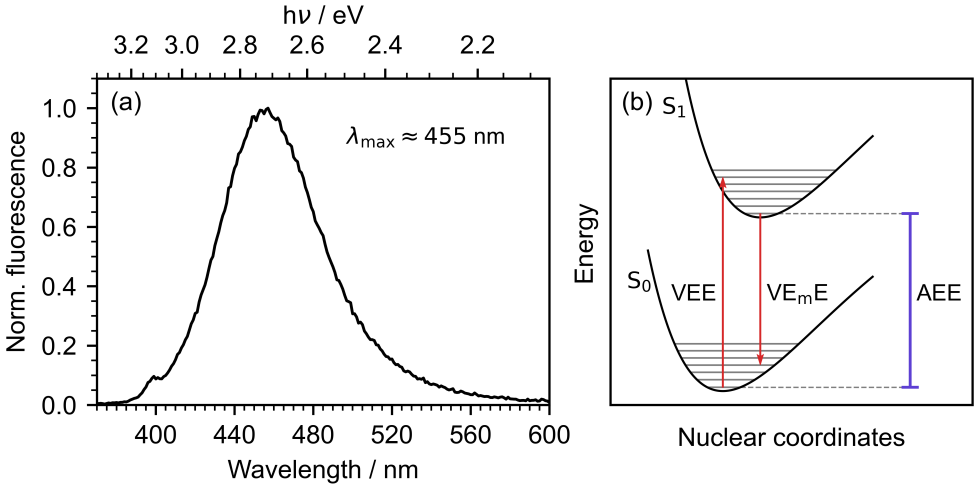

Figure 4.20: (a) Normalised fluorescence spectrum of 50 µM *p*CE in 2.0 mM aqueous NaOH after excitation at 350 nm. The peak maximum is at ∼455 nm (∼2.72 eV). (b) Diagram outlining the difference between vertical excitation energy (VEE), vertical emission energy (VE_mE) and adiabatic excitation energy (AEE).

As the S_1-D_0 VDE cannot be confidently determined from the three-photon detachment processes via S_1, the blue peak in the spectra of Figures 4.15 and 4.16 is considered here. Due to the eKE of the blue peak being ∼0 eV in all spectra, an accurate eKE value could only be obtained from the 310 nm spectrum presented in Figure 4.15, with a $h\nu - \text{eKE}$ value of 3.4 ± 0.1 eV. In Chapter 5, a two-colour photoelectron spectrum was recorded following excitation to S_1 with 350 nm, and detachment with 266.7 nm. The photoelectron

distribution is shifted to higher eKEs because the total photon energy is higher, thus providing the more accurate value 3.7 ± 0.1 eV, which is 0.3 eV higher than the value from the 310 nm spectrum. This difference could be due to competition between excitation to S_1 and S_2. Although some computational studies have calculated the oscillator strength of S_2 with $n\pi^*$ character to be near-zero,[119,121,148] UV-visible spectra of other derivatives of pCA$^-$ (i.e., the dianion of pCA, the amide and the phenyl thioester) show a band centred at around 310 nm in ethylene glycol, while the most intense band had a peak at 340, 350 and 400 nm, respectively.[132] The 310 nm bands underwent a smaller solvatochromic shift in ethylene glycol and dimethylformamide solutions and the anisotropy of the fluorescence of the chromophore following excitation at different wavelengths also decreased rapidly at excitation wavelengths shorter than ∼320 nm, suggesting the presence of a different electronic state with a different polarisation direction. Furthermore, the 310 nm band lacks a corresponding emission counterpart in the fluorescence spectrum of pCE$^-$ (Figure 4.20).

Therefore, the spectrum at 310 nm may contain contributions from detachment from S_2 as well as S_1. Based on Koopmans' correlations, detachment from S_2 is expected to form the neutral radical in its first excited state (D_1). The decrease in $h\nu -$ eKE between the 350 nm and 310 nm spectrum could be attributed to overlap between signals from these two channels, and the S_2-D_1 ADE being smaller than the S_1-D_0 ADE.

In the 335 nm spectrum (Figure 4.16h), the positions of the red and orange peaks, which correspond to detachment from S_1, deviate from the trend observed at wavelengths shorter than 350 nm. Furthermore, the one-photon eBE of the blue peak obtained from the two-colour spectrum in Chapter 5 after excitation at 350 nm (3.7 ± 0.1 eV) is about 0.4 eV smaller than the average two-photon eBE of the orange peak (4.1 ± 0.1 eV), despite both originating from S_1-D_0 detachment. Transient absorption experiments of pCE$^-$ and PYP in solution[114,133] have reported the formation of solvated electrons as a conse-

quence of the absorption of two pump photons. This process was identified by the quadratic dependence of the solvated electron signal on the pulse energy of the exciting laser. Since both pCE$^-$ and PYP have an excited state absorption near S_0-S_1 absorption maximum,[114,133,134] TAS measurements suggested that solvated electrons originate from a high-lying state near the detachment continuum. In the present PES measurements, excitation to this state could result in a different overlap with D_0, thereby influencing the amount of vibrational energy conserved upon detachment and the observed eKE. Consequently, the three-photon detachment to D_0 could proceed via a sequential mechanism: initial excitation to S_1, followed by further excitation to a high-lying state near the detachment continuum and, finally, detachment to D_0.

4.4 Conclusions and outlook

The first two vertical detachment energies of the model photoactive yellow protein chromophore pCE$^-$ have been determined using X-ray and EUV liquid-microjet photoelectron spectroscopy. VDEs of 6.8 ± 0.1 eV and 7.8 ± 0.1 eV were obtained, in excellent agreement with values calculated with XMC-QDPT2/CASSCF (6.7 and 7.8 eV). The onsets of the X-ray, EUV and UV photoelectron spectra were employed to determine the first ADE of pCE$^-$ to be $\sim$5.9 eV.

The photodetachment pathways of pCE$^-$ following excitation to its first excited state were investigated with UV LJ-PES across a wavelength range of 410 nm to 310 nm. Power-dependent measurements were employed to distinguish between one and two photon detachment channels and wavelength-dependent measurements disentangled the role of two distinct two-photon detachment mechanisms from S_1. The first involves direct detachment via a high-lying excited state near the detachment continuum, previously implicated in the formation of solvated electrons. The presence of this high-lying resonance was inferred from the difference between the one-photon and two-photon eBEs of S_1 and the change in slope of the eKE of the two-photon channel as a func-

tion of photon energy. The second two-photon process entails autodetachment from a high-lying excited state embedded within the continuum. While such resonances above the detachment threshold are commonly observed in isolated anions due to their low detachment energies, this work provides the first experimental evidence for their presence in solution, offering new insight into the electronic structure of anions in solvated environments.

In addition to improving our understanding of the electronic strucutre of aqueous $p\mathrm{CE}^-$, these measurements provide a strong platform for the TRPES study of $p\mathrm{CE}^-$ presented in Chapter 5, providing the necessary context for the investigation of its photochemical pathways.

Chapter 5

Time-resolved photoelectron spectroscopy of the photoactive yellow protein chromophore in aqueous solution

The photocycle of the photoactive yellow protein (PYP) begins with photoinduced *trans-cis* isomerisation around the double bond of its chromophore, *para*-coumaric acid. To better understand the inherent photophysics of the chromophore and the effect of the environment around it, extensive efforts have been made to investigate its excited state dynamics in the gas phase and in solution, free from the protein environment. In these environments, model PYP chromophores can access an additional decay channel involving rotation around the single bond adjacent to the double bond via a phenolate-twisted geometry, resulting in no net *cis* isomer. While numerous studies have explored the effect of substitution at the carbonyl tail, the effect of bond rotations, and the effect of solvent properties on the chromophore, the role of solvent response remains comparatively underexplored. In this chapter, UV-pump UV-probe time-resolved liquid-microjet photoelectron spectroscopy is employed to investigate the excited state dynamics of the methyl-ester analogue of the PYP chromophore (pCE$^-$) near the liquid-vacuum interface. This study reveals

that pCE$^-$ decays via a single channel involving two transient configurations, consistent with the initially excited state and either solvent relaxation or torsion around the single bond. This work sheds new light on the role of the solvation environment in shaping the ultrafast photophysical pathways of the PYP chromophore.

5.1 Introduction

5.1.1 The photoactive yellow protein

The photoactive yellow protein (PYP) is responsible for the negative phototactic response of the *Halorhodospira halophila* bacterium.[149] Due to its small size, ease of production, and ease of crystallisation,[150] it is a popular model system for the study of biological photoreceptors.[105,151,152] The photocycle of PYP (Figure 4.2 in Chapter 4) is initiated by the absorption of a photon of blue light by the anionic form of *trans-para*-coumaric acid (pCA$^-$), which is bound to a cysteine residue of PYP via a thioester link and is stabilised by a network of hydrogen bonds. pCA$^-$ undergoes torsion around its double bond in the excited state and decays within 100s of femtoseconds to a few picoseconds via a conical intersection with the ground state.[153] This ultimately leads to the formation of a red-shifted intermediate, pR, associated with the *cis* isomer in the ground electronic state. Subsequently, a series of thermal reactions lead to protonation of pCA$^-$ by a glutamic acid residue at the phenolate moiety on a microsecond timescale,[154] inducing structural changes and partial unfolding of the protein.[155,156] This blue-shifted pB state is believed to be responsible for signalling the cell of the presence of potentially harmful blue light.[157] pCA is then deprotonated and undergoes *cis-trans* isomerisation on millisecond to second timescales, recovering the ground state and completing the photocycle.[158]

5.1.2 Early steps of the photocycle

The early steps of the photocycle involve the evolution of the chromophore on the potential energy surface of its first excited state, ultimately leading

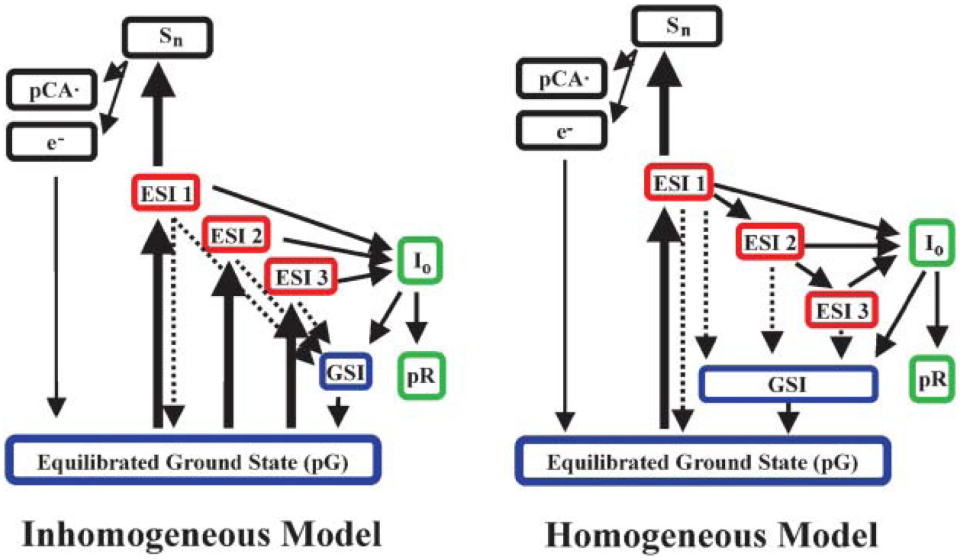

Figure 5.1: Inhomogeneous and homogeneous kinetic models employed in the global analysis of transient absorption data of PYP. pG is the equilibrium ground state, ESI indicates excited state intermediates, S_n is a higher-lying excited state, GSI indicates the ground state intermediates, I_0 and pR are ground state *cis* intermediates. Reprinted from Larsen, D. S., van Stokkum, I. H., Vengris, M., van der Horst, M. A., de Weerd, F. L., Hellingwerf, K. J., van Grondelle, R., *Biophys. J.* **2004**, *87*, 1858–1872. Copyright 2004, with permission from Elsevier.

to a conical intersection with the ground state and the formation of the *cis* intermediate. Time-resolved transient absorption[111,113,159] and fluorescence upconversion[160] experiments of aqueous and crystallised PYP revealed that the relaxation of S_1 is multiexponential, with three components (∼0.5-1.2 ps, ∼2–3 ps, and ∼14-40 ps). Of the population relaxing through the two fastest components, approximately 20-40% proceeds to form the *cis* isomer, whereas the remaining population decays via a highly vibrationally excited electronic ground state intermediate to the *trans* conformer.[159] The overall quantum yield for isomerisation, considering all components, is about 10-20%.[113,159]

Homogeneous and inhomogeneous kinetic models have been employed to explain the multiexponential decay of $p\mathrm{CA}^-$ after photoexcitation. Figure 5.1 shows an example of these two models,[111] although minor modifications have been proposed in different studies, such as the presence of multiple ground state intermediates.[110,112,114,159] The inhomogeneous model attributes the mul-

tiexponential behaviour to the presence of conformational heterogeneity in the ground state. This heterogeneity is preserved upon excitation, resulting in the three timescales associated with the decay of S_1 (Figure 5.1 left).[111,158,159] The homogenous model attributes the multiexponential behaviour to vibrational cooling and the presence of three excited state intermediates (Figure 5.1 right).[111,158,159]

While earlier time-resolved crystallography experiments largely focused on the intermediates of the photocycle formed after the formation of the *cis* isomer with time resolutions larger than 100 ps,[106,161,162] recent advances in free electron laser technology have allowed crystallographic measurements of the excited state of pCA$^-$ in the protein on the femtosecond timescale.[108] Pande et al. observed a structural transition from the *trans* to the *cis* conformations at around 550 fs after excitation,[108] associated with passage through the conical intersection between the excited and ground state potential energy surfaces, in excellent agreement with the dominant ∼0.5-1.2 ps component seen in spectroscopic studies. Interestingly, the slower components could not be resolved, possibly because these pathways make only a minor contribution to isomerisation.

5.1.3 The photoactive yellow protein chromophore

Considerable effort has been dedicated to the study of the PYP chromophore outside its native environment to disentangle the intrinsic dynamics of the chromophore from the role of the protein. Several analogues of pCA$^-$ have been the subject of studies in the gas phase and in different solvents. Some of these chromophores, which will be discussed in this section, are presented in Figure 5.2.

5.1.3.1 Dynamics in the gas phase

The excited state dynamics of isolated PYP chromophores have been studied in the gas phase using time-resolved anion photoelectron spectroscopy.[122–125] The first experiments, by Zewail and co-workers, were performed on pCK$^-$ af-

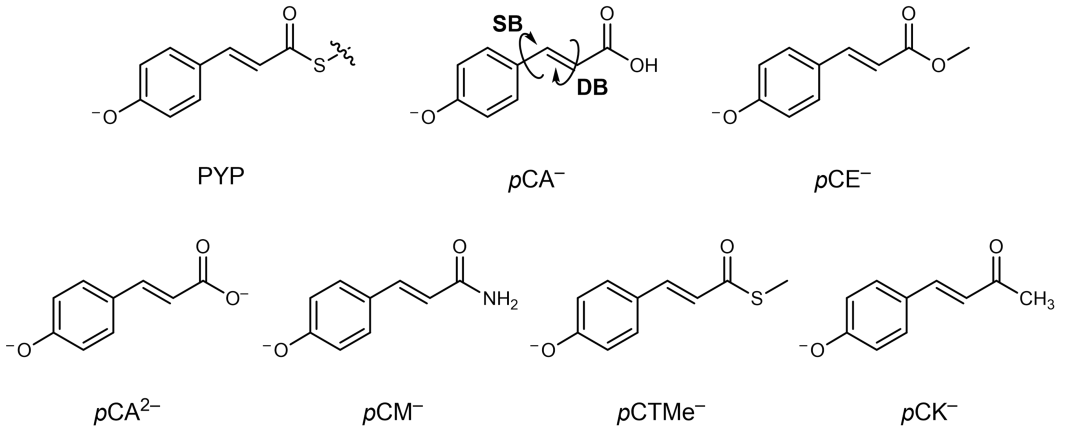

Figure 5.2: Structure of the PYP chromophore in the protein (PYP) and isolated (pCA$^-$). Structure of the analogues of the PYP chromophore referenced in the main text: pCE$^-$, pCA^{2-}, pCM$^-$, pCTMe$^-$, pCK$^-$. Arrows denoted SB and DB indicated torsion about the single and double bonds,respectively, as referenced in the main text.

ter excitation at 400 nm (3.10 eV).[122] Photoelectron spectra were characterised by a large autodetachment signal as the pump photon energy was higher than the adiabatic detachment energy which was subsequently determined to be 2.87±0.05 eV.[124] Zewail and co-workers observed a twisted intermediate which formed on a 1 ps timescale and decayed on a 52 ps timescale and attributed it to rotation about the double bond, based on the similarity of the timescale for its formation to the timescales observed in solution, followed by internal conversion through a conical intersection with the ground state.[122] In subsequent experiments, Anstöter et al. excited pCK$^-$ at 444 nm (2.79 eV) to minimise the signal arising from autodetachment.[124] They measured time-resolved photoelectron spectra and photoelectron angular distributions up to 1 ps and compared them to MS-XMCQDPT2/(aug)-cc-pVTZ calculations (Figure 5.3).[124] They found that the measured eKE and angular distributions were consistent with torsion of the single bond between the phenolate and the double bond, rather than torsion around the double bond (SB and DB in Figure 5.2). The decay of S_1, which was attributed to autodetachment, was observed to occur on a much longer timescale (120 ps) compared to the previous study (52 ps).[122,124] This discrepancy was linked to the higher photon energy employed by Zewail

and co-workers,[122] which was proposed to be sufficient to overcome the barrier associated with the double bond twist.[124] Single-bond rotation was also observed for isolated pCE$^-$, occurring on a 0.6 ± 0.1 ps timescale, and was followed by vibrational autodetachment on a 45 ps timescale.[123] This motion competes with the formation of a dipole-bound-state, a diffuse weakly-bound molecular orbital where an electron is bound by the permanent dipole moment of the neutral core of the anion. Competition between single and double bond rotations is consistent with solution-phase observations (see Section 5.1.3.2).

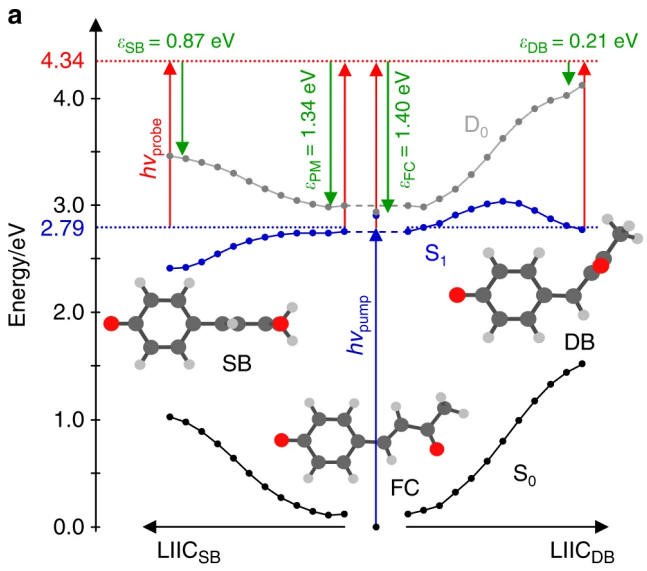

Figure 5.3: Potential energy surface obtained from linearly interpolating internal coordinates connecting the S_1 planar minimum and the S_1 minima along the single bond (SB) and double bond (DB) pathways. Adapted from Ref. 124, licensed under CC BY 4.0.

A later TRPES study of isolated pCK$^-$ revealed ultrafast relaxation to a planar minimum geometry, similar to the Franck-Condon (FC) geometry, occurring within 100-150 fs, before torsion of the single bond,[125] as predicted by numerous computational studies for several analogues of the PYP chromophore.[163–167]

5.1.3.2 Dynamics in solution

The excited-state behaviour of model chromophores of PYP has been studied in aqueous solution with transient absorption spectroscopy[132–135,137,168] and flu-

orescence upconversion.[136,137] Unlike in the gas phase, the minima on the S_1 potential energy surface associated with single and double bond rotations are strongly stabilised by hydrogen bonds with water,[169] and are near conical intersections with the ground state.[164] Consequently, the excited-state relaxation of model PYP chromophores occurs on a few picosecond timescale,[132–137,137,168] considerably faster than in the gas phase, where lifetimes exceed 40 ps.

Investigations into the effects of chemical and structural modifications on the relaxation dynamics of the PYP chromophore have highlighted the role of the substituent at the carbonyl tail of the chromophore. Chromophore analogues bearing strong electron-accepting substituents (like $p\mathrm{CE}^-$ and $p\mathrm{CK}^-$) relax via a transient intermediate to the *trans* ground state. In contrast, analogues with weak electron-accepting groups (like $p\mathrm{CA}^{2-}$ and $p\mathrm{CM}^-$) undergo efficient isomerisation to the *cis* conformer without the formation of a detectable intermediate. The timescales associated with the decay of S_1 decrease with increasing electron-accepting character of the substituent; within the set of examined chromophores, the time constants span about an order of magnitude, ranging from 10 ps for $p\mathrm{CA}^{2-}$ (weakest substituent) to 1.2 ps for $p\mathrm{CK}^-$ (strongest substituent).[133,134]

The nature of the transient intermediate was investigated in pump-dump-probe experiments of $p\mathrm{CTMe}^-$, $p\mathrm{CE}^-$ and analogues of $p\mathrm{CTMe}^-$ and $p\mathrm{CA}^{2-}$ in which both the single and double bonds were locked.[168,170] Unlike standard pump-probe spectroscopy, which monitors the evolution of excited states following a single excitation event, pump-dump-probe experiments introduce a second, dump pulse to selectively depopulate specific excited-state pathways, and are able to distinguish between ground and excited state intermediates. The increase in signal associated with the intermediate state following the dump pulse indicated that it exists on the ground-state potential energy surface. This was attributed to torsion of the single or double bond, as no intermediate could be observed for the locked chromophores.[168] In light of the following discussion, this is consistent with a phenolate-twisted ground state

intermediate.

To investigate the effect of substitution at the carbonyl end, studies focused on employing solvents with different viscosities and polarity.[132,133,136,137] These included water-glycerol mixtures, water-ethanol mixtures and alcohols with progressively longer alkyl chains. The lifetimes of all PYP chromophores increased with increasing solvent viscosity.[132,133,136,137] This effect was more pronounced for chromophores with stronger electron-accepting groups, suggesting that a motion of larger amplitude is involved in these chromophores.[132] Similarly, chromophores with strong electron acceptors exhibited a stronger polarity effect, with more polar solvents leading to shorter excited state lifetimes.[132,136] This behaviour was attributed to a larger stabilisation of the S_1 minimum accessed by these chromophores.[132,134,136,171]

These solvent and substituents effects have been rationalised by the two following schemes:[134,172] (i) rotation about the single bond to a phenolate-twisted intermediate is associated with a larger amplitude motion and a charge transfer from the phenolate moiety to the double bond, facilitated by strong electron-accepting groups; (ii) rotation about the double bond involves a smaller amplitude motion and the return of the negative charge to the phenolate group, which is facilitated by weak electron-accepting groups. A direct comparison of the transient absorption signal of $p\mathrm{CK}^-$ in water and decanol showed that in decanol, which has a lower polarity and higher viscosity than water, a long-lived ($\sim$60 fs) photoproduct is formed.[134] This photoproduct was tentatively assigned to the *cis* isomer, as the phenolate twisted minimum is destabilised and less accessible.[134] These results are supported by computational studies that employed CASPT2, CASSCF and EOM-CCSD,[164,166,169,172] showing that charge migrates to the alkene and carbonyl moieties during single bond rotations, while it remains localised on the phenolate group in double bond rotation. Furthermore, CASSCF/CASPT2 and EOM-CCSD calculations revealed that, while the excitation of $p\mathrm{CK}^-$ involves a charge transfer from the phenolate ring to the alkene and carbonyl tail, excitation of $p\mathrm{CA}^{2-}$ involves a

locally excited state concentrated on the phenolate moiety.[172] This difference in electronic character significantly destabilises the single-bond twisted geometry in $p\mathrm{CA}^{2-}$, which no longer corresponds to a minimum on the S_1 potential energy surface.[172]

5.1.4 Motivation

Time-resolved FU and TAS studies have consistently revealed ultrafast, subpicosecond shifts in emission and absorption features of PYP chromophores in aqueous solution.[133,134,136,137] These dynamical shifts have been assigned to solvent relaxation following the charge transfer induced by photoexcitation, based on their consistency with typical solvent relaxation timescales.[173] However, the clear identification and temporal evolution of solvent relaxation has been hindered by the spectral congestion arising from overlapping contributions, particularly in TAS experiments, where excited and ground state absorption, ground-state bleach, stimulated emission, radical formation and solvated electron absorption overlap.[133,134] This complexity can obscure mechanistic insights into solvent-chromophore interactions, masking the role of the solvent.

Here, UV-pump UV-probe time-resolved liquid-microjet photoelectron spectroscopy is employed to investigate the excited state dynamics of the methyl-ester analogue of the PYP chromophore, $p\mathrm{CE}^-$. TRPES offers advantages over traditional absorption and emission techniques by enabling direct probing of electron binding energies (eBEs) and providing a measure of the difference between the potential energy surfaces of the excited state and the ionised state (i.e., the anion and the neutral radical of $p\mathrm{CE}^-$). Moreover, electron detachment is an always allowed process as there are no stringent selection rules, unlike in optical techniques. This makes it possible to track the evolution of the chromophore across the potential energy surface of the excited state, provided the probe has enough photon energy to detach an electron.

Importantly, the use of UV-pump and UV-probe pulses ensures that only the excited-state dynamics are monitored, effectively excluding ground-state

contributions, thus providing selective probing of photoexcited species.

Additionally, molecular dynamics simulations (Figure 4.11 in Chapter 4) revealed the propensity of pCE$^-$ to reside near the liquid-vacuum interface. The study of pCE$^-$ in this interfacial environment exploiting the surface sensitivity of LJ-PES has the opportunity to provide insight into its photophysics and the effect of solvation on its excited state dynamics. Indeed, recent studies on phenol and phenolate at the water-air interface have demonstrated that photoinduced dynamics can be significantly altered by the liquid surface.[174–177]

5.2 Experimental Details

Aqueous solutions of pCE$^-$ were prepared with 50 µM pCE (>98.0%, Tokyo Chemical Industries) and 2.0 mM NaOH (Sigma Aldrich). A solution of 50 µM pCE in 1.5 mM NaOD (99% D, Sigma Aldrich) and D_2O (99.8% D, Thermo Scientific) was also prepared to investigate isotope effects induced by the solvent response. Details of the operation of the UV liquid microjet instrument and the collection of time-resolved photoelectron spectra have been described in Chapter 2. For the experiments described in this Chapter, pCE$^-$ solutions were introduced into the chamber through a 20 µm fused silica nozzle using a high-performance liquid chromatography pump operating at flow rates of 0.54 ml/min and 0.55 ml/min for H_2O and D_2O experiments, respectively. The liquid jet was intersected by 350 nm (3.54 eV) pump pulses to excite pCE$^-$ and by 266.7 nm (4.65 eV) probe pulses to track the evolution of its excited state at a series of pump-probe delays. The photon energy of the probe pulse is sufficiently high to detach electrons from the excited state but not the ground state, rendering the TRPES signal sensitive solely to excited state dynamics.

Pump and probe powers were attenuated to minimise the contribution from pump-only and probe-only signal, allowing for the collection of time-resolved photoelectron spectra with good signal-to-noise ratio. The pump and probe beams were sequentially blocked using optical choppers to achieve

pump-only, probe-only, pump-probe and background shots every four laser shots. Nine sets of photoelectron spectra were obtained for $p\text{CE}^-$ in H_2O at 47 pump-probe delays, with acquisition times of either 10 s or 20 s per delay, corresponding to 2.5 s and 5 s for each of the four detection channels (pump-only, probe-only, pump-probe and background). The overall scanning time was approximately two hours. For $p\text{CE}^-$ in D_2O, nine sets of photoelectron spectra at 33 pump-probe delays were recorded, with an acquisition time of 20 s per delay. Time-resolved spectra of $p\text{CE}^-$ were obtained by subtracting the contributions from pump-only, probe-only and background signals from the pump-probe signal.

The cross-correlation between a 249.7 nm pump pulse and a 266.7 nm probe pulse, determined using Xe and NO as reference gases, was measured to be 310 fs and 319 fs (Figure 2.15 in Chapter 2), respectively, thereby defining the instrument response function. Attempts to record the cross-correlation with a 350 nm pump pulse were unsuccessful, as one additional photon is required to ionise Xe and NO, and no two-colour signal could be observed. Nevertheless, the cross-correlation between the 350 nm pump and 266.7 nm probe pulses is expected to be similar to that measured with the 249.7 nm pump.

5.3 Results and discussion

5.3.1 TRPES of $p\text{CE}^-$ in water

Figure 5.4a shows the time-resolved photoelectron spectra of 50 µM *p*CE in 2.0 mM aqueous NaOH, and the spectra averaged over selected pump-probe delays are presented in Figure 5.4c. The spectral retrieval software described in Chapter 3 was used to retrieve the true photoelectron spectrum, free from distortion arising from inelastic scattering in the liquid and transmission through the liquid-vacuum interface. The concentration depth profile of $p\text{CE}^-$ obtained from molecular dynamics simulations of the liquid-vacuum interface in Chapter 4 (Figure 4.11a) was employed in this chapter.

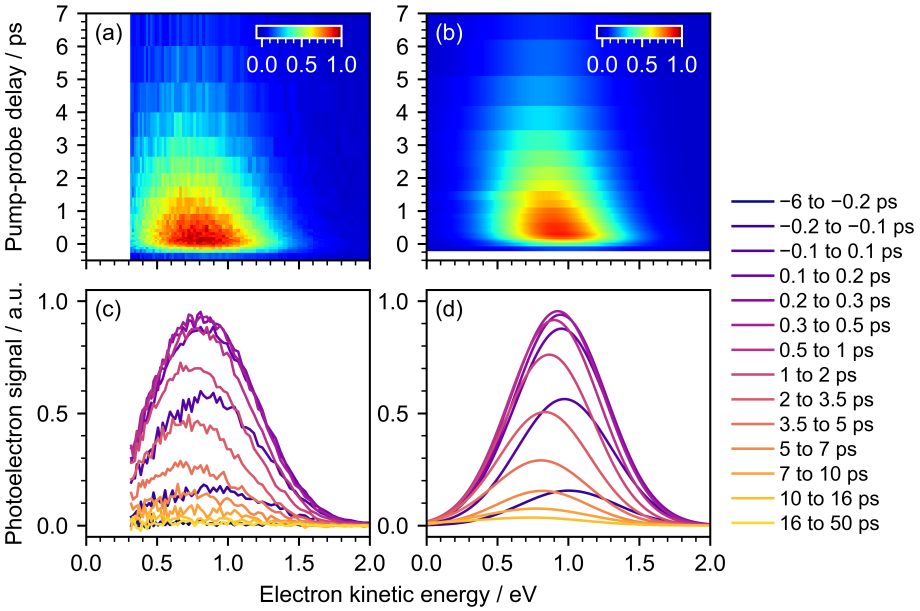

Figure 5.4: Heatmaps of the time-resolved photoelectron spectra and averaged spectra of $p\mathrm{CE}^-$ in water recorded with 350 nm pump pulses and a 266.7 nm probe pulses. (a) Measured photoelectron spectra with eKEs binned every 10 bins. (b) Photoelectron spectra retrieved with LJscatter. (c) Measured and (d) retrieved photoelectron spectra of $p\mathrm{CE}^-$ averaged over specified pump-probe delays. Note that retrieved spectra were obtained for pump-probe delays between −0.17 and 15.03 ps. A heatmap plot of the residuals of (b) is shown in Appendix B.2.

The retrieved one-colour UV spectrum at 350 nm (3.54 eV) presented in Chapter 4 exhibited a signal near 0 eV eKE, which corresponded to one-photon detachment from S_1 (Figure 5.5a). In the work presented in this chapter, the population of S_1 was probed with a higher photon energy (4.65 eV), so the eKE profile is shifted to higher eKE. The time-resolved photoelectron signal reflects one-photon detachment from S_1 and tracks the evolution of the population of $p\mathrm{CE}^-$ on the S_1 potential energy surface. The central eKE of the retrieved Gaussian at $t = 0$ is 0.97 ± 0.09 eV with a FWHM of 0.81 eV, corresponding to an eBE of 3.66 ± 0.09 eV for S_1 (Figure 5.5c). This would appear as a peak at approximately −0.14 eV in the one-colour 350 nm spectrum, which is consistent with the signal near 0 eV eKE. It should be noted that this value does not match the $2h\nu -$ eKE value obtained from the high eKE peak in the 350 nm spectrum (eKE $\sim$ 4.1 eV, Figure 4.13 in Chapter 4), which was also

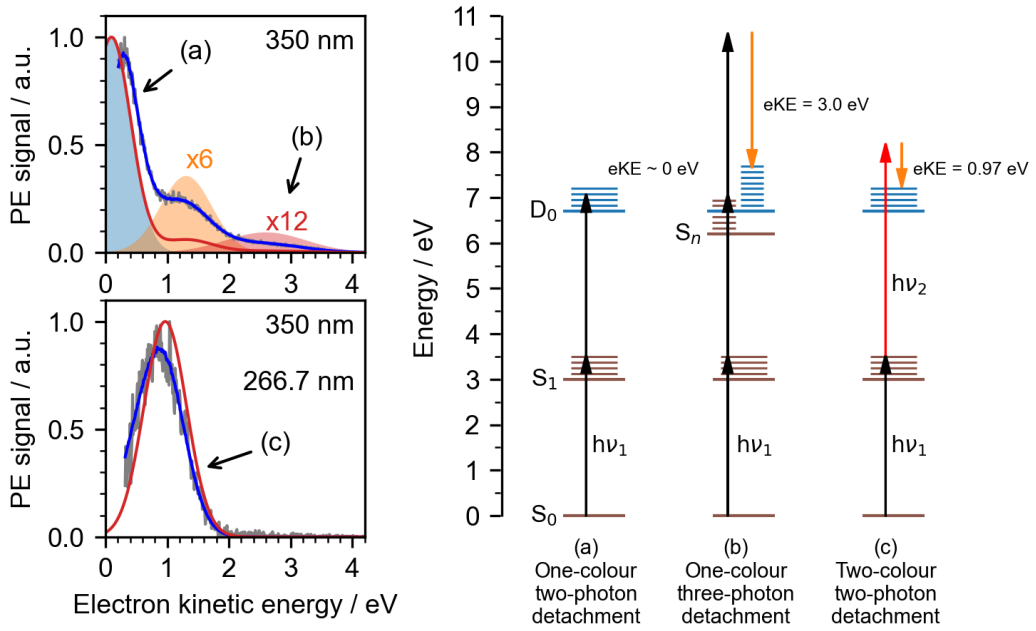

Figure 5.5: Top left: 350 nm photoelectron spectrum of aqueous $p\mathrm{CE}^-$. Bottom left: Time-resolved photoelectron spectrum of aqueous $p\mathrm{CE}^-$ at a pump-probe delay of 0. Right: Energy level diagram of the possible detachment pathways of $p\mathrm{CE}^-$ after one-colour photodetachment with 350 nm ($h\nu_1$) or two-colour photodetachment with 350 nm and 266.7 nm ($h\nu_2$). One-colour photodetachment with 350 nm pulses leads to (a) two-photon detachment to D_0 and (b) three-photon detachment to D_0 via a high-lying excited state S_n. (c) Two-colour photodetachment with 350 nm and 266.7 nm pulses leads to detachment to D_0.

assigned to detachment from S_1 (Figure 5.5b). This discrepancy was attributed the presence of a resonance near the detachment continuum.

Two complementary approaches were employed to analyse the time-resolved data. The first method modelled the time-resolved photoelectron spectra of $p\mathrm{CE}^-$ as a single spectral feature that shifts in eKE over time. The second method assumed the presence of two distinct features with fixed eKE values.

5.3.1.1 First method

As a first analysis, a single Gaussian was employed to retrieve spectra at each pump-probe delay between −0.17 and 15.03 ps; outside this range, spectra did not have enough intensity to confidently apply the retrieval. A heatmap plot

of the retrieved spectra is shown in Figure 5.4b. Figure 5.4d shows retrieved spectra averaged over selected pump-probe delays and extended to 0 eV eKE.

The spectra in Figure 5.4 are characterised by a rise in photoelectron counts at $t = 0$, followed by decay on a picosecond timescale. Figure 5.6a shows the total integrated counts and the area of the retrieved Gaussians as a function of pump-probe delay. Both traces are best described by monoexponential decays with time constants of 2.83±0.05 ps and 3.32±0.07 ps for the measured and retrieved total counts, respectively. Here and in the rest of this chapter, the errors quoted are obtained from the fits and represent one standard deviation.

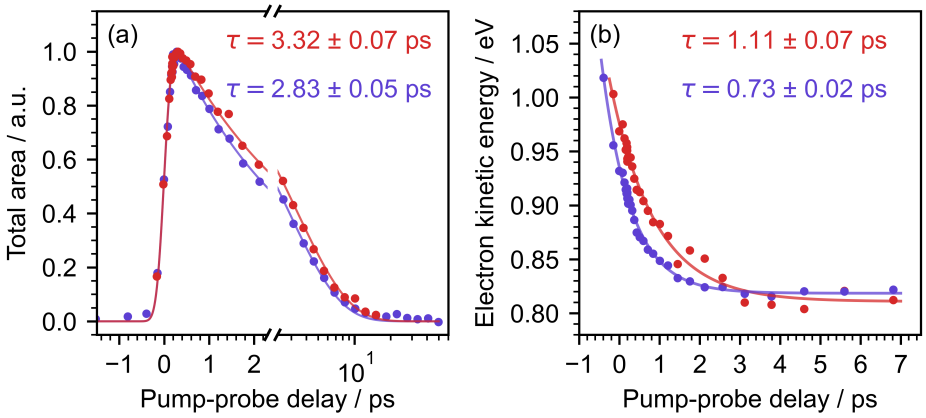

Figure 5.6: (a) Total integrated photoelectron counts (violet) and total retrieved counts (red) of the photoelectron spectra of $p\mathrm{CE}^-$ as a function of pump probe delay. Solid lines indicate fits of monoexponential decays convoluted with a Gaussian (FWHM = 320 fs) and values indicate the time constants and errors associated with the fits. (b) Mean eKE of the measured spectra (violet) and central eKE of the retrieved Gaussian (red) as a function pump probe delay. The solid lines are monoexponential fits to the mean eKE (violet) and retrieved peak centres (red) and the values in ps indicate the time constants and errors associated with the fits.

In Figure 5.4, a clear shift in the eKE distribution of the photoelectron spectra can be observed. This can be quantified by plotting the mean eKE of the spectra and the central eKE of the retrieved Gaussians (Figure 5.6b). The mean eKE of the measured spectra shifts on a 0.73 ± 0.02 ps timescale. However, it does not perfectly represent the spectral shift due to two key factors. First, electrons with lower eKEs experience reduced transmission at

the surface of the jet, resulting in the measured average being skewed toward higher eKE. Second, the distributions are truncated below 0.31 eV because of the poorer collection efficiency of the instrument for low-energy electrons and the additional shift caused by the vacuum level offset. The shift in the central eKE of the retrieved Gaussians occurs on a 1.11 ± 0.07 ps timescale, and likely provides a better measure of the spectral shift.

These results can be interpreted as population evolving on the S_1 potential energy surface, accompanied by a widening of the energy gap between S_1 and D_0, followed by internal conversion through a conical intersection with the ground state (Figure 5.7).

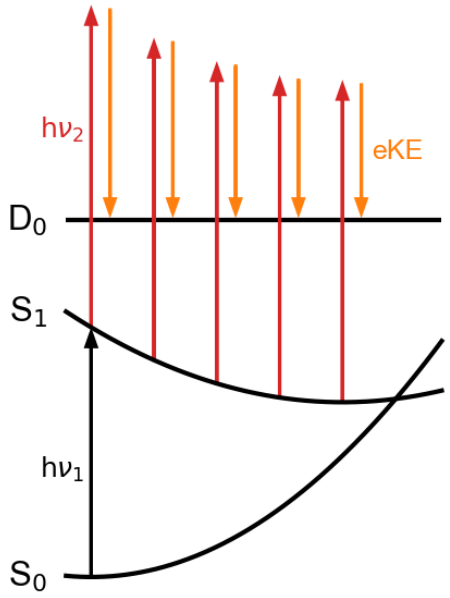

Figure 5.7: Diagram illustrating the evolution of $p\mathrm{CE}^-$ on the potential energy surface of S_1 consistent with a Gaussian shifting in eKE as a function of time. The potential energy surface of D_0 is depicted as a straight line for simplicity, but is expected to vary as a function of nuclear coordinates.

5.3.1.2 Second method

An alternative approach to analyse the TRPES data is to employ decay-associated spectra (DAS) and evolution-associated spectra (EAS). DAS and EAS are commonly used for the analysis of time-resolved spectroscopic data,[178]

and are based on the assumption that the spectroscopic and temporal properties of the system are separable, i.e. the total time-resolved signal can be expressed as a product of the spectral and temporal profiles. The DAS model employed the sum of two exponential decays convoluted with the instrument response function $R(t)$:

$$S(\mathrm{eKE}, t) = \sum_{i}^{2} c_i(\mathrm{eKE}) e^{-t/\tau_i} * R(t) \tag{5.1}$$

where $c_i(\mathrm{eKE})$ represents the contribution of the i^{th} component at a given eKE, and τ_i the time constant associated with the corresponding decay. The EAS model employed a sequential kinetic model A $\xrightarrow{\tau_1}$ B $\xrightarrow{\tau_2}$ C, where A and B are two spectroscopically measurable states and C is a final non-measurable state outside the probing window. The photoelectron signal can thus be described as the sum of the contribution of A and B, $S_{\mathrm{A}}(\mathrm{eKE}, t) + S_{\mathrm{B}}(\mathrm{eKE}, t)$, convoluted with the instrument response function:

$$\begin{aligned} S_{\mathrm{A}}(\mathrm{eKE}, t) &= c_{\mathrm{A}}(\mathrm{eKE}) e^{-t/\tau_1} * R(t) \\ S_{\mathrm{B}}(\mathrm{eKE}, t) &= c_{\mathrm{B}}(\mathrm{eKE}) \frac{\tau_1^{-1}}{\tau_2^{-1} - \tau_1^{-1}} \left(e^{-t/\tau_1} - e^{-t/\tau_2} \right) * R(t) \end{aligned} \tag{5.2}$$

Although decay- and evolution-associated spectra differ in form, they are different linear combinations of the same exponential decays and therefore yield the same rate constants.

The results of the global fits to the measured photoelectron spectra of $p\mathrm{CE}^-$ binned every 10 eKE points are shown in Figure 5.8a. The DAS and EAS are shown in Figure 5.8b, c. The blue and green spectra decay on 0.55 ± 0.03 ps and 2.84 ± 0.03 ps timescales, respectively. The green DAS and EAS show the shape of the signal at long delays after the blue spectrum has decayed. The sign reversal of the blue DAS, combined with its near-zero integrated area, suggests that the system evolves along the S_1 potential energy surface from a region yielding photoelectrons with higher eKE to one producing electrons with lower eKE. This is similarly reflected in the blue EAS which has a peak at

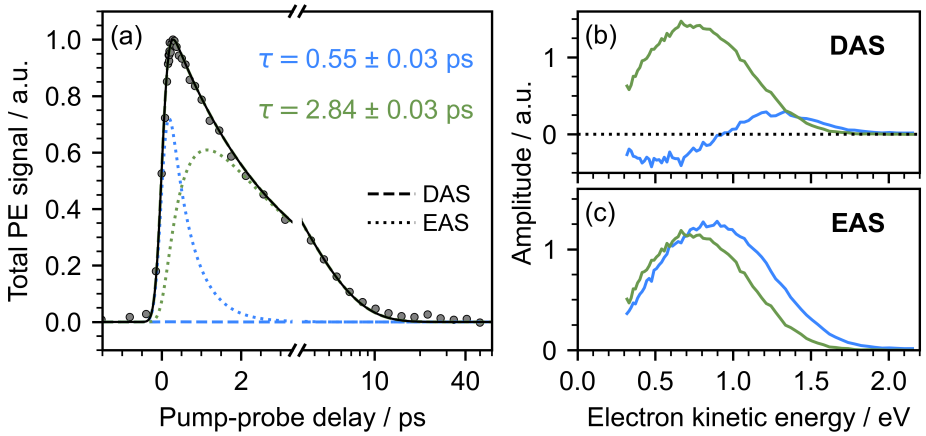

Figure 5.8: (a) Total measured photoelectron counts (circles), DAS (dashed) and EAS (dotted) of $p\mathrm{CE}^-$ in water integrated over eKE and plotted as a function of pump-probe delay. The black solid line indicates the total fit, the blue traces are associated with $\tau = 0.55 \pm 0.03$ ps, and the green traces with $\tau = 2.84 \pm 0.03$ ps. The trace of the blue DAS yields a net contribution of around zero, indicating a transient shift of the signal. In contrast, the green DAS contributes positively and closely follows the total fit. (b) and (c) show the DAS and EAS normalised to the maximum of the green spectrum, respectively. A heatmap plot of the residuals of the global fit is shown in Appendix B.2.

higher eKE (∼0.87 eV) and represents the spectrum of the initial geometry of the excited state than the green one (∼0.75 eV), which represents the spectrum of $p\mathrm{CE}^-$ after it has evolved on the potential energy surface of S_1.

Guided by the spectral features obtained in the DAS and EAS analyses, the time-resolved spectra of $p\mathrm{CE}^-$ were also fit using LJscatter and the sequential model employed in the EAS analysis (A $\xrightarrow{\tau_1}$ B $\xrightarrow{\tau_2}$ C). At each time point, the spectra were modelled as the sum of two Gaussians with globally fixed centre positions and FWHM. The time-dependent evolution of the amplitudes of the Gaussians was modelled using the same exponential decays used in the EAS fits (Equation 5.2). The total signal is thus given by $S_\mathrm{A}(\mathrm{eKE}, t) + S_\mathrm{B}(\mathrm{eKE}, t)$ convoluted with the instrument response function $R(t)$:

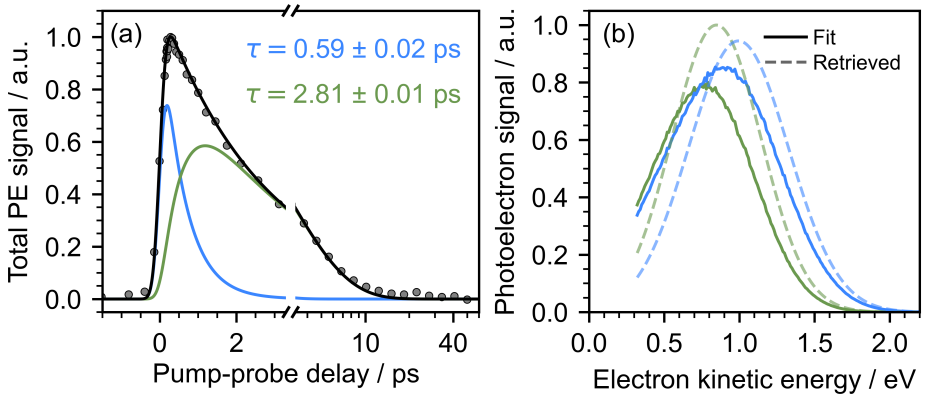

Figure 5.9: (a) Total measured counts (circles) and integrated 'distorted' Gaussians (blue and green lines) as a function of pump-probe delay. The black solid line indicates the total fit, the blue line is associated with $\tau = 0.59 \pm 0.03$ ps, and the green line with $\tau = 2.81 \pm 0.03$ ps. (b) Fit and retrieved Gaussians normalised to the maximum value of the green retrieved Gaussian, respectively. Note that the absolute ratio between the retrieved and fit spectra is arbitrary due to independent normalization, but the relative areas of the blue and green distributions within each set (fit and retrieved) are preserved. A heatmap plot of the residuals of the global fit is shown in Appendix B.2.

$$
\begin{aligned}
S_{\mathrm{A}}(\mathrm{eKE}, t) &= g_{\mathrm{A}}(\mathrm{eKE})\, e^{-t/\tau_1} * R(t) \\
S_{\mathrm{B}}(\mathrm{eKE}, t) &= g_{\mathrm{B}}(\mathrm{eKE})\, \frac{\tau_1^{-1}}{\tau_2^{-1} - \tau_1^{-1}} \left(e^{-t/\tau_1} - e^{-t/\tau_2}\right) * R(t)
\end{aligned}
\tag{5.3}
$$

where $g(\mathrm{eKE})$ is a 'distorted' Gaussian. Attempts to fit the data using simple monoexponential kinetics, as in DAS analysis, resulted in poor fits and are therefore not shown. This is because, unlike when fitting DAS to each eKE independently, the retrieval software does not allow negative amplitudes.

The global fits to the spectra, retrieved spectra and associated kinetic traces are shown in Figure 5.9. The fitted 'distorted' Gaussians are in excellent agreement with the spectral profiles of the EAS obtained without LJscatter and are associated with 0.59 ± 0.02 ps and 2.81 ± 0.01 ps time constants, in good agreement with those obtained from the DAS and EAS of the measured spectra (0.55 ± 0.03 ps and 2.84 ± 0.03 ps). The overall decay of the signal $\langle\tau\rangle$ is given by the weighted mean of the individual lifetimes

$$\langle \tau \rangle = \frac{S_A \tau_1 + S_B \tau_2}{S_A + S_B} \tag{5.4}$$

where S_A and S_B are the areas under the retrieved Gaussians. A $\langle \tau \rangle$ of 3.24 ± 0.03 ps was obtained from the global fit of LJscatter, in good agreement with the monoexponential fit of the retrieved total counts employing one Gaussian (3.32 ± 0.07 ps). The retrieved Gaussians have central eKEs of 0.99 ± 0.09 eV (eBE = 3.65 ± 0.09 eV) and 0.85 ± 0.09 eV (eBE = 3.80 ± 0.09 eV) and FWHM of 0.78 eV and 0.70 eV, respectively. A schematic representation of this shift is shown in Figure 5.10. The ratio of the area of the blue and green retrieved Gaussians is $1.06 \approx 1$, indicating a single decay pathway, with the population associated with the blue peak evolving into that of the green. This suggests that, after initial population of S_1, the system moves away from the Franck-Condon region, either along nuclear coordinates of pCE$^-$ or as a consequence of solvent reorganisation, before disappearing from the observation window of the experiment.

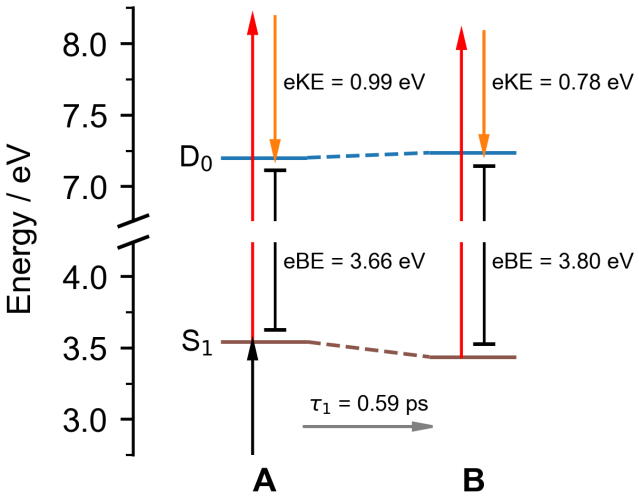

Figure 5.10: Energy level diagram of the features obtained from the global LJscatter fit. The pump pulse (black arrow) excites pCE$^-$ to S_1 and the probe pulse (red arrows) monitors the evolution of pCE$^-$ on the S_1 potential energy surface. Species A (eKE = 0.99 ± 0.09 eV) evolves into species B (eKE = 0.78 ± 0.09 eV) on a 0.59 ± 0.02 ps timescale. Species B decays on a 2.81 ± 0.01 ps timescale.

Fluorescence upconversion (FU) measurements of pCE$^-$ and several PYP chromophore analogues in water revealed that the fluorescence of the chromophores decayed as a biexponential and was characterised by a red shift in the spectra as a function of time.[136,137] The first component of the biexponential and the shift in the maximum of fluorescence spectra both exhibited a ∼0.9 ps time constant, comparable to the 0.59 ± 0.02 ps obtained for A $\rightarrow$ B and the 1.11 ± 0.07 ps shift in eKE of the single Gaussian fit. A similar dynamical shift was observed in TAS measurements which revealed a red shift in the stimulated emission band occurring in under 1 ps.[133,134] These observations were interpreted as solvent reorganisation, which for water occurs on sub-picosecond timescales.[173] This was attributed to a charge transfer from the phenolate moiety to the double bond and carbonyl moieties involved in the S_0-S_1 excitation, as predicted by QM/MM computational studies at the CASPT2//CASSCF/cc-pVDZ level of theory,[164,166] and EOM-CCSD/cc-pVDZ calculations of the thioester analogue with two water molecules.[179]

5.3.2 TRPES of pCE$^-$ in D_2O

To test whether the fast timescale observed in the TRPES measurements in water could be interpreted as solvent relaxation, time-resolved photoelectron spectra of pCE$^-$ in NaOD and D_2O were recorded to exploit the isotope effect which is expected to increase the time constants associated with the solvent response. If the solvent relaxation is mediated by librational or vibrational modes of water, a ∼1.4 isotope effect should be observed,[180] as the vibrational frequencies of D_2O are larger because of the higher reduced mass of the OD bonds. If the solvent response is mediated by the translation of solvent molecules, a 1.1-1.3 isotope effect is expected,[181,182] due to the increased molecular mass and viscosity of D_2O. A heatmap plot of the time-resolved spectra of pCE$^-$ in D_2O and the measured photoelectron spectra averaged over selected pump-probe delays are shown in Figure 5.11.

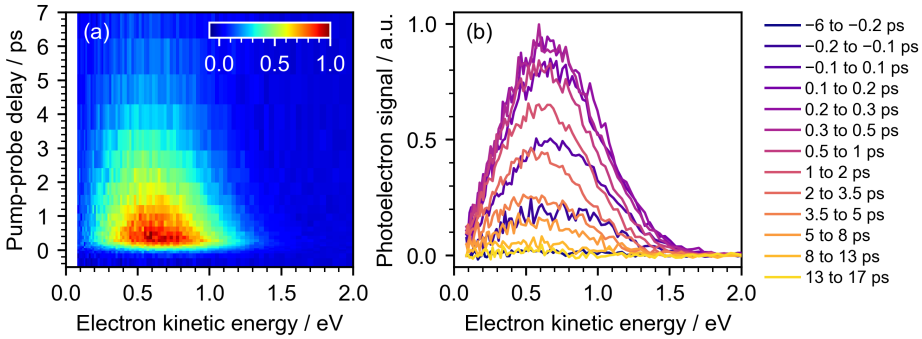

Figure 5.11: (a) Heatmap of the time-resolved photoelectron spectra of pCE$^-$ in D_2O recorded with a 350 nm pump pulse and a 266.7 nm probe pulse. The eKE of the spectra was rebinned every 10 bins. (b) Measured photoelectron spectra averaged over specified pump-probe delays.

5.3.2.1 Spectral shift in D_2O

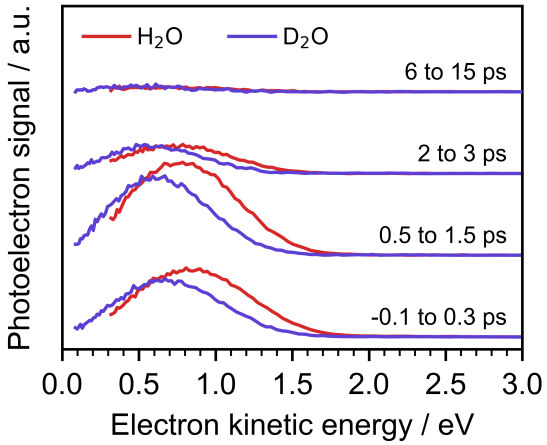

Figure 5.12: Averaged time-resolved spectra of pCE$^-$ in H_2O (red) and D_2O (violet) at selected pump-probe delays. The maximum of the pCE$^-$ spectra in D_2O is shifted ∼0.2 eV to lower eKE.

The photoelectron spectra of pCE$^-$ in D_2O are characterised by photoelectron distributions shifted ∼0.2 eV to lower eKEs compared to the photoelectron spectra of pCE$^-$ in H_2O (Figure 5.12). This shift is similarly reflected in the pump-only and probe-only photoelectron spectra of pCE$^-$ in H_2O and D_2O at eKEs below ∼1.5 eV (Figure 5.13). Differences in the electronic structure of the pCE$^-$ chromophore itself are excluded as a potential reason for this difference as the UV-Vis spectra of pCE$^-$ in H_2O and D_2O are identical

(Appendix B.1). While this is only indicative that the energy gap between the ground state and the excited states of $p\mathrm{CE}^-$ is unchanged, it is unlikely that all states would shift by the same amount with respect to the detachment continuum. Moreover, the VIEs of H_2O and D_2O in the gas phase are almost identical,[183] and the VIEs of liquid H_2O and D_2O were found to be the same[27] or differ by 0.11 eV.[43] However, the latter were recorded at a time when the effects of the streaming potential were poorly understood and thus do not provide an accurate measure of any isotope effect. Vertical detachment energies of $p\mathrm{CE}^-$ are therefore assumed to remain the same in H_2O and D_2O. The most likely explanation for the shift in the measured spectra of $p\mathrm{CE}^-$ in D_2O compared to H_2O is the effect of electron scattering inside the liquid before they escape the jet.

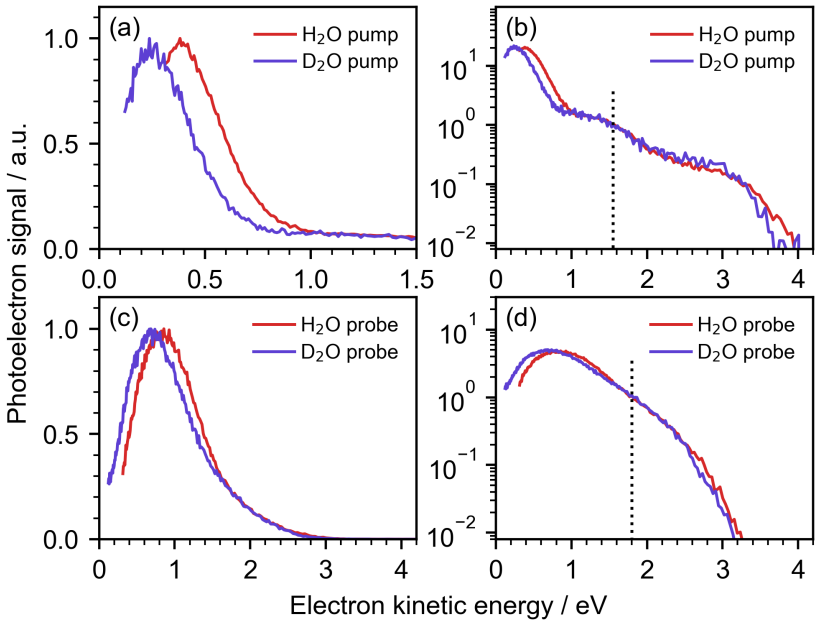

Figure 5.13: (a, b) Pump-only and (c, d) probe-only photoelectron spectra of $p\mathrm{CE}^-$ in H_2O (red lines) and D_2O (violet lines). (a, c) The spectra were normalised to their maximum intensity. (b, d) The spectra were normalised to their intensity at eKEs denoted by the vertical dotted lines and plotted on a log scale to highlight the similarities between the spectra at high eKE.

Although one may expect a smaller overall distortion in D_2O due to its lower librational and vibrational frequencies, to the best of our knowledge, the

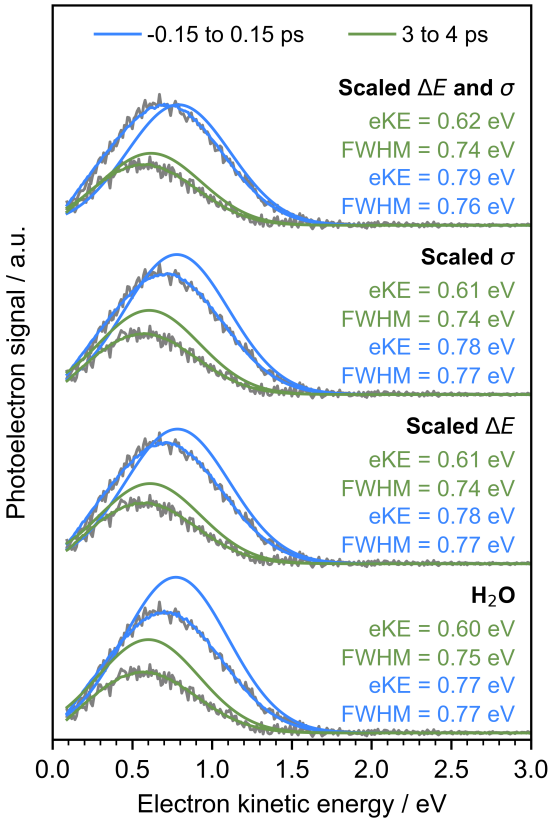

Figure 5.14: Effect of scaling the cross sections (σ) and the mean energy losses (ΔE) associated with the vibrational and librational scattering channels employed in LJscatter by 1/1.3736. The photoelectron spectra of $p\mathrm{CE}^-$ in D_2O recorded at pump-probe delays ranging −0.15–0.15 ps and 3–4 ps were averaged and retrieved using the H_2O parameters, only scaling the mean energy losses, only scaling the cross sections, and scaling both the cross sections and mean energy losses.

scattering cross sections in liquid D_2O are not known, and may thus contribute to a larger eKE shift. In fact, the total electron scattering cross sections for D_2O have only been measured in the gas-phase for eKEs above ∼0.6 eV and were found to be within experimental error of those for H_2O.[184,185] In contrast, measurements limited to the vibrational cross sections in the gas phase revealed a notable isotope effect.[186,187] The vibrational differential cross sections for the stretching modes of H_2O were found to be a 1.47 times larger than for D_2O at an incident eKE of 8 eV and a scattering angle of 40°,[186] while a 1.3–1.4 isotope effect was found for all vibrational modes at a final eKE of 0.6 eV (with initial eKEs ranging from 0.75 to 1.05 eV) and a scattering angle of

135°.[187] These values are consistent with $\sqrt{\mu_{OD}/\mu_{OH}} = 1.37$, where μ denotes the reduced mass of OD and OH bonds. To investigate the impact of lower vibrational frequencies and scattering cross sections, additional simulations were performed with LJscatter. The cross sections and mean energy losses associated with scattering channels involving librations and vibrations were scaled by a factor of 1/1.37. Retrieval of the spectra of $p\mathrm{CE}^-$ in D_2O with basis sets obtained from these simulations yielded negligible spectral shifts compared to the retrieval using the H_2O parameters (Figure 5.14). The lack of any significant shift may be due to the small absolute shift induced by scaling the energy losses and cross sections. It is likely that the isotope effect on the cross sections is dependent on eKE, since significant shifts are only observed at low eKEs in the pump-only and probe-only spectra. This hypothesis could not be tested using LJscatter, due to the difficulty in predicting the eKE dependence. Therefore, the spectral shift at low eKE is tentatively assigned to an eKE-dependent isotope effect on the scattering of electrons in liquid water.

5.3.2.2 Kinetic analysis

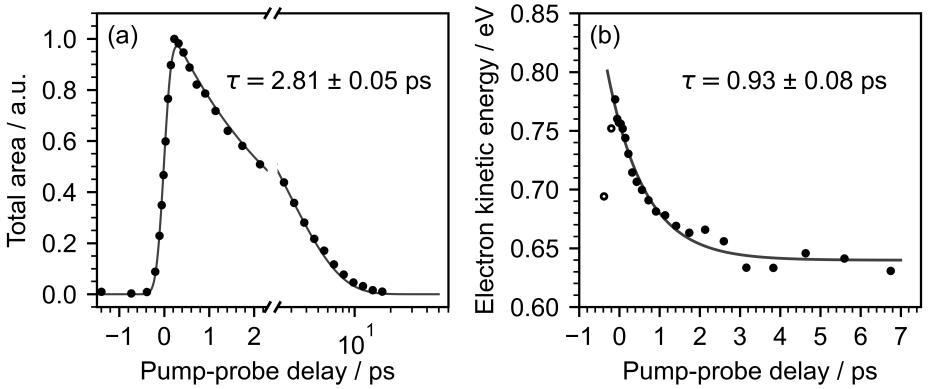

Figure 5.15: (a) Total integrated photoelectron counts (circles) of the photoelectron spectra of $p\mathrm{CE}^-$ in D_2O as a function of pump-probe delay. The solid line indicates a monoexponential fit convoluted with the a Gaussian (FWHM = 320 fs). (b) Mean eKE of the measured spectra (circles) fit with a exponential decay. Empty circles were not included in the fit,as they correspond to negative pump–probe delays where the pulses are not temporally overlapped. Values in ps indicate the time constants and the errors associated with the fits.

Since the photoelectron spectra for the D2O data cannot be retrieved confidently, the following kinetic analysis is limited to the measured spectra.

The integrated photoelectron counts were fitted with a monoexponential decay, yielding a time constant of 2.81 ± 0.05 ps (Figure 5.16a), in close agreement with the time constant obtained in H_2O (2.83 ± 0.05 ps). The shift in mean eKE of the measured spectra occurs on a 0.93 ± 0.08 ps timescale, slightly longer than in H_2O (0.73 ± 0.02 ps), corresponding to an increase by a factor of 1.3.

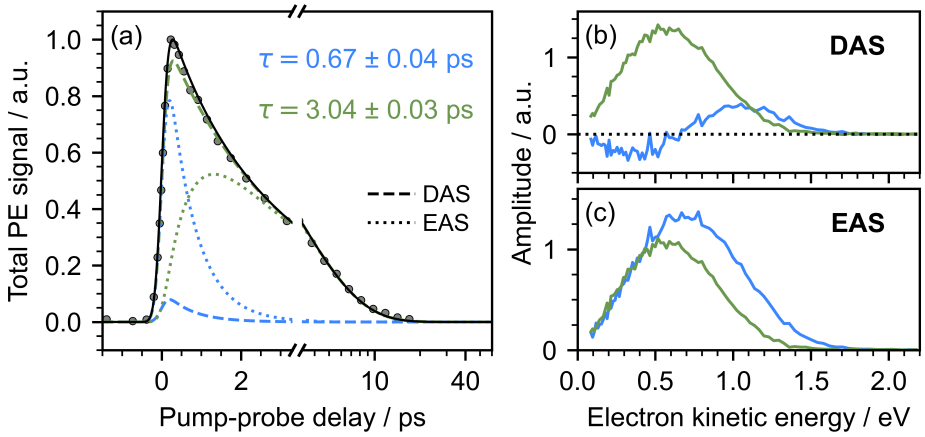

Figure 5.16: (a) Total measured photoelectron counts (circles), DAS (dashed) and EAS (dotted) of $p\mathrm{CE}^-$ in D_2O integrated over eKE and plotted as a function of pump-probe delay. The black solid line indicates the total fit, the blue traces are associated with $\tau = 0.55 \pm 0.03$ ps, and the green traces with $\tau = 2.84 \pm 0.03$ ps. (b) and (c) show the DAS and EAS normalised to the maximum value of the green spectrum, respectively. A heatmap plot of the residuals of the global fit is shown in Appendix B.2.

The time constants of $p\mathrm{CE}^-$ in H_2O obtained from the measured EAS and DAS (0.55 ± 0.03 ps and 2.84 ± 0.03 ps) closely matched those obtained from fitting LJscatter (0.59 ± 0.03 ps and 2.81 ± 0.03 ps). Therefore, DAS and EAS were fit to the measured spectra (Figure 5.15), yielding time constants of 0.67 ± 0.04 ps and 3.04 ± 0.03 ps, with an overall decay of the total signal of 2.80 ± 0.05 ps. Interestingly, despite the timescale of the overall decay being unaffected by a heavier solvent isotopomer, the fast and slow components are slightly larger by factors of 1.2 and 1.1, respectively.

The differences between the time constants of $p\mathrm{CE}^-$ in H_2O and in D_2O range from 0.12 to 0.20 ps. These values are smaller than the IRF (0.32 ps), being representing only 38–62% of its value, which complicates their interpretation. Nevertheless, time-resolved LJ-PES experiments investigating the relaxation of the hydrated electron were able to resolve an isotope effect of 1.4 ± 0.2 for one of the decay constants, despite their absolute difference being only 40% of the IRF.[180] Therefore, the longer time constants observed in this work could suggest a significant isotope effect

The ratios obtained here are inconsistent with solvent reorganisation mediated by vibrational or librational modes, which would result in a $\sim$1.4 increase in the lifetime,[180] but may be due to solvent response mediated by translational diffusion of the solvent.[181,182] Moreover, TAS and FU measurements revealed that the viscosity of the solvent affects the timescale of the deactivation of S_1 for all PYP analogues. Those with stronger electron-accepting groups at the carbonyl end (such as $p\mathrm{CE}^-$), which preferentially relax via torsion of the single bond, exhibited a stronger dependence on viscosity,[134,136] attributed to the large amplitude motion of the phenolate twist as compared to the double-bond twist. As the viscosity of D_2O is larger by a factor of $\sim$1.2,[188] an alternative explanation could be that the evolution from A to B involves twisting of the phenolate group around the single bond.

5.3.3 Summary of time constants

Table 5.1 shows the time constants obtained in the analysis carried out in the previous sections.

Table 5.1: Time constants associated with the decay of the S_1 state of pCE$^-$ in H_2O and D_2O, measured with an IRF of ∼0.32 ps. Values are in ps. Errors are obtained from the fits and represent one standard deviation. Values were obtained using various fitting approaches: monoexponential fits to the total measured signals; biexponential fits to the measured data using EAS and DAS; and fits to the time-resolved spectra of pCE$^-$ in H_2O using either one shifting 'distorted' Gaussian or two fixed 'distorted' Gaussians using LJscatter. For biexponential fits the time constants of the overall decay of the signal $\langle\tau\rangle$, given by the amplitude-weighted sum of each component, are also reported. For biexponential fits, the area of the EAS or retrieved Gaussians is shown in brackets. Additionally, time constants associated with the shift in mean eKE of the measured spectra in both solvents and the evolution of the central eKE of single retrieved Gaussian of the spectra in H_2O are reported.

PE signal			H_2O	D_2O	Ratio
Meas.	Tot. PE sig.	τ	2.83 ± 0.05	2.81 ± 0.05	1.0
	EAS/DAS	τ_1	0.55 ± 0.03 (0.55)	0.67 ± 0.04 (0.59)	1.2
		τ_2	2.84 ± 0.03 (0.45)	3.04 ± 0.03 (0.41)	1.1
		$\langle\tau\rangle$	2.84 ± 0.03	2.80 ± 0.04	1.0
Retr.	One Gauss.	τ	3.32 ± 0.07	-	
	Two Gauss.	τ_1	0.59 ± 0.02 (0.51)	-	
		τ_2	2.81 ± 0.01 (0.49)	-	
		$\langle\tau\rangle$	3.24 ± 0.02	-	
eKE			H_2O	D_2O	Ratio
Meas.	Mean	τ_{eKE}	0.73 ± 0.02	0.93 ± 0.08	1.3
Retr.	Centre	τ_{eKE}	1.11 ± 0.07	-	

5.3.4 Relaxation mechanism

In order to assign the processes associated with either the shift in eKE observed assuming one Gaussian or the rise and decay of the transient species A (blue spectra) and B (green spectra) obtained from the global fit of two Gaussians, this section explores two possible mechanisms for the evolution of pCE$^-$ on the S_1 potential energy surface.

Three key geometries have been found to be implicated in the relaxation of analogues of the PYP chromophore in the gas phase and in aqueous solution, using a variety of experimental and computational methods,[123,125,133,163,164,172] as summarised in Figure 5.3. The chromophores are generally believed to relax to a planar minimum (PM) with a geometry similar to the equilibrium ground state geometry, before accessing rotations about the single or double

bond.[125,163–167] Relaxation to the planar minimum has been observed experimentally as a 0.07 eV shift in the gas-phase photoelectron spectra of the ketone analogue pCK$^-$, occurring within the first 100-150 fs.[125] Experimental evidence for the planar minimum has not been found in aqueous solution, likely due to line broadening in solution and the overlap with the shift attributed to solvent relaxation. It is thus unlikely that this shift can be observed in the experiments presented in this chapter.

Following relaxation to the planar minimum, the chromophore can undergo rotations about the single and double bonds, each associated with energy barriers. MS-XMCQDPT2/(aug)-cc-pVTZ potential energy surface calculations of isolated pCK$^-$ [124] and EOM-CCSD/aug-cc-pVDZ calculations of pCTMe$^-$ microsolvated with two water molecules[163] revealed that, for chromophores with strong electron-accepting substituents like pCE$^-$, the barrier to single bond rotation is extremely small. Conversely, double bond rotation has a significant barrier of approximately 0.2-0.4 eV[124,126,163,165]

Gas-phase TRPES experiments confirmed that pCE$^-$ undergoes exclusively single-bond rotation,[123,124] which occurs on a 0.6 ± 0.1 ps timescale and is followed by vibrational autodetachment on a 45 ps timescale.[123] This fast component is in agreement with the decay of species A and formation of species B observed in this work (0.59 ± 0.02 ps). Given the surface sensitivity of LJ-PES, the observed dynamics may reflect interfacial behaviour that differs from the bulk dynamics. Indeed, sum-frequency generation spectroscopy of phenol and phenolate revealed that their excited state dynamics at the water surface differ significantly from those in the bulk.[174–177] For phenol, dissociation is accelerated at the interface due to a lowering of the dissociative state.[174,175] In the case of phenolate, while both fast and slower electron ejection pathways are accessible in bulk solution, only the fast component is observed at the surface.[176,177] These studies highlight that the interfacial environment can influence excited state dynamics.

In aqueous solution, the minima associated with both rotations of pCE$^-$

are stabilised and are located near conical intersections with the ground state.[164,169,179] Therefore, the decay of the excited state of *p*CE$^-$ in bulk aqueous solution (2.8-3 ps) via single-bond rotation proceeds on a much faster timescale than in the gas phase (45 ps) .[133,134,136,137] Notably, the excited state decay of *p*CE$^-$ in H_2O observed with LJ-PES (2.81 ± 0.01 ps) is in excellent agreement with the time constants obtained from bulk aqueous solution measurements using FU (2.8 ps)[136] and TAS (3.0 ± 0.5 ps).[133]

In TAS and FU experiments, the timescale associated with single-bond rotation of *p*CE$^-$ was not directly observed in water; instead, the sub-picosecond red shift of the fluorescence and stimulated emission signals was assigned to solvent relaxation.[133,134,136,137] The fastest component of the biexponential decay of the FU signal and the shift in the maximum of the fluorescence spectra both exhibited a ∼0.9 ps time constant, which is consistent with the eKE shift (1.11 ± 0.07 ps) and the time constant for A $\rightarrow$ B (0.59 ± 0.02) observed in this work. The concurrent decay of the TAS and FU signals was attributed to depletion of the FC/PM geometries.[133,134,136,137] This is followed by the formation of a transient ground state intermediate, which relaxes to the *trans* ground state on a 4.5 ps timescale.[133,168] As the probe employed in this work (266.7 nm, 4.65 eV) selectively detaches electrons from the first excited state, ground-state transients cannot be observed in the time-resolved photoelectron spectra.

Based on the discussion above, the assignment of species A and B in the time-resolved photoelectron spectra can be addressed. Species A is attributed to the Franck-Condon or planar minimum geometries, formed immediately upon excitation of *p*CE$^-$. This species then evolves into species B on a 0.59 ± 0.02 ps timescale. Species B subsequently decays on a 2.81 ± 0.01 ps timescale via a conical intersection located near the minimum on the S_1 potential energy surface associated with torsion of the single bond. The assignment of species B is less straightforward, and two mechanisms are proposed to account for its formation (Figure 5.17). These mechanisms cannot be distin-

guished by our TRPES measurements without supporting theory.

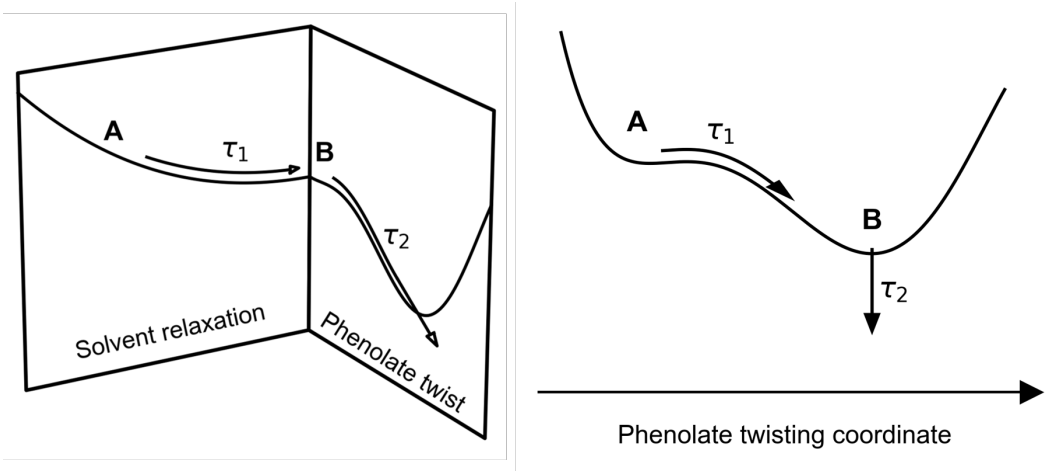

Figure 5.17: Possible relaxation mechanisms of *p*CE$^-$ after excitation to S_1. In both mechanisms species A is associated with the FC geometry or a rapidly formed PM geometry. Left: species A evolves into species B through relaxation of the solvent. Species B decays via torsional motion around the single bond (phenolate twist) and internal conversion to the ground state. Right: species A directly accesses the single bond torsional coordinate, forming species B with a twisted phenolate geometry. The decay of species B is governed by the search for the conical intersection connecting S_1 to S_0.

In the first mechanism (Figure 5.17, left), *p*CE$^-$ evolves along solvent relaxation coordinates, primarily driven by translational motion of water. This leads to a solvent-relaxed geometry, associated with species B. Subsequently, *p*CE$^-$ decays by twisting around the single bond and reaches the conical intersection connecting S_1 to S_0 on a 2.81 ± 0.01 ps timescale. This pathway is consistent with literature interpretations of relaxation dynamics observed in bulk aqueous solution, where solvent reorganization has been proposed to play a significant role.[133,134,137]

In the second proposed mechanism (Figure 5.17, right), species A directly accesses the single-bond twisting coordinate forming species B, which is associated with the twisted phenolate geometry. The search for the conical intersection with the ground state occurs on a 2.81 ± 0.01 ps timescale, leading to the loss of photoelectron signal. This mechanism resembles that proposed to account for measurements in the gas-phase, where torsion dominates the

relaxation process, albeit with an accelerated excited state deactivation due to the proximity of the phenolate-twisted minimum to the conical intersection with the ground state.

It is also possible that solvent relaxation and torsional motion are coupled and occur simultaneously. Evidence for this hypothesis lies in the fact that the TRPES signal of $p\text{CE}^-$ is well described by a single 'distorted' Gaussian that shifts over time, capturing the evolution of $p\text{CE}^-$ on the potential energy surface of S_1.

Calculations mapping the projection of S_1 onto the ground state of the neutral radical D_0 are being undertaken in the group of Chiara Cappelli at the Scuola Normale Superiore (Pisa, Italy) and should shed light on which of the proposed mechanisms is most likely.

5.4 Summary and Outlook

This chapter employed UV-pump UV-probe TRPES to explore the excited state dynamics of the ester analogue of the photoactive yellow protein chromophore in aqueous solution. This study represents the first liquid-microjet TRPES study of a protein chromophore at sub-millimolar concentrations, demonstrating the capability of UV LJ-PES in studying systems close to physiological conditions.

The deactivation of the first excited state of $p\text{CE}^-$, involved in the isomerisation of the chromophore in PYP, proceeds via one decay channel, and the photoelectron spectra of two transient configurations have been identified. The first species (A) forms within the instrument response function (320 fs) and is attributed to the Franck-Condon region or a planar minimum on the S_1 potential energy surface. Species A evolves into a second species (B) on a 0.59 ± 0.02 ps timescale. The formation of species B was interpreted through two possible mechanisms. The first mechanism involves solvent relaxation followed by twisting of the single bond adjacent to the phenolate moiety, in excellent agreement with studies of $p\text{CE}^-$ in bulk aqueous solution. The sec-

ond mechanism involves torsion of the single bond followed by search of the conical intersection connecting S_1 and S_0. Species B decays on a 2.81 ± 0.01 ps timescale, attributed to internal conversion to the ground state.

These results provide new insight into the photophysics of PYP chromophores in aqueous solution, revealing spectroscopic signatures of key steps in the isomerisation process. This work underscores the strengths of TRPES to access ultrafast dynamics in solvated systems and paves the way for future studies of biologically relevant chromophores in increasingly complex environments. Future TRPES experiments of $p\text{CE}^-$ in aqueous solution employing a EUV probe, which can directly detach electrons from the ground state, will be critical for resolving the dynamics of the ground state intermediate. Moreover, measurements of electron scattering cross sections in D_2O are needed to better compare the results of $p\text{CE}^-$ in H_2O and D_2O.

Chapter 6

Summary and Outlook

The aim of the work presented in this thesis was to record accurate electron binding energies (eBE) of the methyl ester analogue of the photoactive yellow protein chromophore, pCE$^-$, and to explore its excited state dynamics with ultraviolet (UV) liquid-microjet photoelectron spectroscopy (LJ-PES). UV LJ-PES has the advantage over X-ray and extreme UV (EUV) LJ-PES of being able to study solutes at sub-mM concentrations, significantly reducing the contribution of photoelectrons originating from ionisation of water by employing multiphoton ionisation. However, UV photoelectron spectra are distorted by inelastic scattering of low energy electrons (eKE $\lesssim$ 6 eV) in water, complicating the determination of accurate eBEs.

Chapter 3 addressed the challenge of retrieving accurate electron binding energies from UV photoelectron spectra of aqueous solutions by refining Monte Carlo simulations of electron transport in water and investigating the effect of several parameters that have been source of discussion in the literature. It was found that the amorphous ice electron scattering cross sections extrapolated to zero eKE best describe the distortion of the UV photoelectron spectrum of water, yielding a value of 11.31 ± 0.09 eV for the vertical ionisation energy of water, in excellent agreement with accurate studies employing X-ray and EUV light sources. An investigation of the transmission of electrons at the liquid-vacuum interface, which is controlled by a barrier height equal to the electron affinity of water at the surface, revealed that the escape of electrons is best

treated by calculating the component of the eKE perpendicular to the surface for every electron rather than applying a transmission function *a posteriori*. Additionally, a value for the electron affinity at the water surface of 1.0 eV was inferred from the agreement of the retrieved VIE of water with X-ray experiments. Finally, the UV photoelectron spectra of phenol and phenolate were employed to gain insight into how weighting the contributions of electrons originating from different depths by concentration depth profiles obtained from molecular dynamics simulations affects the retrieval the VIE of phenol and the VDE of phenolate. The results of this chapter provide a solid foundation for improving our understanding of low energy electron scattering in water and the application of UV LJ-PES for the investigation of electronic structure and excited state dynamics of aqueous solutions.

Chapter 4 presented a study of the electronic structure of $p\text{CE}^-$ with X-ray, EUV and multiphoton UV LJ-PES, yielding values for the first two VDEs of $p\text{CE}^-$ of 6.8 ± 0.1 eV and 7.8 ± 0.1 eV, and a value for the ADE of $\sim$5.9 eV. Investigation of the excited state landscape through power and wavelength dependent measurements confirmed the presence of a high-lying resonance accessed via excitation of the first excited state, which has been previously implicated in the formation of solvated electrons from the chromophore in solution and within the protein environment. Additionally, a resonance embedded in the detachment continuum, a feature commonly observed in isolated anions, was identified for the first time for an anion in aqueous solution.

Chapter 5 presented the first liquid-microjet time-resolved PES study of a protein chromophore in aqueous solution. UV-pump UV-probe TRPES was employed to unravel the excited state dynamics of $p\text{CE}^-$ in water following excitation to its first excited state, which plays a key role in the *trans-cis* isomerisation of the chromophore and initiates the photocycle of PYP. The photoelectron spectra of $p\text{CE}^-$ were found to shift to lower eKEs on a 0.59 ± 0.02 ps timescale, consistent with either torsion around the single bond adjacent to the double bond or solvent relaxation. This was followed by passage through

a conical intersection to the ground state on a 2.81 ± 0.01 ps timescale. This study provides insight into the sub-ps dynamics of the chromophore revealing the spectral profiles associated with these two transient configurations, and benchmark data for computational chemistry calculations

In terms of future directions, UV-pump EUV-probe TRPES will allow population to be tracked all the way back to the ground state. Coupling high-harmonic generation EUV pulses with the liquid-jet spectrometer is currently in progress at UCL. Importantly, the focal size of the EUV pulses has been designed to be comparable to the size of the liquid jet, ensuring the contribution from water vapour photoionisation is minimised. All other groups carrying out UV-pump EUV-probe TRPES have focal sizes much larger than the liquid jet diameter. UV-pump EUV-probe experiments of aqueous $p\text{CE}^-$ will be able to confirm whether the longest time constant measured with UV pulses corresponds to internal conversion by monitoring the repopulation of the ground state. This will also help disentangle the formation and decay of the ground state intermediate, whose absorption overlaps with other features in transient absorption spectroscopy measurement. The ground state intermediate is expected to have a larger VDE than the excited state, allowing LJ-PES to distinguish it from excited state features.

Extension of the Monte Carlo simulations to higher eKEs will prove invaluable for modelling the photoelectron spectra obtained with EUV radiation, especially with photon energies lower than approximately 25 eV, where electron scattering significantly distorts photoelectron distributions, hindering the determination of accurate eBEs.

Promising future directions for UV-pump UV-prove TRPES include investigating the excited state dynamics of PYP, exploiting the sensitivity of LJ-PES to low concentrations. This capability enables the study of scarce samples, shedding new light on the relaxation pathways leading to isomerisation in the protein.

Appendix A

Supporting information: X-ray, EUV and UV photoelectron spectroscopy of the photoactive yellow protein chromophore in aqueous solution

A.1 NMR spectra of *p*CE⁻

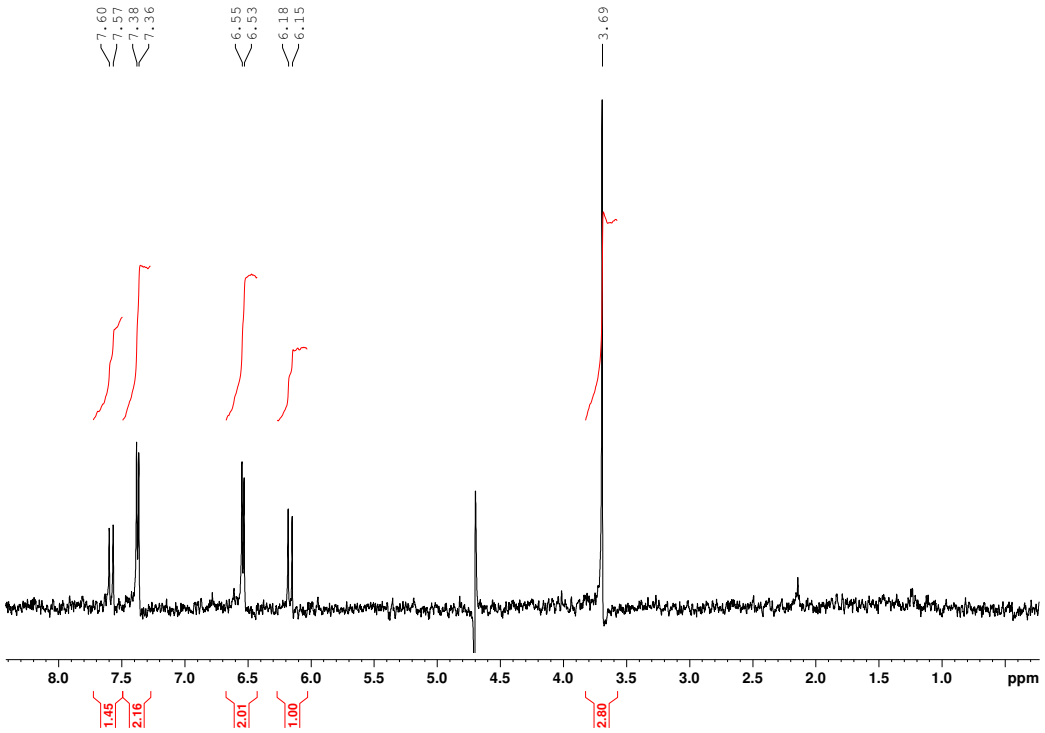

Figure A.1: ^{1}H NMR spectrum (500 MHz, D_2O) of 50 µM *p*CE in 1.25 mM NaOD. The contribution from H_2O, HDO and OD^- has been subtracted.

^{1}H NMR (500 MHz, D_2O) of 50 µM *p*CE in 1.25 mM NaOD: δ 7.58 (d, J = 15.8 Hz, 1H), 7.37 (d, J = 8.6 Hz, 2H), 6.54 (d, J = 8.5 Hz, 2H), 6.16 (d, J = 15.8 Hz, 1H), 3.69 (s, 3H).

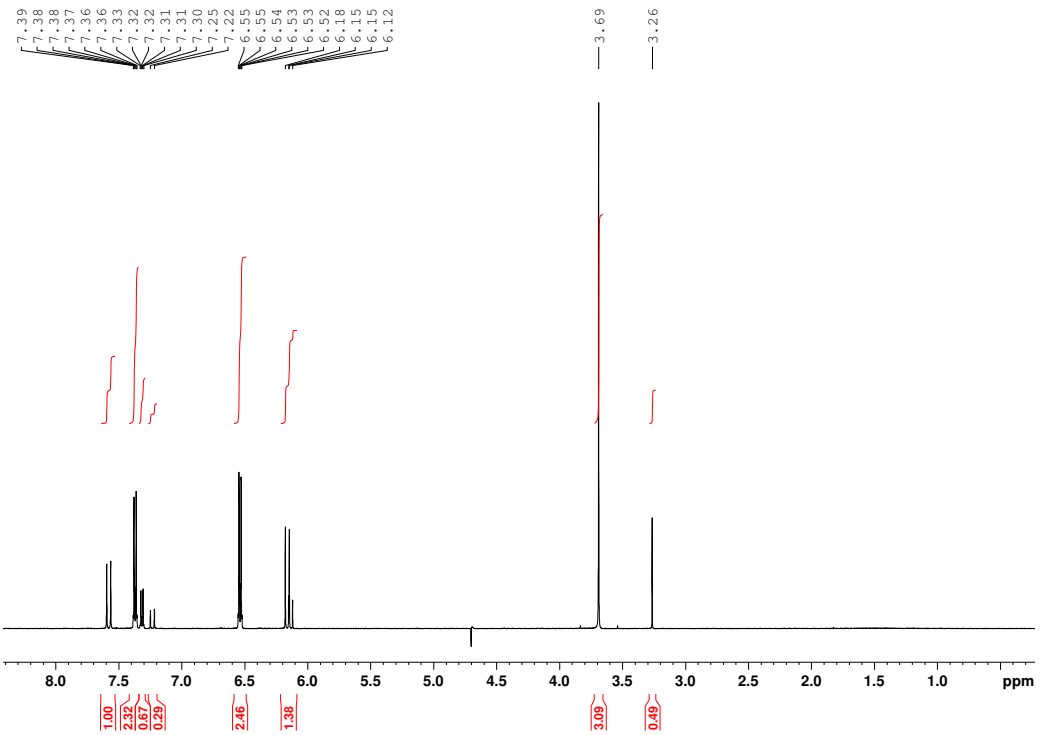

Figure A.2: ^{1}H NMR spectrum (500 MHz, D_2O) of 5 mM *p*CE in 5.5 mM NaOD. The contribution from H_2O, HDO and OD^- has been subtracted.

^{1}H NMR (500 MHz, D_2O) of 5 mM *p*CE in 5.5 mM NaOD: *p*CE^- δ 7.58 (d, J = 15.9 Hz, 1H), 7.37 (ddd, J = 8.7 Hz, 2H), 6.54 (d, J = 15.5 Hz, 2H), 6.16 (d, J = 15.9 Hz, 1H), 3.69 (s, 3H); *p*CA^{2-} δ 7.32 (ddd, J = 8.7 Hz, 2H), 7.23 (d, J = 15.9 Hz, 1H), 6.14 (d, J = 15.9 Hz, 1H), 3.26 (s, 3H); MeOH δ 3.26 (s, 3H).

A.2 X-ray photoelectron spectra

A.2.1 Full spectrum fits with literature constrained water peaks

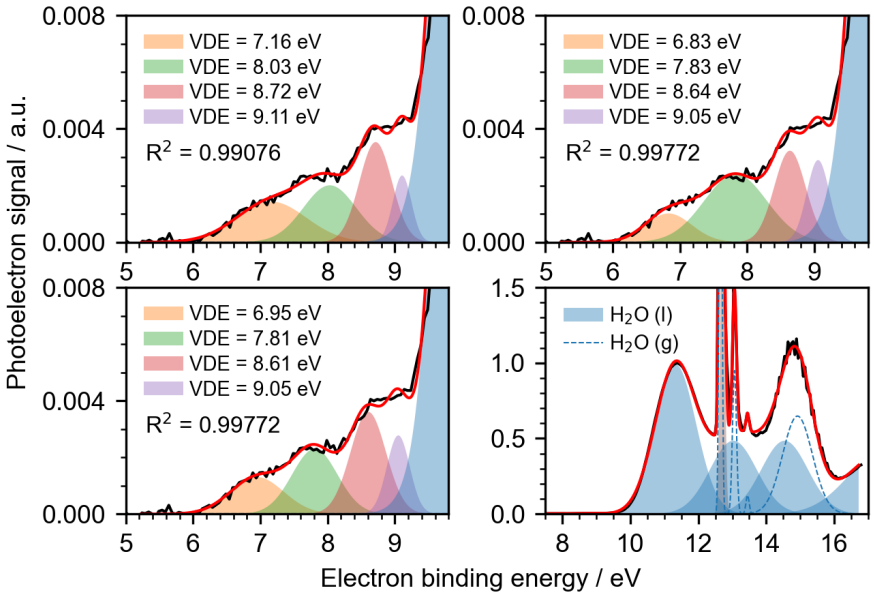

Figure A.3: Possible fits of the X-ray ($h\nu$ = 180 eV) photoelectron spectrum of 5 mM *p*CE in aqueous solution with 5.5 mM NaOH and 30 mM NaF, in which the widths and relative positions of the liquid water Gaussians were constrained to literature values.[42,144] The parameters of the gaseous water and $p\mathrm{CE}^-$ Gaussians were not constrained. The eKE was calibrated to the $1b_1$ peak of water which was set to 11.33 eV.[42] The fits are sensitive to the initial guess and several sets of parameters describe the contribution of $p\mathrm{CE}^-$ adequately. The parameters describing liquid and gaseous water are virtually unaffected. Experimental spectrum reproduced from Ref. 138.

A.2.2 Full and subtracted spectrum fits with free water peaks

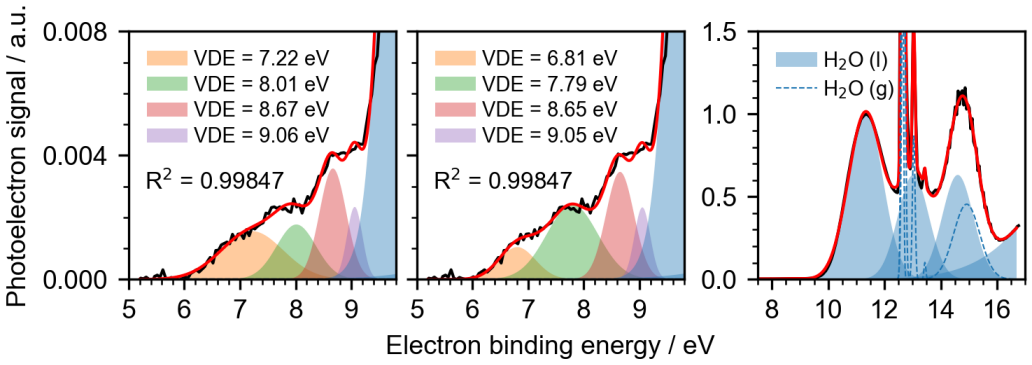

Figure A.4: Possible fits of the X-ray ($h\nu$ = 180 eV) photoelectron spectrum of 5 mM *p*CE in aqueous solution with 5.5 mM NaOH and 30 mM NaF, in which the only widths and relative intensities of the $3a_1$ liquid water Gaussians were constrained to be the same.[42] The parameters of the other peaks were free. The eKE was calibrated to the $1b_1$ peak of water which was set to 11.33 eV.[42] The fits are sensitive to the initial guess and several sets of parameters describe the contribution of *p*CE$^-$ adequately. The parameters describing liquid and gaseous water are virtually unaffected. Experimental spectrum reproduced from Ref. 138.

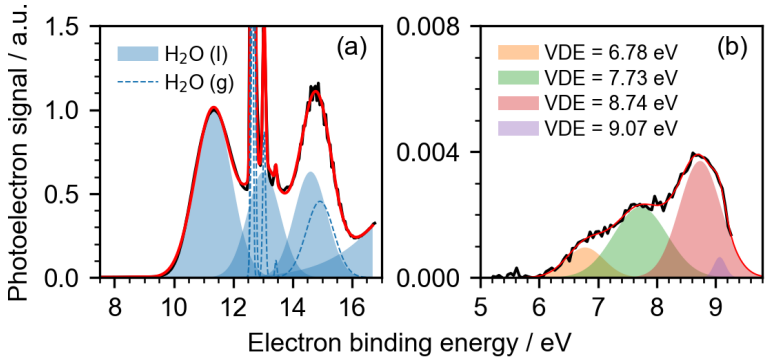

Figure A.5: X-ray photoelectron spectrum of 5 mM *p*CE in aqueous solution with 5.5 mM NaOH and 30 mM NaF recorded with a photon energy of 180 eV. (a) The spectrum was fit as a sum of Gaussians representing photoionisation of liquid and gaseous water and photodetachment of $p\text{CE}^-$ and a vertical offset to capture the baseline noise. The widths and relative intensities of the $3a_1$ liquid water Gaussians were constrained to be the same.[42] The parameters of the other peaks were free. The eKE was calibrated to the $1b_1$ peak of water which was set to 11.33 eV.[42] (b) The water contribution to the spectrum was subtracted and the signal below 9.35 eV (black line) was fit with four Gaussians. The spectrum without subtraction is shown in gray. The obtained VDEs of $p\text{CE}^-$ are in excellent agreement with those obtained from constraining the liquid water Gaussians to the literature values (Figure 4.8 in Chapter 4). b Experimental spectrum reproduced from Ref. 138.

A.2.3 Effect of cutoff on the subtracted spectrum fits

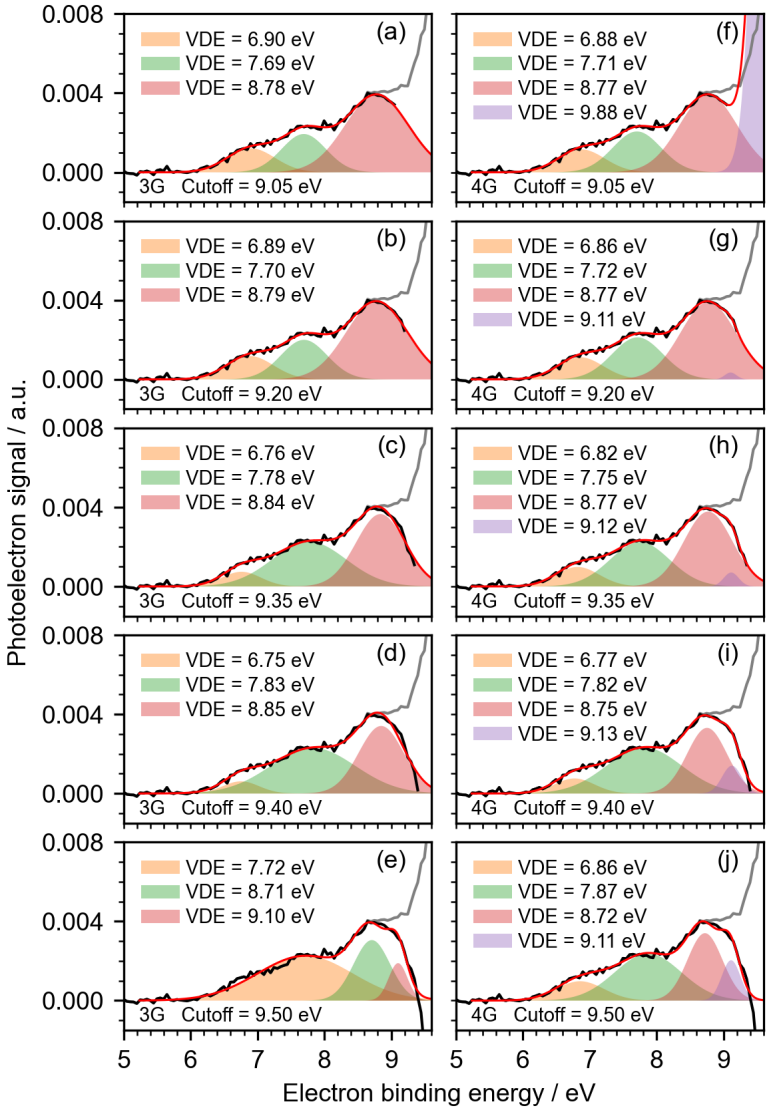

Figure A.6: Effect of the high eBE cutoff on the fits of the X-ray ($h\nu = 180$ eV) photoelectron spectrum of 5 mM *p*CE in aqueous solution with 5.5 mM NaOH and 30 mM NaF from which the water contribution was subtracted. Left: three Gaussians were employed. Gray lines represent the measured spectrum, black lines represent the subtracted spectrum below the cutoff, and red lines represent the fits. Right: four Gaussians were employed. Each row corresponds to a different cutoff value, shown in increasing order from top to bottom: 9.05, 9.20, 9.35, 9.40, and 9.50 eV. Experimental spectrum reproduced from Ref. 138.

Appendix B

Supporting information: Time-resolved photoelectron spectroscopy of the photoactive yellow protein chromophore in aqueous solution

B.1 UV-Vis spectra of pCE$^-$ in H_2O and D_2O

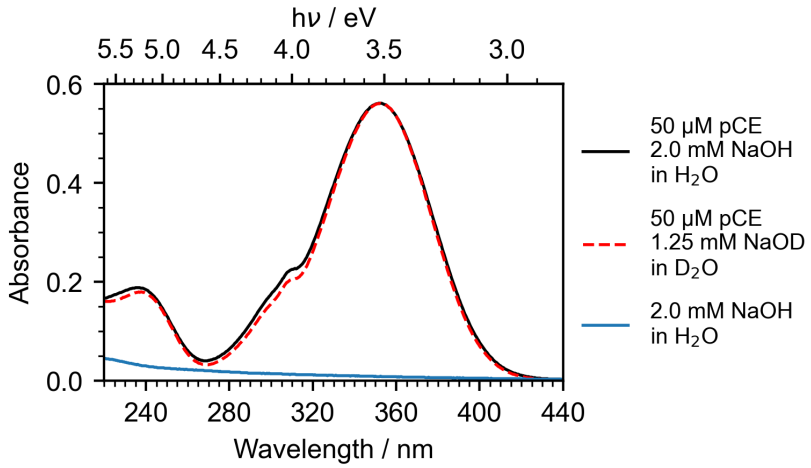

Figure B.1: UV-Vis spectra of 50 µM pCE in 2.0 mM aqueousNaOH (solid black line), and 50 µM pCE in 1.25 mM NaOD in D_2O (dashed red line). As no background spectrum of NaOD in D_2O was recorded, the pCE$^-$ spectra are not subtracted and the UV-Vis spectrum of 2.0 mM aqueous NaOH is shown in blue. Spectra were recorded with a 4 mm path length.

B.2 Residuals

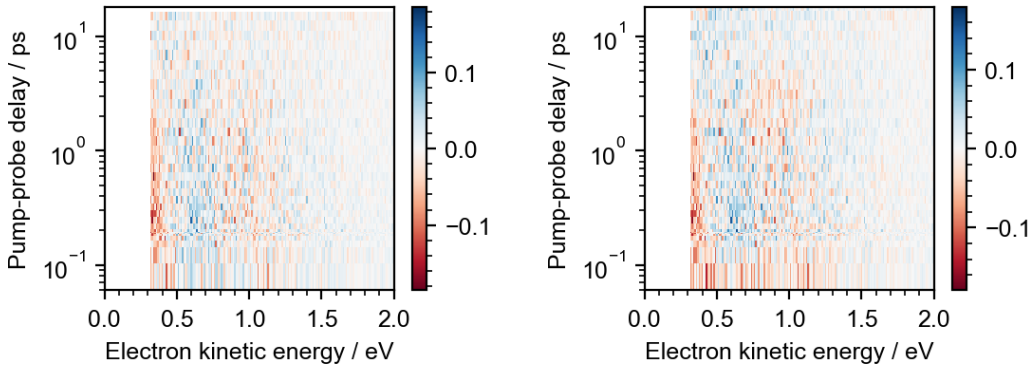

Figure B.2: Left: residuals of the single Gaussian fit of the TR spectra of pCE$^-$ in H_2O in Figure 5.4b. Right: residuals of the two Gaussian fit of the TR spectra of pCE$^-$ in H_2Oin Figure 5.9

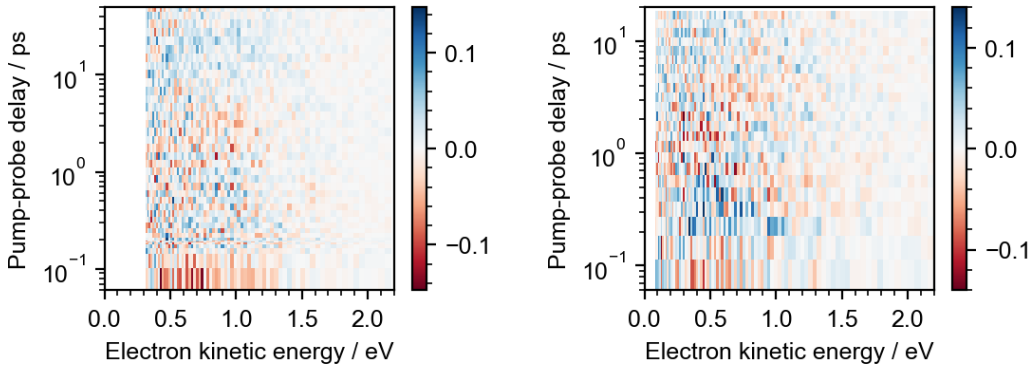

Figure B.3: Left: residuals of the DAS/EAS fit of the TR spectra of pCE$^-$ in H_2O in Figure 5.8. Right: Residuals of the DAS/EAS fit of the TR spectra of pCE$^-$ in D_2O in Figure 5.15.

Bibliography

[1] Hertz, H. Ueber sehr schnelle electrische Schwingungen. *Annalen der Physik* **1887**, *267*, 421–448.

[2] Jenkin, J. G.; Leckey, R. C.; Liesegang, J. The development of x-ray photoelectron spectroscopy: 1900-1960. *Journal of Electron Spectroscopy and Related Phenomena* **1977**, *12*, 1–35.

[3] Einstein, A. Über einen die Erzeugung und Verwandlung des Lichtes betreffenden heuristischen Gesichtspunkt. *Annalen der Physik* **1905**, *322*, 132–148.

[4] Koopmans, T. Über die Zuordnung von Wellenfunktionen und Eigenwerten zu den Einzelnen Elektronen Eines Atoms. *Physica* **1934**, *1*, 104–113.

[5] Richards, W. The use of Koopmans' Theorem in the interpretation of photoelectron spectra. *International Journal of Mass Spectrometry and Ion Physics* **1969**, *2*, 419–424.

[6] Greczynski, G.; Hultman, L. X-ray photoelectron spectroscopy: Towards reliable binding energy referencing. *Progress in Materials Science* **2020**, *107*, 100591.

[7] Baer, D. R.; Sherwood, P. M. A. Perspective on the development of XPS and the pioneers who made it possible. *Frontiers in Analytical Science* **2025**, *4*, 1–10.

[8] Siegbahn, K. Electron spectroscopy for atoms, molecules, and condensed matter. *Reviews of Modern Physics* **1982**, *54*, 709–728.

[9] Turner, D. W.; Baker, C.; Baker, A. D.; Brundle, C. R. *Molecular photoelectron spectroscopy: a handbook of He 584 A spectra*; Wiley-Interscience: London, New York, 1970.

[10] Seidel, R.; Winter, B.; Bradforth, S. E. Valence Electronic Structure of Aqueous Solutions: Insights from Photoelectron Spectroscopy. *Annual Review of Physical Chemistry* **2016**, *67*, 283–305.

[11] Fielding, H. H.; Worth, G. A. Using time-resolved photoelectron spectroscopy to unravel the electronic relaxation dynamics of photoexcited molecules. *Chemical Society Reviews* **2018**, *47*, 309–321.

[12] Stevie, F. A.; Donley, C. L. Introduction to x-ray photoelectron spectroscopy. *Journal of Vacuum Science & Technology A: Vacuum, Surfaces, and Films* **2020**, *38*.

[13] Suzuki, T. Time-resolved photoelectron spectroscopy of non-adiabatic electronic dynamics in gas and liquid phases. *International Reviews in Physical Chemistry* **2012**, *31*, 265–318.

[14] Reid, K. L. Photoelectron Angular Distributions. *Annual Review of Physical Chemistry* **2003**, *54*, 397–424.

[15] Stolow, A.; Underwood, J. G. *Time-Resolved Photoelectron Spectroscopy of Nonadiabatic Dynamics in Polyatomic Molecules*; 2008; pp 497–584.

[16] Spesyvtsev, R.; Underwood, J. G.; Fielding, H. H. *Time-Resolved Photoelectron Spectroscopy for Excited State Dynamics*; 2014; pp 99–117.

[17] Seah, M. P.; Dench, W. A. Quantitative electron spectroscopy of surfaces: A standard data base for electron inelastic mean free paths in solids. *Surface and Interface Analysis* **1979**, *1*, 2–11.

[18] Siegbahn, H. Electron spectroscopy for chemical analysis of liquids and solutions. *The Journal of Physical Chemistry* **1985**, *89*, 897–909.

[19] Siegbahn, H.; Siegbahn, K. ESCA applied to liquids. *Journal of Electron Spectroscopy and Related Phenomena* **1973**, *2*, 319–325.

[20] Winter, B.; Faubel, M. Photoemission from Liquid Aqueous Solutions. *Chemical Reviews* **2006**, *106*, 1176–1211.

[21] Lundholm, M.; Siegbahn, H.; Holmberg, S.; Arbman, M. Core electron spectroscopy of water solutions. *Journal of Electron Spectroscopy and Related Phenomena* **1986**, *40*, 163–180.

[22] Faubel, M.; Schlemmer, S.; Toennies, J. P. A molecular beam study of the evaporation of water from a liquid jet. *Zeitschrift für Physik D Atoms, Molecules and Clusters* **1988**, *10*, 269–277.

[23] Suzuki, T. Ultrafast photoelectron spectroscopy of aqueous solutions. *The Journal of Chemical Physics* **2019**, *151*, 090901.

[24] Knudsen, M. Die Gesetze der Molekularströmung und der inneren Reibungsströmung der Gase durch Röhren. *Annalen der Physik* **1909**, *333*, 75–130.

[25] Gad-El-Hak, M. The fluid mechanics of microdevices—the freeman scholar lecture. *Journal of Fluids Engineering, Transactions of the ASME* **1999**, *121*, 5–33.

[26] Faubel, M.; Steiner, B.; Toennies, J. P. Photoelectron spectroscopy of liquid water, some alcohols, and pure nonane in free micro jets. *The Journal of Chemical Physics* **1997**, *106*, 9013–9031.

[27] Winter, B.; Weber, R.; Widdra, W.; Dittmar, M.; Faubel, M.; Hertel, I. V. Full Valence Band Photoemission from Liquid Water Using EUV Synchrotron Radiation. *Journal of Physical Chemistry A* **2004**, *108*, 2625–2632.

[28] Winter, B.; Aziz, E. F.; Hergenhahn, U.; Faubel, M.; Hertel, I. V. Hydrogen bonds in liquid water studied by photoelectron spectroscopy. *The Journal of chemical physics* **2007**, *126*, 124504.

[29] Faubel, M.; Steiner, B.; Toennies, J. P. Photoelectron spectroscopy of liquid water, some alcohols, and pure nonane in free micro jets. *Journal of Chemical Physics* **1997**, *106*, 9013–9031.

[30] Winter, B.; Weber, R.; Hertel, I. V.; Faubel, M.; Jungwirth, P.; Brown, E. C.; Bradforth, S. E. Electron binding energies of aqueous alkali and halide ions: EUV photoelectron spectroscopy of liquid solutions and combined Ab initio and molecular dynamics calculations. *Journal of the American Chemical Society* **2005**, *127*, 7203–7214.

[31] Kurahashi, N.; Karashima, S.; Tang, Y.; Horio, T.; Abulimiti, B.; Suzuki, Y.-I.; Ogi, Y.; Oura, M.; Suzuki, T. Photoelectron spectroscopy of aqueous solutions: Streaming potentials of NaX (X = Cl, Br, and I) solutions and electron binding energies of liquid water and X-. *The Journal of Chemical Physics* **2014**, *140*, 174506.

[32] Winter, B.; Faubel, M.; Vácha, R.; Jungwirth, P. Behavior of hydroxide at the water/vapor interface. *Chemical Physics Letters* **2009**, *474*, 241–247.

[33] Pluhařová, E.; Ončák, M.; Seidel, R.; Schroeder, C.; Schroeder, W.; Winter, B.; Bradforth, S. E.; Jungwirth, P.; Slavíček, P. Transforming anion instability into stability: Contrasting photoionization of three protonation forms of the phosphate ion upon moving into water. *Journal of Physical Chemistry B* **2012**, *116*, 13254–13264.

[34] Seidel, R.; Faubel, M.; Winter, B.; Blumberger, J. Single-ion reorganization free energy of aqueous Ru(bpy)32+/3+ and Ru(H2O)62+/3+ from photoemission spectroscopy and density functional molecular dy-

namics simulation. *Journal of the American Chemical Society* **2009**, *131*, 16127–16137.

[35] Moens, J.; Seidel, R.; Geerlings, P.; Faubel, M.; Winter, B.; Blumberger, J. Energy levels and redox properties of aqueous Mn2+/3+ from photoemission spectroscopy and density functional molecular dynamics simulation. *Journal of Physical Chemistry B* **2010**, *114*, 9173–9182.

[36] Seidel, R.; Thürmer, S.; Moens, J.; Geerlings, P.; Blumberger, J.; Winter, B. Valence photoemission spectra of aqueous Fe2+/3+ and [Fe(CN)6]4-/3- and their interpretation by DFT calculations. *Journal of Physical Chemistry B* **2011**, *115*, 11671–11677.

[37] Makowski, M. J.; Galhenage, R. P.; Langford, J.; Hemminger, J. C. Liquid-Jet X-ray Photoelectron Spectra of TiO2 Nanoparticles in an Aqueous Electrolyte Solution. *Journal of Physical Chemistry Letters* **2016**, *7*, 1732–1735.

[38] Faubel, M.; Steiner, B. Strong Bipolar Electrokinetic Charging of Thin Liquid Jets Emerging from 10 μm PtIr Nozzles. *Berichte der Bunsengesellschaft für physikalische Chemie* **1992**, *96*, 1167–1172.

[39] Preissler, N.; Buchner, F.; Schultz, T.; Lübcke, A. Electrokinetic Charging and Evidence for Charge Evaporation in Liquid Microjets of Aqueous Salt Solution. *The Journal of Physical Chemistry B* **2013**, *117*, 2422–2428.

[40] Nishitani, J.; Karashima, S.; West, C. W.; Suzuki, T. Surface potential of liquid microjet investigated using extreme ultraviolet photoelectron spectroscopy. *Journal of Chemical Physics* **2020**, *152*, 144503.

[41] Riley, J. W.; Wang, B.; Parkes, M. A.; Fielding, H. H. Design and characterization of a recirculating liquid-microjet photoelectron spectrometer for multiphoton ultraviolet photoelectron spectroscopy. *Review of Scientific Instruments* **2019**, *90*, 083104.

[42] Thürmer, S.; Malerz, S.; Trinter, F.; Hergenhahn, U.; Lee, C.; Neumark, D. M.; Meijer, G.; Winter, B.; Wilkinson, I. Accurate vertical ionization energy and work function determinations of liquid water and aqueous solutions. *Chemical Science* **2021**, *12*, 10558–10582.

[43] Nishizawa, K.; Kurahashi, N.; Sekiguchi, K.; Mizuno, T.; Ogi, Y.; Horio, T.; Oura, M.; Kosugi, N.; Suzuki, T. High-resolution soft X-ray photoelectron spectroscopy of liquid water. *Physical Chemistry Chemical Physics* **2011**, *13*, 413–417.

[44] Winter, B.; Thürmer, S.; Wilkinson, I. Absolute Electronic Energetics and Quantitative Work Functions of Liquids from Photoelectron Spectroscopy. *Accounts of Chemical Research* **2023**, *56*, 77–85.

[45] Michaud, M.; Wen, A.; Sanche, L. Cross sections for low-energy (1-100 eV) electron elastic and inelastic scattering in amorphous ice. *Radiation Research* **2003**, *159*, 3–22.

[46] Ottosson, N.; Faubel, M.; Bradforth, S. E.; Jungwirth, P.; Winter, B. Photoelectron spectroscopy of liquid water and aqueous solution: Electron effective attenuation lengths and emission-angle anisotropy. *Journal of Electron Spectroscopy and Related Phenomena* **2010**, *177*, 60–70.

[47] Thürmer, S.; Seidel, R.; Faubel, M.; Eberhardt, W.; Hemminger, J. C.; Bradforth, S. E.; Winter, B. Photoelectron Angular Distributions from Liquid Water: Effects of Electron Scattering. *Physical Review Letters* **2013**, *111*, 173005.

[48] Suzuki, Y.-I.; Nishizawa, K.; Kurahashi, N.; Suzuki, T. Effective attenuation length of an electron in liquid water between 10 and 600 eV. *Physical Review E* **2014**, *90*, 010302.

[49] Signorell, R. Electron Scattering in Liquid Water and Amorphous Ice: A Striking Resemblance. *Physical Review Letters* **2020**, *124*, 205501.

[50] Signorell, R.; Goldmann, M.; Yoder, B. L.; Bodi, A.; Chasovskikh, E.; Lang, L.; Luckhaus, D. Nanofocusing, shadowing, and electron mean free path in the photoemission from aerosol droplets. *Chemical Physics Letters* **2016**, *658*, 1–6.

[51] Luckhaus, D.; Yamamoto, Y.-i.; Suzuki, T.; Signorell, R. Genuine binding energy of the hydrated electron. *Science Advances* **2017**, *3*, e1603224.

[52] Nolting, D.; Ottosson, N.; Faubel, M.; Hertel, I. V.; Winter, B. Pseudoequivalent nitrogen atoms in aqueous imidazole distinguished by chemical shifts in photoelectron spectroscopy. *Journal of the American Chemical Society* **2008**, *130*, 8150–8151.

[53] Roy, A.; Seidel, R.; Kumar, G.; Bradforth, S. E. Exploring Redox Properties of Aromatic Amino Acids in Water: Contrasting Single Photon vs Resonant Multiphoton Ionization in Aqueous Solutions. *Journal of Physical Chemistry B* **2018**, *122*, 3723–3733.

[54] Richter, C.; Dupuy, R.; Trinter, F.; Buttersack, T.; Cablitz, L.; Gholami, S.; Stemer, D.; Nicolas, C.; Seidel, R.; Winter, B.; Bluhm, H. Surface accumulation and acid–base equilibrium of phenol at the liquid–vapor interface. *Physical Chemistry Chemical Physics* **2024**, *26*, 27292–27300.

[55] Malerz, S.; Mudryk, K.; Tomaník, L.; Stemer, D.; Hergenhahn, U.; Buttersack, T.; Trinter, F.; Seidel, R.; Quevedo, W.; Goy, C.; Wilkinson, I.; Thürmer, S.; Slavíček, P.; Winter, B. Following in Emil Fischer's Footsteps: A Site-Selective Probe of Glucose Acid-Base Chemistry. *Journal of Physical Chemistry A* **2021**, *125*, 6881–6892.

[56] Buchner, F.; Nakayama, A.; Yamazaki, S.; Ritze, H. H.; Lübcke, A. Excited-state relaxation of hydrated thymine and thymidine measured by liquid-jet photoelectron spectroscopy: Experiment and simulation. *Journal of the American Chemical Society* **2015**, *137*, 2931–2938.

[57] Erickson, B. A.; Heim, Z. N.; Pieri, E.; Liu, E.; Martinez, T. J.; Neumark, D. M. Relaxation Dynamics of Hydrated Thymine, Thymidine, and Thymidine Monophosphate Probed by Liquid Jet Time-Resolved Photoelectron Spectroscopy. *The Journal of Physical Chemistry A* **2019**, *123*, 10676–10684.

[58] Mudryk, K.; Lee, C.; Tomaník, L.; Malerz, S.; Trinter, F.; Hergenhahn, U.; Neumark, D. M.; Slavíček, P.; Bradforth, S.; Winter, B. How Does Mg 2+ (aq) Interact with ATP (aq) ? Biomolecular Structure through the Lens of Liquid-Jet Photoemission Spectroscopy. *Journal of the American Chemical Society* **2024**,

[59] Williams, H. L.; Erickson, B. A.; Neumark, D. M. Time-resolved photoelectron spectroscopy of adenosine and adenosine monophosphate photodeactivation dynamics in water microjets. *Journal of Chemical Physics* **2018**, *148*.

[60] Schroeder, C. A.; Pluharová, E.; Seidel, R.; Schroeder, W. P.; Faubel, M.; Slavíçek, P.; Winter, B.; Jungwirth, P.; Bradforth, S. E. Oxidation half-reaction of aqueous nucleosides and nucleotides via photoelectron spectroscopy augmented by ab initio calculations. *Journal of the American Chemical Society* **2015**, *137*, 201–209.

[61] Buchner, F.; Ritze, H. H.; Lahl, J.; Lübcke, A. Time-resolved photoelectron spectroscopy of adenine and adenosine in aqueous solution. *Physical Chemistry Chemical Physics* **2013**, *15*, 11402–11408.

[62] Riley, J. W.; Wang, B.; Woodhouse, J. L.; Assmann, M.; Worth, G. A.; Fielding, H. H. Unravelling the Role of an Aqueous Environment on the Electronic Structure and Ionization of Phenol Using Photoelectron Spectroscopy. *Journal of Physical Chemistry Letters* **2018**, *9*, 678–682.

[63] West, C. W.; Nishitani, J.; Higashimura, C.; Suzuki, T. Extreme ultraviolet time-resolved photoelectron spectroscopy of aqueous aniline solu-

tion: enhanced surface concentration and pump-induced space charge effect. *Molecular Physics* **2021**, *119*.

[64] Tau, O.; Henley, A.; Boichenko, A. N.; Kleshchina, N. N.; Riley, R.; Wang, B.; Winning, D.; Lewin, R.; Parkin, I. P.; Ward, J. M.; Hailes, H. C.; Bochenkova, A. V.; Fielding, H. H. Liquid-microjet photoelectron spectroscopy of the green fluorescent protein chromophore. *Nature Communications* **2022**, *13*, 507.

[65] Roy, A.; Seidel, R.; Kumar, G.; Bradforth, S. E. Exploring Redox Properties of Aromatic Amino Acids in Water: Contrasting Single Photon vs Resonant Multiphoton Ionization in Aqueous Solutions. *Journal of Physical Chemistry B* **2018**, *122*, 3723–3733.

[66] Fortune, W. G.; Scholz, M. S.; Fielding, H. H. UV Photoelectron Spectroscopy of Aqueous Solutions. *Accounts of Chemical Research* **2022**, *55*, 3631–3640.

[67] Kumar, G.; Roy, A.; McMullen, R. S.; Kutagulla, S.; Bradforth, S. E. The influence of aqueous solvent on the electronic structure and non-adiabatic dynamics of indole explored by liquid-jet photoelectron spectroscopy. *Faraday Discussions* **2018**, *212*, 359–381.

[68] Shreve, A. T.; Yen, T. A.; Neumark, D. M. Photoelectron spectroscopy of hydrated electrons. *Chemical Physics Letters* **2010**, *493*, 216–219.

[69] Lübcke, A.; Buchner, F.; Heine, N.; Hertel, I. V.; Schultz, T. Time-resolved photoelectron spectroscopy of solvated electrons in aqueous NaI solution. *Physical Chemistry Chemical Physics* **2010**, *12*, 14629.

[70] Tang, Y.; Shen, H.; Sekiguchi, K.; Kurahashi, N.; Mizuno, T.; Suzuki, Y.-I.; Suzuki, T. Direct measurement of vertical binding energy of a hydrated electron. *Physical Chemistry Chemical Physics* **2010**, *12*, 3653.

[71] Malerz, S. et al. Low-energy constraints on photoelectron spectra measured from liquid water and aqueous solutions. *Physical Chemistry Chemical Physics* **2021**, *23*, 8246–8260.

[72] Thürmer, S.; Stemer, D.; Trinter, F.; Kiyan, I. Y.; Winter, B.; Wilkinson, I. Low-Energy Photoelectron Spectroscopy and Scattering from Aqueous Solutions and the Role of Solute Surface Activity. *Journal of the American Chemical Society* **2025**,

[73] Siefermann, K. R.; Liu, Y.; Lugovoy, E.; Link, O.; Faubel, M.; Buck, U.; Winter, B.; Abel, B. Binding energies, lifetimes and implications of bulk and interface solvated electrons in water. *Nature Chemistry* **2010**, *2*, 274–279.

[74] Buchner, F.; Schultz, T.; Lübcke, A. Solvated electrons at the water–air interface: surface versus bulk signal in low kinetic energy photoelectron spectroscopy. *Physical Chemistry Chemical Physics* **2012**, *14*, 5837.

[75] Horio, T.; Shen, H.; Adachi, S.; Suzuki, T. Photoelectron spectra of solvated electrons in bulk water, methanol, and ethanol. *Chemical Physics Letters* **2012**, *535*, 12–16.

[76] Yamamoto, Y.-i.; Karashima, S.; Adachi, S.; Suzuki, T. Wavelength Dependence of UV Photoemission from Solvated Electrons in Bulk Water, Methanol, and Ethanol. *The Journal of Physical Chemistry A* **2016**, *120*, 1153–1159.

[77] Yamamoto, Y.-I.; Suzuki, T. Distortion Correction of Low-Energy Photoelectron Spectra of Liquids Using Spectroscopic Data for Solvated Electrons. *The Journal of Physical Chemistry A* **2023**, *127*, 2440–2452.

[78] Nishitani, J.; Yamamoto, Y.-i.; West, C. W.; Karashima, S.; Suzuki, T. Binding energy of solvated electrons and retrieval of true UV photoelectron spectra of liquids. *Science Advances* **2019**, *5*, eaaw6896.

[79] Scholz, M. S.; Fortune, W. G.; Tau, O.; Fielding, H. H. Accurate Vertical Ionization Energy of Water and Retrieval of True Ultraviolet Photoelectron Spectra of Aqueous Solutions. *The Journal of Physical Chemistry Letters* **2022**, *13*, 6889–6895.

[80] Gadeyne, T.; Zhang, P.; Schild, A.; Wörner, H. J. Low-energy electron distributions from the photoionization of liquid water: a sensitive test of electron mean free paths. *Chemical Science* **2022**, *13*, 1675–1692.

[81] Bartels, D. M. Is the hydrated electron vertical detachment genuinely bimodal? *Journal of Physical Chemistry Letters* **2019**, *10*, 4910–4913.

[82] Gaiduk, A. P.; Pham, T. A.; Govoni, M.; Paesani, F.; Galli, G. Electron affinity of liquid water. *Nature Communications* **2018**, *9*, 4–9.

[83] Jarvis, G. K.; Evans, M.; Ng, C. Y.; Mitsuke, K. Rotational-resolved pulsed field ionization photoelectron study of NO+(X 1Σ+,v+=0–32) in the energy range of 9.24–16.80 eV. *The Journal of Chemical Physics* **1999**, *111*, 3058–3069.

[84] Sansonetti, J. E.; Martin, W. C. Handbook of Basic Atomic Spectroscopic Data. *Journal of Physical and Chemical Reference Data* **2005**, *34*, 1559–2259.

[85] Lis, D.; Backus, E. H. G.; Hunger, J.; Parekh, S. H.; Bonn, M. Liquid flow along a solid surface reversibly alters interfacial chemistry. *Science* **2014**, *344*, 1138–1142.

[86] Coreño, J.; Martínez, A.; Bolarín, A.; Sánchez, F. Apatite nucleation on silica surface: A ζ potential approach. *Journal of Biomedical Materials Research* **2001**, *57*, 119–125.

[87] Signorell, R.; Winter, B. Photoionization of the aqueous phase: clusters, droplets and liquid jets. *Physical Chemistry Chemical Physics* **2022**, *24*, 13438–13460.

[88] Titov, E.; Hummert, J.; Ikonnikov, E.; Mitrić, R.; Kornilov, O. Electronic relaxation of aqueous aminoazobenzenes studied by time-resolved photoelectron spectroscopy and surface hopping TDDFT dynamics calculations. *Faraday Discussions* **2021**, *228*, 226–241.

[89] Wang, C.; Waters, M. D.; Zhang, P.; Suchan, J.; Svoboda, V.; Luu, T. T.; Perry, C.; Yin, Z.; Slavíček, P.; Wörner, H. J. Different timescales during ultrafast stilbene isomerization in the gas and liquid phases revealed using time-resolved photoelectron spectroscopy. *Nature Chemistry* **2022**, *14*, 1126–1132.

[90] Miura, Y.; Yamamoto, Y. I.; Karashima, S.; Orimo, N.; Hara, A.; Fukuoka, K.; Ishiyama, T.; Suzuki, T. Formation of Long-Lived Dark States during Electronic Relaxation of Pyrimidine Nucleobases Studied Using Extreme Ultraviolet Time-Resolved Photoelectron Spectroscopy. *Journal of the American Chemical Society* **2023**, *145*, 3369–3381.

[91] No Title. https://github.com/FieldingGroup/LJscatter.

[92] Simonetti, E.; Fielding, H. H. Retrieval of Genuine Ultraviolet Liquid-Microjet Photoelectron Spectra. *Journal of Physical Chemistry A* **2025**, *129*, 5292–5299.

[93] Atkins, P.; De Paula, J. *Atkins' physical chemistry*, tenth ed.; Oxford University Press, 2014; pp 37–44.

[94] Eastman, P.; Swails, J.; Chodera, J. D.; McGibbon, R. T.; Zhao, Y.; Beauchamp, K. A.; Wang, L.-P.; Simmonett, A. C.; Harrigan, M. P.; Stern, C. D.; Wiewiora, R. P.; Brooks, B. R.; Pande, V. S. OpenMM 7: Rapid development of high performance algorithms for molecular dynamics. *PLOS Computational Biology* **2017**, *13*, e1005659.

[95] Malde, A. K.; Zuo, L.; Breeze, M.; Stroet, M.; Poger, D.; Nair, P. C.; Oostenbrink, C.; Mark, A. E. An Automated Force Field Topology

Builder (ATB) and Repository: Version 1.0. *Journal of Chemical Theory and Computation* **2011**, *7*, 4026–4037.

[96] Stroet, M.; Caron, B.; Visscher, K. M.; Geerke, D. P.; Malde, A. K.; Mark, A. E. Automated Topology Builder Version 3.0: Prediction of Solvation Free Enthalpies in Water and Hexane. *Journal of Chemical Theory and Computation* **2018**, *14*, 5834–5845.

[97] Mobley, D. L.; Bannan, C. C.; Rizzi, A.; Bayly, C. I.; Chodera, J. D.; Lim, V. T.; Lim, N. M.; Beauchamp, K. A.; Slochower, D. R.; Shirts, M. R.; Gilson, M. K.; Eastman, P. K. Escaping Atom Types in Force Fields Using Direct Chemical Perception. *Journal of Chemical Theory and Computation* **2018**, *14*, 6076–6092.

[98] Jorgensen, W. L.; Chandrasekhar, J.; Madura, J. D.; Impey, R. W.; Klein, M. L. Comparison of simple potential functions for simulating liquid water. *The Journal of Chemical Physics* **1983**, *79*, 926–935.

[99] Zhang, Z.; Liu, X.; Yan, K.; Tuckerman, M. E.; Liu, J. Unified Efficient Thermostat Scheme for the Canonical Ensemble with Holonomic or Isokinetic Constraints via Molecular Dynamics. *The Journal of Physical Chemistry A* **2019**, *123*, 6056–6079.

[100] Goulet, T.; Jay-Gerin, J.-P.; Patau, J.-P. Monte carlo simulations of low-energy (¡10eV) electron transmission and reflection experiments: application to solid xenon. *Journal of Electron Spectroscopy and Related Phenomena* **1987**, *43*, 17–35.

[101] Yamamoto, Y.-i.; Hirano, T.; Ishiyama, T.; Morita, A.; Suzuki, T. Gas–Liquid Interface of Aqueous Solutions of Surface Active Aromatic Molecules Studied Using Extreme Ultraviolet Laser Photoelectron Spectroscopy and Molecular Dynamics Simulation. *Journal of the American Chemical Society* **2025**, *147*, 4026–4037.

[102] Ghosh, D.; Roy, A.; Seidel, R.; Winter, B.; Bradforth, S.; Krylov, A. I. First-principle protocol for calculating ionization energies and redox potentials of solvated molecules and ions: Theory and application to aqueous phenol and phenolate. *Journal of Physical Chemistry B* **2012**, *116*, 7269–7280.

[103] Heitland, J.; Lee, J. C.; Ban, L.; Abma, G. L.; Fortune, W. G.; Fielding, H. H.; Yoder, B. L.; Signorell, R. Valence Electronic Structure of Interfacial Phenol in Water Droplets. *Journal of Physical Chemistry A* **2024**, *128*, 7396–7406.

[104] Borgstahl, G. E. O.; Williams, D. R.; Getzoff, E. D. Å Structure of Photoactive Yellow Protein, a Cytosolic Photoreceptor: Unusual Fold, Active Site, and Chromophore. *Biochemistry* **1995**, *34*, 6278–6287.

[105] Hellingwerf, K. J.; Hendriks, J.; Gensch, T. Photoactive yellow protein, a new type of photoreceptor protein: Will this "yellow lab" bring us where we want to go? *Journal of Physical Chemistry A* **2003**, *107*, 1082–1094.

[106] Jung, Y. O.; Lee, J. H.; Kim, J.; Schmidt, M.; Moffat, K.; Šrajer, V.; Ihee, H. Volume-conserving trans-cis isomerization pathways in photoactive yellow protein visualized by picosecond X-ray crystallography. *Nature Chemistry* **2013**, *5*, 212–220.

[107] Tenboer, J. et al. Time-resolved serial crystallography captures high-resolution intermediates of photoactive yellow protein. *Science* **2014**, *346*, 1242–1246.

[108] Pande, K. et al. Femtosecond structural dynamics drives the trans/cis isomerization in photoactive yellow protein. *Science* **2016**, *352*, 725–729.

[109] Schmidt, M. A short history of structure based research on the photocycle of photoactive yellow protein. *Structural Dynamics* **2017**, *4*, 032201.

[110] Devanathan, S.; Pacheco, A.; Ujj, L.; Cusanovich, M.; Tollin, G.; Lin, S.; Woodbury, N. Femtosecond spectroscopic observations of initial intermediates in the photocycle of the photoactive yellow protein from Ectothiorhodospira halophila. *Biophysical Journal* **1999**, *77*, 1017–1023.

[111] Larsen, D. S.; van Stokkum, I. H.; Vengris, M.; van der Horst, M. A.; de Weerd, F. L.; Hellingwerf, K. J.; van Grondelle, R. Incoherent Manipulation of the Photoactive Yellow Protein Photocycle with Dispersed Pump-Dump-Probe Spectroscopy. *Biophysical Journal* **2004**, *87*, 1858–1872.

[112] Changenet-Barret, P.; Espagne, A.; Plaza, P.; Martin, M.; Hellingwerf, K. *Femtochemistry and Femtobiology*; Elsevier, 2004; pp 417–420.

[113] Lincoln, C. N.; Fitzpatrick, A. E.; Thor, J. J. v. Photoisomerisation quantum yield and non-linear cross-sections with femtosecond excitation of the photoactive yellow protein. *Physical Chemistry Chemical Physics* **2012**, *14*, 15752.

[114] Zhu, J.; Paparelli, L.; Hospes, M.; Arents, J.; Kennis, J. T. M.; van Stokkum, I. H. M.; Hellingwerf, K. J.; Groot, M. L. Photoionization and Electron Radical Recombination Dynamics in Photoactive Yellow Protein Investigated by Ultrafast Spectroscopy in the Visible and Near-Infrared Spectral Region. *The Journal of Physical Chemistry B* **2013**, *117*, 11042–11048.

[115] Van Wilderen, L. J.; Van Der Horst, M. A.; Van Stokkum, I. H.; Hellingwerf, K. J.; Van Grondelle, R.; Groot, M. L. Ultrafast infrared spectroscopy reveals a key step for successful entry into the photocycle for photoactive yellow protein. *Proceedings of the National Academy of Sciences of the United States of America* **2006**, *103*, 15050–15055.

[116] Creelman, M.; Kumauchi, M.; Hoff, W. D.; Mathies, R. A. Chromophore

dynamics in the PYP photocycle from femtosecond stimulated raman spectroscopy. *Journal of Physical Chemistry B* **2014**, *118*, 659–667.

[117] Kuramochi, H.; Takeuchi, S.; Yonezawa, K.; Kamikubo, H.; Kataoka, M.; Tahara, T. Probing the early stages of photoreception in photoactive yellow protein with ultrafast time-domain Raman spectroscopy. *Nature Chemistry* **2017**, *9*, 660–666.

[118] Mooney, C. R. S.; Parkes, M. A.; Iskra, A.; Fielding, H. H. Controlling Radical Formation in the Photoactive Yellow Protein Chromophore. *Angewandte Chemie International Edition* **2015**, *54*, 5646–5649.

[119] Parkes, M. A.; Phillips, C.; Porter, M. J.; Fielding, H. H. Controlling electron emission from the photoactive yellow protein chromophore by substitution at the coumaric acid group. *Physical Chemistry Chemical Physics* **2016**, *18*, 10329–10336.

[120] Henley, A.; Diveky, M. E.; Patel, A. M.; Parkes, M. A.; Anderson, J. C.; Fielding, H. H. Electronic structure and dynamics of torsion-locked photoactive yellow protein chromophores. *Physical Chemistry Chemical Physics* **2017**, *19*, 31572–31580.

[121] Henley, A.; Patel, A. M.; Parkes, M. A.; Anderson, J. C.; Fielding, H. H. Role of Photoisomerization on the Photodetachment of the Photoactive Yellow Protein Chromophore. *The Journal of Physical Chemistry A* **2018**, *122*, 8222–8228.

[122] Lee, I.-R.; Lee, W.; Zewail, A. H. Primary steps of the photoactive yellow protein: Isolated chromophore dynamics and protein directed function. *Proceedings of the National Academy of Sciences* **2006**, *103*, 258–262.

[123] Bull, J. N.; Anstöter, C. S.; Verlet, J. R. R. Ultrafast valence to non-valence excited state dynamics in a common anionic chromophore. *Nature Communications* **2019**, *10*, 5820.

[124] Anstöter, C. S.; Curchod, B. F. E.; Verlet, J. R. R. Geometric and electronic structure probed along the isomerisation coordinate of a photoactive yellow protein chromophore. *Nature Communications* **2020**, *11*, 2827.

[125] Anstöter, C. S.; Curchod, B. F. E.; Verlet, J. R. R. Photo-isomerization of the isolated photoactive yellow protein chromophore: what comes before the primary step? *Physical Chemistry Chemical Physics* **2022**, *24*, 1305–1309.

[126] Ashworth, E. K.; Coughlan, N. J.; Hopkins, W. S.; Bieske, E. J.; Bull, J. N. Excited-State Barrier Controls E → Z Photoisomerization in p-Hydroxycinnamate Biochromophores. *Journal of Physical Chemistry Letters* **2022**, *13*, 9028–9034.

[127] Changenet-Barret, P.; Plaza, P.; Martin, M. M. Primary events in the photoactive yellow protein chromophore in solution. *Chemical Physics Letters* **2001**, *336*, 439–444.

[128] Changenet-Barret, P.; Espagne, A.; Katsonis, N.; Charier, S.; Baudin, J. B.; Jullien, L.; Plaza, P.; Martin, M. M. Excited-state relation dynamics of a PYP chromophore model in solution: Influence of the thioester group. *Chemical Physics Letters* **2002**, *365*, 285–291.

[129] Larsen, D. S.; Vengris, M.; van Stokkum, I. H.; van der Horst, M. A.; Cordfunke, R. A.; Hellingwerf, K. J.; van Grondelle, R. Initial photoinduced dynamics of the photoactive yellow protein chromophore in solution. *Chemical Physics Letters* **2003**, *369*, 563–569.

[130] Changenet-Barret, P.; Espagne, A.; Charier, S.; Baudin, J.-B.; Jullien, L.; Plaza, P.; Hellingwerf, K. J.; Martin, M. M. Early molecular events in the photoactive yellow protein: role of the chromophore photophysics. *Photochemical & Photobiological Sciences* **2004**, *3*, 823.

[131] Espagne, A.; Changenet-Barret, P.; Charier, S.; Baudin, J.-B.; Jullien, L.; Plaza, P.; Martin, M. *Femtochemistry and Femtobiology*; Elsevier, 2004; pp 421–424.

[132] Espagne, A.; Changenet-Barret, P.; Plaza, P.; Martin, M. M. Solvent effect on the excited-state dynamics of analogues of the photoactive Yellow Protein chromophore. *Journal of Physical Chemistry A* **2006**, *110*, 3393–3404.

[133] Espagne, A.; Changenet-Barret, P.; Baudin, J.-B.; Plaza, P.; Martin, M. M. Photoinduced charge shift as the driving force for the excited-state relaxation of analogues of the Photoactive Yellow Protein chromophore in solution. *Journal of Photochemistry and Photobiology A: Chemistry* **2007**, *185*, 245–252.

[134] Changenet-Barret, P.; Lacombat, F.; Plaza, P. Reaction-coordinate tracking in the excited-state deactivation of the photoactive yellow protein chromophore in solution. *Journal of Photochemistry and Photobiology A: Chemistry* **2012**, *234*, 171–180.

[135] Mustalahti, S.; Morozov, D.; Luk, H. L.; Pallerla, R. R.; Myllyperkiö, P.; Pettersson, M.; Pihko, P. M.; Groenhof, G. Photoactive Yellow Protein Chromophore Photoisomerizes around a Single Bond if the Double Bond Is Locked. *Journal of Physical Chemistry Letters* **2020**, *11*, 2177–2181.

[136] Espagne, A.; Paik, D. H.; Changenet-Barret, P.; Martin, M. M.; Zewail, A. H. Ultrafast Photoisomerization of Photoactive Yellow Protein Chromophore Analogues in Solution: Influence of the Protonation State. *ChemPhysChem* **2006**, *7*, 1717–1726.

[137] Espagne, A.; Paik, D. H.; Changenet-Barret, P.; Plaza, P.; Martin, M. M.; Zewail, A. H. Ultrafast light-induced response of photoactive yellow protein chromophore analogues. *Photochemical & Photobiological Sciences* **2007**, *6*, 780.

[138] Henley, A. Electronic structure and dynamics of photoactive yellow protein chromophores. Ph.D. thesis, University College London, 2020.

[139] Seidel, R.; Pohl, M. N.; Ali, H.; Winter, B.; Aziz, E. F. Advances in liquid phase soft-x-ray photoemission spectroscopy: A new experimental setup at BESSY II. *Review of Scientific Instruments* **2017**, *88*.

[140] Malerz, S.; Haak, H.; Trinter, F.; Stephansen, A. B.; Kolbeck, C.; Pohl, M.; Hergenhahn, U.; Meijer, G.; Winter, B. A setup for studies of photoelectron circular dichroism from chiral molecules in aqueous solution. *Review of Scientific Instruments* **2022**, *93*.

[141] Boichenko, A. N.; Bochenkova, A. V. Private communication. **2025**,

[142] Rocha-Rinza, T.; Christiansen, O.; Rajput, J.; Gopalan, A.; Rahbek, D. B.; Andersen, L. H.; Bochenkova, A. V.; Granovsky, A. A.; Bravaya, K. B.; Nemukhin, A. V.; Christiansen, K. L.; Nielsen, M. B. Gas Phase Absorption Studies of Photoactive Yellow Protein Chromophore Derivatives. *The Journal of Physical Chemistry A* **2009**, *113*, 9442–9449.

[143] Henley, A.; Riley, J. W.; Wang, B.; Fielding, H. H. An experimental and computational study of the effect of aqueous solution on the multiphoton ionisation photoelectron spectrum of phenol. *Faraday Discussions* **2020**, *221*, 202–218.

[144] Dupuy, R.; Buttersack, T.; Trinter, F.; Richter, C.; Gholami, S.; Björneholm, O.; Hergenhahn, U.; Winter, B.; Bluhm, H. The solvation shell probed by resonant intermolecular Coulombic decay. *Nature Communications* **2024**, *15*, 6926.

[145] Credidio, B.; Thürmer, S.; Stemer, D.; Pugini, M.; Trinter, F.; Vokrouhlický, J.; Slavíček, P.; Winter, B. From Gas to Solution: The Changing Neutral Structure of Proline upon Solvation. *The Journal of Physical Chemistry A* **2024**, *128*, 10202–10212.

[146] Lambropoulos, P. *Topics on Multiphoton Processes in Atoms*; 1976; pp 87–164.

[147] Henley, A.; Fielding, H. H. Anion photoelectron spectroscopy of protein chromophores. *International Reviews in Physical Chemistry* **2019**, *38*, 1–34.

[148] García-Prieto, F. F.; Aguilar, M. A.; Galván, I. F.; Muñoz-Losa, A.; Olivares del Valle, F. J.; Sánchez, M. L.; Martín, M. E. Substituent and Solvent Effects on the UV–vis Absorption Spectrum of the Photoactive Yellow Protein Chromophore. *The Journal of Physical Chemistry A* **2015**, *119*, 5504–5514.

[149] Sprenger, W. W.; Hoff, W. D.; Armitage, J. P.; Hellingwerf, K. J. The eubacterium Ectothiorhodospira halophila is negatively phototactic, with a wavelength dependence that fits the absorption spectrum of the photoactive yellow protein. *Journal of Bacteriology* **1993**, *175*, 3096–3104.

[150] McRee, D. E.; Tainer, J. A.; Meyer, T. E.; Van Beeumen, J.; Cusanovich, M. A.; Getzoff, E. D. Crystallographic structure of a photoreceptor protein at 2.4 A resolution. *Proceedings of the National Academy of Sciences of the United States of America* **1989**, *86*, 6533–6537.

[151] Schmidt, M. A short history of structure based research on the photocycle of photoactive yellow protein. *Structural Dynamics* **2017**, *4*, 032201.

[152] Xing, J.; Gumerov, V. M.; Zhulin, I. B. Photoactive Yellow Protein Represents a Distinct, Evolutionarily Novel Family of PAS Domains. *Journal of Bacteriology* **2022**, *204*.

[153] Kuramochi, H.; Takeuchi, S.; Kamikubo, H.; Kataoka, M.; Tahara, T. Skeletal Structure of the Chromophore of Photoactive Yellow Protein in the Excited State Investigated by Ultraviolet Femtosecond Stimulated Raman Spectroscopy. *Journal of Physical Chemistry B* **2021**, *125*, 6154–6161.

[154] Imamoto, Y.; Mihara, K.; Hisatomi, O.; Kataoka, M.; Tokunaga, F.; Bojkova, N.; Yoshihara, K. Evidence for proton transfer from Glu-46 to the chromophore during the photocycle of photoactive yellow protein. *Journal of Biological Chemistry* **1997**, *272*, 12905–12908.

[155] Pan, D.; Philip, A.; Hoff, W. D.; Mathies, R. A. Time-Resolved Resonance Raman Structural Studies of the pB Intermediate in the Photocycle of Photoactive Yellow Protein. *Biophysical Journal* **2004**, *86*, 2374–2382.

[156] Xie, A.; Kelemen, L.; Hendriks, J.; White, B. J.; Hellingwerf, K. J.; Hoff, W. D. Formation of a new buried charge drives a large-amplitude protein quake in photoreceptor activation. *Biochemistry* **2001**, *40*, 1510–1517.

[157] Cho, H. S.; Schotte, F.; Dashdorj, N.; Kyndt, J.; Henning, R.; Anfinrud, P. A. Picosecond Photobiology: Watching a Signaling Protein Function in Real Time via Time-Resolved Small- and Wide-Angle X-ray Scattering. *Journal of the American Chemical Society* **2016**, *138*, 8815–8823.

[158] Schotte, F.; Cho, H. S.; Dyda, F.; Anfinrud, P. Watching a signaling protein function: What has been learned over four decades of time-resolved studies of photoactive yellow protein. *Structural Dynamics* **2024**, *11*, 1–20.

[159] Mix, L. T.; Carroll, E. C.; Morozov, D.; Pan, J.; Gordon, W. R.; Philip, A.; Fuzell, J.; Kumauchi, M.; Van Stokkum, I.; Groenhof, G.; Hoff, W. D.; Larsen, D. S. Excitation-Wavelength-Dependent Photocycle Initiation Dynamics Resolve Heterogeneity in the Photoactive Yellow Protein from Halorhodospira halophila. *Biochemistry* **2018**, *57*, 1733–1747.

[160] Chosrowjan, H.; Taniguchi, S.; Tanaka, F. Ultrafast fluorescence upconversion technique and its applications to proteins. *FEBS Journal* **2015**, *282*, 3003–3015.

[161] Schotte, F.; Cho, H. S.; Kaila, V. R.; Kamikubo, H.; Dashdorj, N.; Henry, E. R.; Graber, T. J.; Henning, R.; Wulff, M.; Hummer, G.; Kataoka, M.; Anfinrud, P. A. Watching a signaling protein function in real time via 100-ps time-resolved Laue crystallography. *Proceedings of the National Academy of Sciences of the United States of America* **2012**, *109*, 19256–19261.

[162] Cho, H. S.; Schotte, F.; Dashdorj, N.; Kyndt, J.; Anfinrud, P. A. Probing anisotropic structure changes in proteins with picosecond time-resolved small-angle X-ray scattering. *Journal of Physical Chemistry B* **2013**, *117*, 15825–15832.

[163] Gromov, E. V.; Burghardt, I.; Köppel, H.; Cederbaum, L. S. Photoinduced isomerization of the photoactive yellow protein (PYP) chromophore: Interplay of two torsions, a HOOP mode and hydrogen bonding. *Journal of Physical Chemistry A* **2011**, *115*, 9237–9248.

[164] García-Prieto, F. F.; Muñoz-Losa, A.; Fdez. Galván, I.; Sánchez, M. L.; Aguilar, M. A.; Martín, M. E. QM/MM Study of Substituent and Solvent Effects on the Excited State Dynamics of the Photoactive Yellow Protein Chromophore. *Journal of Chemical Theory and Computation* **2017**, *13*, 737–748.

[165] Boggio-Pasqua, M.; Burmeister, C. F.; Robb, M. A.; Groenhof, G. Photochemical reactions in biological systems: Probing the effect of the environment by means of hybrid quantum chemistry/molecular mechanics simulations. *Physical Chemistry Chemical Physics* **2012**, *14*, 7912–7928.

[166] García-Prieto, F. F.; Muñoz-Losa, A.; Luz Sánchez, M.; Elena Martín, M.; Aguilar, M. A. Solvent effects on de-excitation

channels in the p-coumaric acid methyl ester anion, an analogue of the photoactive yellow protein (PYP) chromophore. *Physical Chemistry Chemical Physics* **2016**, *18*, 27476–27485.

[167] Groenhof, G.; Bouxin-Cademartory, M.; Hess, B.; de Visser, S. P.; Berendsen, H. J. C.; Olivucci, M.; Mark, A. E.; Robb, M. A. Photoactivation of the Photoactive Yellow Protein: Why Photon Absorption Triggers a Trans-to-Cis Isomerization of the Chromophore in the Protein. *Journal of the American Chemical Society* **2004**, *126*, 4228–4233.

[168] Vengris, M.; Larsen, D. S.; Van Der Horst, M. A.; Larsen, O. F.; Hellingwerf, K. J.; Van Grondelle, R. Ultrafast dynamics of isolated model photoactive yellow protein chromophores: "Chemical perturbation theory" in the laboratory. *Journal of Physical Chemistry B* **2005**, *109*, 4197–4208.

[169] Boggio-Pasqua, M.; Robb, M. A.; Groenhof, G. Hydrogen Bonding Controls Excited-State Decay of the Photoactive Yellow Protein Chromophore. *Journal of the American Chemical Society* **2009**, *131*, 13580–13581.

[170] Larsen, D. S.; Vengris, M.; van Stokkum, I. H.; van der Horst, M. A.; de Weerd, F. L.; Hellingwerf, K. J.; van Grondelle, R. Photoisomerization and Photoionization of the Photoactive Yellow Protein Chromophore in Solution. *Biophysical Journal* **2004**, *86*, 2538–2550.

[171] Changenet-Barret, P.; Loukou, C.; Ley, C.; Lacombat, F.; Plaza, P.; Mallet, J.-M.; Martin, M. M. Primary photodynamics of a biomimetic model of photoactive yellow protein (PYP). *Physical Chemistry Chemical Physics* **2010**, *12*, 13715.

[172] Boggio-Pasqua, M.; Groenhof, G. Controlling the Photoreactivity of the Photoactive Yellow Protein Chromophore by Substituting at the p -

Coumaric Acid Group. *The Journal of Physical Chemistry B* **2011**, *115*, 7021–7028.

[173] Jimenez, R.; Fleming, G. R.; Kumar, P. V.; Maroncelli, M. Femtosecond solvation dynamics of water. *Nature* **1994**, *369*, 471–473.

[174] Kusaka, R.; Nihonyanagi, S.; Tahara, T. The photochemical reaction of phenol becomes ultrafast at the air–water interface. *Nature Chemistry* **2021**, *13*, 306–311.

[175] Ishiyama, T.; Tahara, T.; Morita, A. Why the Photochemical Reaction of Phenol Becomes Ultrafast at the Air–Water Interface: The Effect of Surface Hydration. *Journal of the American Chemical Society* **2022**, *144*, 6321–6325.

[176] Jordan, C. J.; Lowe, E. A.; Verlet, J. R. Photooxidation of the Phenolate Anion is Accelerated at the Water/Air Interface. *Journal of the American Chemical Society* **2022**, *144*, 14012–14015.

[177] Jordan, C. J.; Coons, M. P.; Herbert, J. M.; Verlet, J. R. Spectroscopy and dynamics of the hydrated electron at the water/air interface. *Nature Communications* **2024**, *15*, 1–8.

[178] Ruckebusch, C.; Sliwa, M.; Pernot, P.; de Juan, A.; Tauler, R. Comprehensive data analysis of femtosecond transient absorption spectra: A review. *Journal of Photochemistry and Photobiology C: Photochemistry Reviews* **2012**, *13*, 1–27.

[179] Gromov, E. V.; Burghardt, I.; Hynes, J. T.; Köppel, H.; Cederbaum, L. S. Electronic structure of the photoactive yellow protein chromophore: Ab initio study of the low-lying excited singlet states. *Journal of Photochemistry and Photobiology A: Chemistry* **2007**, *190*, 241–257.

[180] Elkins, M. H.; Williams, H. L.; Neumark, D. M. Isotope effect on hy-

drated electron relaxation dynamics studied with time-resolved liquid jet photoelectron spectroscopy. *Journal of Chemical Physics* **2016**, *144*.

[181] Schwartz, B. J.; Rossky, P. J. The isotope effect in solvation dynamics and nonadiabatic relaxation: A quantum simulation study of the photoexcited solvated electron in D2O. *Journal of Chemical Physics* **1996**, *105*, 6997–7010.

[182] Svishchev, I. M.; Kusalik, P. G. Dynamics in liquid water, water-d2, and water-t2: a comparative simulation study. *The Journal of Physical Chemistry* **1994**, *98*, 728–733.

[183] Reutt, J. E.; Wang, L. S.; Lee, Y. T.; Shirley, D. A. Molecular beam photoelectron spectroscopy and femtosecond intramolecular dynamics of H2O+ and D2O+. *The Journal of Chemical Physics* **1986**, *85*, 6928–6939.

[184] Szmytkowski, C.; Maciag, K.; Koenig, P.; Zecca, A.; Oss, S.; Grisenti, R. D2O absolute total electron-scattering cross sections. *Chemical Physics Letters* **1991**, *179*, 114–118.

[185] Itikawa, Y.; Mason, N. Cross Sections for Electron Collisions with Water Molecules. *Journal of Physical and Chemical Reference Data* **2005**, *34*, 1–22.

[186] Ben Arfa, M.; Edard, F.; Tronc, M. Isotope effect in resonant vibrational excitation of H2O (D2O), NH3 (ND3), CH4 (CD4). *Chemical Physics Letters* **1990**, *167*, 602–606.

[187] Allan, M.; Moreira, O. Excitation of the symmetric and antisymmetric stretch vibrations of H 2 O by electron impact. *Journal of Physics B: Atomic, Molecular and Optical Physics* **2002**, *35*, L37–L42.

[188] Hardy, E. H.; Zygar, A.; Zeidler, M. D.; Holz, M.; Sacher, F. D. Isotope

effect on the translational and rotational motion in liquid water and ammonia. *Journal of Chemical Physics* **2001**, *114*, 3174–3181.